



TECHNISCHE
UNIVERSITÄT
WIEN

DIPLOMARBEIT

**2 + 1D gauge theories
in a Bjorken-expanding space-time**

zur Erlangung des akademischen Grades

Diplom-Ingenieur

im Rahmen des Studiums

Technische Physik

eingereicht von

Paul Hotzy BSc BSc

Matrikelnummer 01426503

ausgeführt am Institut für Theoretische Physik
der Fakultät für Physik der Technischen Universität Wien

Betreuer:

Privatdoz. Dipl.-Ing. Dr.techn. Andreas Ipp

Verantwortlicher Mitbetreuer:

Univ.Ass. Dr.rer.nat. Kirill Boguslavski

Wien, 21. Oktober 2021

Paul Hotzy
(Verfasser)

Dr. Andreas Ipp
(Betreuer)

Dr. Kirill Boguslavski
(Verantwortlicher Mitbetreuer)



Die approbierte gedruckte Originalversion dieser Diplomarbeit ist an der TU Wien Bibliothek verfügbar
The approved original version of this thesis is available in print at TU Wien Bibliothek.


Eidesstattliche Erklärung

Ich erkläre an Eides statt, dass die vorliegende Arbeit nach den anerkannten Grundsätzen für wissenschaftliche Abhandlungen von mir selbstständig erstellt wurde. Alle verwendeten Hilfsmittel, insbesondere die zugrunde gelegte Literatur, sind in dieser Arbeit genannt und aufgelistet. Die aus den Quellen wörtlich entnommenen Stellen, sind als solche kenntlich gemacht.

Das Thema dieser Arbeit wurde von mir bisher weder im In- noch Ausland einer Beurteilerin/einem Beurteiler zur Begutachtung in irgendeiner Form als Prüfungsarbeit vorgelegt. Diese Arbeit stimmt mit der von den Begutachterinnen/Begutachtern beurteilten Arbeit überein.



Unterschrift



Ort, Datum



Die approbierte gedruckte Originalversion dieser Diplomarbeit ist an der TU Wien Bibliothek verfügbar
The approved original version of this thesis is available in print at TU Wien Bibliothek.

Abstract

We conduct classical statistical simulations for $SU(2)$ gauge theories in a 2+1 dimensional Bjorken expanding space-time with a particular interest in the dynamical behaviour at large time scales. Motivated by the early stages of ultra-relativistic heavy-ion collisions, we compare boost invariant Glasma initial conditions with Gaussian initial conditions using the same Bjorken expanding metric, and study general late-time features of the gluonic plasmas. Particular emphasis is put on the dynamics of the energy stress-tensor and its components, on the dynamics of correlation functions of gauge and chromo-electric fields in momentum space, and on the computation of distribution functions. We find that systems with these different sets of initial conditions show different properties at late times of their dynamical evolution, which is imposed by the late-time properties of the scalar sector for 2+1 dimensional gauge systems undergoing Bjorken expansion. We observe that in contrast to the Gaussian initial conditions the Glasma reaches a state of linear scalar particle production. We collect evidence that the differences in the dynamics for both systems stem from higher-order contributions of connected n -point correlation functions. This linear growth of the average scalar particle numbers is responsible for a linear increase of the energy density contribution from the longitudinal chromo-electric field when compared to other contributions to the energy density. We further observe a rapid freezing of the gluonic distribution function, and a nontrivial evolution of the scalar distribution function even at late times which substantiate the argument for the scalar sector being responsible for the changes in the late-time dynamics. Our results further suggest that the Glasma does not approach a clear quasi-particle picture which implies that the transition to a kinetic theory has to be treated with caution.



Die approbierte gedruckte Originalversion dieser Diplomarbeit ist an der TU Wien Bibliothek verfügbar
The approved original version of this thesis is available in print at TU Wien Bibliothek.

Zusammenfassung

Wir führen klassisch statistische Simulationen für $SU(2)$ Eichtheorien in einer $2+1$ dimensionalen Bjorken expandierenden Raumzeit mit besonderem Interesse am dynamischen Verhalten auf großen Zeitskalen durch. Motiviert durch die frühen Stadien ultrarelativistischer Schwerionenkollisionen vergleichen wir die Boost-invarianten Glasma-Anfangsbedingungen mit Gauß'schen Anfangsbedingungen unter Verwendung derselben expandierenden Bjorken-Metrik und untersuchen allgemeine spätzeitliche Merkmale der gluonischen Plasmen. Besonderes Augenmerk wird auf die Dynamik des Energie-Impuls-Tensors und seiner Komponenten, auf die Dynamik von Korrelationsfunktionen von Eich- und chromo-elektrischen Feldern im Impulsraum sowie auf die Berechnung von Verteilungsfunktionen gelegt. Wir stellen fest, dass Systeme mit diesen unterschiedlichen Anfangsbedingungen zu späten Zeiten ihrer dynamischen Entwicklung unterschiedliche Eigenschaften aufweisen, was durch die spätzeitlichen Eigenschaften des skalaren Sektors für $2+1$ -dimensionale Eichsysteme, die eine Björken-Expansion durchlaufen, erklärt werden kann. Wir beobachteten, dass das Glasma im Gegensatz zu den Gauß'schen Anfangsbedingungen einen Zustand der linearen skalaren Teilchenproduktion erreicht. Wir sammeln Indizien dafür, dass die Unterschiede in der Dynamik beider Systeme von Beiträgen höherer Ordnung von zusammenhängender n -Punkt-Korrelationsfunktionen herrühren. Dieses lineare Wachstum der durchschnittlichen skalaren Teilchenzahlen ist für einen linearen Anstieg des Energiedichtebeitrags aus dem longitudinalen chromo-elektrischen Feld im Vergleich zu anderen Beiträgen zur Energiedichte verantwortlich. Wir beobachten weiterhin ein schnelles Einfrieren der gluonischen Verteilungsfunktion und eine nichttriviale Entwicklung der skalaren Verteilungsfunktion selbst zu späten Zeiten, was das Argument dafür erhärtet, dass der skalare Sektor für die Änderungen in der spätzeitlichen Dynamik verantwortlich ist. Unsere Ergebnisse legen außerdem nahe, dass sich das Glasma keinem klaren Quasiteilchen Bild nähert, was bedeutet, dass der Übergang zu einer kinetischen Theorie kritisch zu hinterfragen ist.



Die approbierte gedruckte Originalversion dieser Diplomarbeit ist an der TU Wien Bibliothek verfügbar
The approved original version of this thesis is available in print at TU Wien Bibliothek.

Acknowledgments

First and foremost, I would like to thank my responsible supervisor Dr. Kirill Boguslavski for his guidance and the time he devoted to this thesis. I consider myself very fortunate to continue our collaboration during my PhD studies. I also want to thank Dr. Andreas Ipp for the supervision of this project. Furthermore, I want to express my gratitude to my parents who made it possible for me to study physics and mathematics. Finally, I have to thank Patricia for her invaluable support over the majority of my academic career in so many ways.



Die approbierte gedruckte Originalversion dieser Diplomarbeit ist an der TU Wien Bibliothek verfügbar
The approved original version of this thesis is available in print at TU Wien Bibliothek.

Contents

1	Introduction	1
1.1	Motivation	1
1.2	Outline	3
2	Theoretical Background	4
2.1	Bjorken expanding space-times	4
2.2	Introduction to QCD in the continuum	5
2.3	Introduction to Lattice QCD	7
2.4	Classical-statistical simulations	11
2.5	Observables	18
3	Initial Conditions	23
3.1	Glasma Initial Conditions	23
3.2	Gaussian Initial Conditions	30
3.3	Equations of motion	33
4	Energy densities for expanding space-times	37
4.1	Energy densities for Glasma initial conditions	37
4.2	Energy densities of gauge systems with Gaussian initial conditions	42
5	Results for large time scales	47
5.1	Energy densities at large time scales of the Glasma	47
5.2	Distribution function and correlations at late-times of the Glasma	49
5.3	Hard momentum scales and characteristic occupancy of the Glasma	55
5.4	Lattice spacing (in-)dependence of Glasma initial conditions	57
5.5	Gaussian initial conditions for large time scales	62
6	Conclusion	66
	Appendices	69
A	Properties of $SU(N_c)$ and $\mathfrak{su}(N_c)$	69
B	Algorithm for $SU(2)$ theories	72
C	Conversion to lattice units	73
	Bibliography	77



Die approbierte gedruckte Originalversion dieser Diplomarbeit ist an der TU Wien Bibliothek verfügbar
The approved original version of this thesis is available in print at TU Wien Bibliothek.

Chapter 1

Introduction

In this thesis we are interested in the dynamical behavior of 2+1 dimensional gauge systems in a Bjorken-expanding space-time. For our analysis we conduct classical statistical simulations of two different types of initial conditions for non-thermal gauge systems and employ a quasi-particle picture for some observables to compare the systems and interpret our results. In this chapter we want to give a motivation for this investigation and give a brief outline of this work.

1.1 Motivation

Strongly interacting matter is described by quantum chromo-dynamics (QCD), which is a non-Abelian gauge theory with the symmetry group $SU(3)$. In this theory the gauge boson is introduced as an exchange particle between quarks, which are the fundamental building blocks of atomic nuclei. In particular, the non-Abelian symmetry group introduces various interesting physical and mathematical features. Two of them are known as *asymptotic freedom* and *self-interacting gluons*.

Self-interacting gluons render pure gauge systems physically meaningful as they describe interacting systems consisting only of gluons. This is particularly interesting for states where the dynamical behavior is governed by gluons and therefore allows us to drop the quark contributions. These theories are known as Yang-Mills theories. Pure gauge theories therefore also help to understand the full theory of interacting quarks and gluons better.

Asymptotic freedom is known as the behavior of the running coupling constant of QCD, which gets large at small momentum regimes. This behavior appears counter intuitive since despite many similarities to quantum electrodynamics (QED), which is the gauge theory with the symmetry group $U(1)$, we cannot observe asymptotic freedom for QED. More importantly, because of the increasing coupling constant at low momenta perturbative approaches fail at these regimes. A possible solution to circumvent this problem is to use a non-perturbative description of QCD by discretizing the fields on a lattice [1, 2]. We refer to this formulation of the theory as *Lattice QCD* throughout this thesis.

In this work we are interested in the dynamical behavior of gluonic systems created in heavy-ion collisions. In such collisions a state of quarks and gluons is created which is known as quark gluon plasma (QGP). These collisions could be produced in experiments at the Large Hadron Collider (LHC) and the Relativistic Heavy Ion Collider (RHIC) and therefore present a viable test to the QCD description of the phenomena observed in these experiments. Further, heavy-ion collisions can be used to model the very early stages of our universe and therefore have implications relevant to cosmology. Astonishingly the QGP behaves similar to ideal fluids for sufficiently late times and can therefore be described by hydrodynamics [3, 4, 5].

At the earliest stages, immediately after the ultra-relativistic heavy-ion collision, the created gluonic system is in a non-thermal state which means that the gluons do not follow the Bose-Einstein statistic. Since the high collision energy leads to a near boost invariance in the collision

direction this stage is described in a longitudinally expanding coordinate system which is imposed by the Bjorken metric. In this space-time the description of this symmetry renders in an independence of the so-called rapidity direction. The hydrodynamic approach only describes the evolution of the QGP close-to-equilibrium and therefore does not provide a viable description for the earliest times after the heavy-ion collision. The state directly after an ultra-relativistic heavy-ion collision is often modeled as the Glasma [6, 7, 8]. After a short transient time a kinetic description is used that smoothly transitions into a hydrodynamic description. [9, 10, 11]. The Glasma can therefore be seen as a pre-hydrodynamic and pre-kinetic phase of the QGP.

The Glasma is derived with the framework of the color glass condensate (CGC), which describes a classical effective theory of QCD at high energy regimes [12, 13, 14]. In this model the valence quarks carry most of the momentum and are described by Lorentz-contracted sheets of color charges. These high momentum charges create a highly occupied color field which is predominantly governed by low momentum gluons. In the CGC a momentum cutoff is introduced to separate both constituents, i.e., the hard scales (high momentum valence quarks) and soft scales (low momentum gluons). The CGC yields an effective description for high energy nuclei of which the dynamics for the color fields and color charges is governed by Yang-Mills theories. A combination of the CGC with kinetic theory and a hydro-dynamical description of the QGP provides a modern approach for the analysis of heavy-ion collisions known as IP-Glasma and extensions thereof [15, 16, 17, 18, 19, 20, 21, 10].

In the ultra-relativistic limit the color sheet which describes the color charge density of the nuclei gets infinitesimally thin because of the Lorentz contraction. We therefore obtain an effective 2+1 dimensional system with boost invariant fields in the rapidity direction. The dependence of the rapidity of this system can be analyzed in 3+1 dimensional Glasma simulations [8, 22, 23, 24, 25]. Alternatively, the rapidity dependence can be analyzed by conducting simulations for different rapidity values [26, 27]. In this work we use the McLerran-Venugopalan model (MV-model) to describe the Glasma in 2+1 dimensions as it is built on simple physical assumptions and enables a straightforward implementation of the initial conditions [8, 28, 29].

In recent years many interesting features of the dynamical behaviour of non-thermal gauge theories have been found, such as universal and self-similar attractors for the evolution of the distribution function and non-thermal fixed points [30, 31, 32, 33, 34]. For these observations a quasi-particle picture was employed which is imposed by the definition of a single-particle distribution function. Kinetic theories are based on a quasi-particle description. We use Gaussian initial conditions as they use a quasi-particle picture in the initialization of the fields and therefore simplify the interpretation of the dynamics in terms of quasi-particles.

In this thesis we are interested in the dynamical behavior of non-thermal gauge systems described by Gaussian and Glasma initial conditions at large times scales. Moreover, distribution functions are important observables since they are also based on a quasi-particle picture. This is also the reason why we compare simulations with Glasma and Gaussian initial conditions: We want to understand the commonalities and differences between simulations that are dominated by classical fields and by large occupation numbers. We analyze an effectively 2+1 dimensional gauge system where the fields have three spatial components. We interpret the additional third component as a scalar field in adjoint representation and differentiate between the distribution for scalars and gluons. We will study their evolution by conducting classical-statistical simulations of the described gauge systems that are applicable due to the high occupation numbers and large fields of the considered systems [31, 33, 35, 34]. Additionally, a crucial difference of the two types of initial conditions is the consideration of the higher-order n -point correlation functions. The Gaussian initial conditions neglect all higher-order contributions by initializing the fields by solely considering the 2-point correlation function. On the other hand the Glasma initial conditions given by the MV-model describe the color-field and the chromo-electric field directly and therefore take all connected n -point correlation functions into account. This enables assessing the importance of higher-order contributions for simulated systems. In order to make both types of initial conditions comparable

we approximate the gluon distribution function at some observation time τ_0 and initialize the fields for the Gaussian initial condition according to this distribution by using the mode vector expansion of the fields [34, 33, 32].

1.2 Outline

In Chapter 2 we introduce the theoretic framework to describe the Glasma and Gaussian initial conditions. In particular, we give a brief introduction to the Bjorken space-time in Section 2.1 and discuss the most essential features of QCD and Lattice QCD in Sections 2.2 and 2.3. We further introduce the classical approximation and its range of validity for the gauge theories we investigate in Section 2.4. In the conducted simulations we are especially interested in the energy density and the 2-point correlation and distribution functions. These observables are introduced in Section 2.5.

We introduce the Glasma and Gaussian initial conditions and derive a lattice formulation for a Bjorken space-time in Sections 3.1 and 3.2. For our simulations we implement a leap-frog algorithm of which the update rules follow the discretized equations of motion which are described in Section 3.3.

Our simulations are implemented as a numerical framework written in the programming language C++. We present our results for small simulation times in Chapter 4. Parts of these results were obtained in the course of a bench-marking procedure to ensure a valid implementation that delivers results comparable to the literature. Furthermore, we discuss the parameters of the MV-model which describe the Glasma in Section 4.1.

In Chapter 5 we present and discuss our results for the long-time behavior of the dynamics for Gaussian and Glasma initial conditions. We compare both systems and find evidence for possible explanations for the different types of initial conditions.

Finally, we conclude our discussion in Chapter 6 where we also briefly recapitulate our results and give a short outlook for possible future work and open questions.

Chapter 2

Theoretical Background

In the following chapter we introduce the most important definitions and notions for the remainder of this thesis. In Section 2.1 we derive the coordinate system which is used for the conducted simulations. These coordinates are defined by the expanding Bjorken metric and are especially relevant for ultra-relativistic heavy-ion collision because they yield a near boost invariant gauge system in rapidity direction. Thereafter in Section 2.2 we give a brief overview of the most important aspects of quantum chromodynamics (QCD) and then introduce a discretized version of the continuum theory which is most often referred to as Lattice QCD in Section 2.3. This allows us to run classical statistical simulations on a lattice and further conduct a detailed analysis of the dynamical behavior of gauge systems. In this work we focus on pure gauge theories without any quark contributions. Nevertheless in the following subsections we will discuss the full QCD including fermions in order to get a clearer picture of the theory itself but also motivate certain steps and definitions in the realm of this theory.

2.1 Bjorken expanding space-times

We compare results for 2+1 dimensional gauge systems for $SU(2)$ gauge theories from a Minkowski metric with in a longitudinally expanding space-time, which is imposed by the Bjorken metric. The Minkowski metric is given by

$$g_{\mu\nu} = \text{diag}(1, -1, -1, -1). \quad (2.1.1)$$

We can perform a coordinate transformation defined by

$$\tau = \sqrt{t^2 + z^2}, \quad \eta = \tanh^{-1}\left(\frac{z}{t}\right) \quad (2.1.2)$$

to obtain the Bjorken metric

$$g_{\mu\nu} = \text{diag}(1, -1, -1, -\tau^2), \quad (2.1.3)$$

and its inverse

$$g^{\mu\nu} = \text{diag}\left(1, -1, -1, -\frac{1}{\tau^2}\right). \quad (2.1.4)$$

Here we call τ proper time and η (spatial) rapidity. Since throughout this text we will discuss results for both metric, we choose a formulation where the metric explicitly occurs and is time dependent. Further we use a covariant formulation where we write

$$\text{Minkowski: } x^\mu = \begin{pmatrix} x^0 \\ x^1 \\ x^2 \\ x^3 \end{pmatrix} = \begin{pmatrix} t \\ x \\ y \\ z \end{pmatrix}^\mu, \quad \text{Bjorken: } x^\mu = \begin{pmatrix} x^0 \\ x^1 \\ x^2 \\ x^3 \end{pmatrix} = \begin{pmatrix} \tau \\ x \\ y \\ \eta \end{pmatrix}^\mu \quad (2.1.5)$$

for our coordinate systems and imply Einsteins summation convention whenever two indices occur twice unless stated differently. Note that throughout this text we use natural units, hence $c = 1$ and $\hbar = 1$. With this notation we write $g(x^0)$ for the (proper) time dependent determinant, where we have

$$g_{\text{Minkowski}}(x^0) = -1, \quad g_{\text{Bjorken}}(x^0) = -\tau^2. \quad (2.1.6)$$

We will always write the dependence of x^0 explicitly in order to distinguish the determinant from the coupling constant g which is introduced in the next section. Further we want to emphasize that the discussion above seems inadequate for 2+1 dimensional systems since all the metrics are given in 3+1 dimensions. This viewpoint is resolved by interpreting the space-times, in which we conduct our analysis, to be completely homogeneous in the longitudinal direction and therefore should not be seen as an independent spatial dimension. Also, the space-time geometry is the same in the expanding case as in the flat Minkowski space-time since we merely performed a coordinate transformation. We introduced a singularity at $\tau = 0$, which is harmless because it stems from the coordinate transformation itself but needs to be taken into account when simulating systems in these coordinates. These two facts make it even more interesting that we will see different dynamical behaviors for the non-expanding and expanding case.

The reason why we impose the expanding metric is that ultra-relativistic heavy-ion collisions are almost boost invariant which renders in an independence in the rapidity direction. This originates from the fact that the colliding nuclei are Lorentz contracted onto a transverse plane. Therefore the introduction of a proper time and rapidity coordinate system will prove very useful. In addition large nuclei can be approximated as being homogeneous in transverse directions. This means that central heavy-ion collisions can be described by homogeneous systems in all spatial directions using the Bjorken metric.

2.2 Introduction to QCD in the continuum

We introduce the QCD action, which can be separated in the fermion and the gluon (gauge) part

$$S[\psi, \bar{\psi}, A] = S_G[A] + S_F[\psi, \bar{\psi}, A]. \quad (2.2.1)$$

The fermionic part will be mainly used to motivate certain steps taken and is not discussed in detail as in the rest of the text we are focusing on the gauge sector.

The fermionic part of the action is given by

$$S_F[\psi, \bar{\psi}, A] = \sum_{f=1}^{N_f} \int d^4x \sqrt{-g(x^0)} \quad (2.2.2)$$

$$\bar{\psi}^{(f)}(x)_{\alpha,c} \left[(\gamma^\mu)_{\alpha,\beta} (\delta_{c,d} \partial_\mu + ig A_\mu(x)_{c,d}) + m^{(f)} \delta_{\alpha\beta} \delta_{cd} \right] \psi^{(f)}(x)_{\beta,d},$$

where $\psi^{(f)}$ denote the fermion fields with mass $m^{(f)}$ which are represented by Dirac spinors with four components. In the expression above $\alpha, \beta = 1, 2, 3, 4$ and $c, d = 1, \dots, N_c$ enumerate the Dirac indices and the color indices of the fermion fields respectively. In addition, the contribution of the action of different fermion flavors $f = 1, \dots, N_f$ is summed over. $A_\mu(x)_{c,d}$ denote hermitian and traceless gauge fields, also called gluon or color fields in the context of QCD. These gauge fields are introduced to the fermionic part of the action in order to satisfy gauge invariance. For convenience we drop almost all indices above and only explicitly write them if they are of relevance. Lastly, the matrices γ are mixing different components of the Dirac spinors. A construction of these matrices can be found in almost any text book about particle physics or quantum field theories, e.g. [36]. In QCD we require the action to be invariant under local rotations of the color indices of the

fermions. Hence, the action (2.2.2) is invariant when the fields are rotated by a unitary matrix $\Omega(x)$ with $\det(\Omega(x)) = 1$, in each point x . It is well-known that these matrices form the special linear group often denoted as $SU(N_c)$. To be more precise this group is the defining representation of the Lie algebra $\mathfrak{su}(N_c)$. A more detailed discussion can be found in Appendix A. We will abbreviate the transformation of the fields by

$$\psi(x) \rightarrow \psi'(x) = \Omega(x)\psi(x), \quad A_\mu(x) \rightarrow A'_\mu(x), \quad (2.2.3)$$

and further the transformed action is given by

$$S_F[\psi', \bar{\psi}', A] = - \int d^4x \sqrt{-g(x^0)} \bar{\psi}'(x) \Omega(x)^\dagger [\gamma^\mu (\partial_\mu + igA'_\mu(x)) + m] \Omega(x) \psi(x). \quad (2.2.4)$$

Gauge invariance for the fermionic part of the action translates into

$$S_F[\psi, \bar{\psi}, A] = S_F[\psi', \bar{\psi}', A'], \quad (2.2.5)$$

which yields the transformation rule for the gauge fields

$$A_\mu(x) \rightarrow A'_\mu(x) = \Omega(x)A_\mu(x)\Omega(x)^\dagger + \frac{i}{g}(\partial_\mu\Omega(x))\Omega(x)^\dagger. \quad (2.2.6)$$

It can be shown that $A'_\mu(x)$ is hermitian and traceless as required, for a more detailed discussion see [36].

We now transition to the gluonic part of the QCD action for which we first define the covariant derivative and its corresponding transformation behavior

$$D_\mu(x) = \partial_\mu + igA_\mu(x), \quad (2.2.7)$$

$$D_\mu(x) \rightarrow D'_\mu(x) = \partial_\mu + igA'_\mu(x) = \Omega(x)D_\mu(x)\Omega(x)^\dagger. \quad (2.2.8)$$

This yields the expected transformation behavior for $D_\mu(x)\psi(x)$

$$D_\mu(x)\psi(x) \rightarrow \Omega(x)D_\mu(x)\Omega(x)^\dagger\Omega(x)\psi(x) = \Omega(x)D_\mu(x)\psi(x). \quad (2.2.9)$$

We have seen above that the color fields are no proper observables because they are not gauge invariant. Therefore in analogy to electrodynamics we define the field strength tensor as the commutator of the covariant derivative

$$F_{\mu\nu}(x) = -\frac{i}{g}[D_\mu(x), D_\nu(x)] = \partial_\mu A_\nu(x) - \partial_\nu A_\mu(x) + ig[A_\mu(x), A_\nu(x)], \quad (2.2.10)$$

and its transformation behavior is given by

$$F_{\mu\nu}(x) \rightarrow F'_{\mu\nu}(x) = \Omega(x)F_{\mu\nu}(x)\Omega(x)^\dagger. \quad (2.2.11)$$

The gauge part of QCD is now defined by

$$S_G[A] = -\frac{1}{2} \int d^4x \sqrt{-g(x^0)} \text{tr}(F^{\mu\nu}(x)F_{\mu\nu}(x)), \quad (2.2.12)$$

which is gauge invariant, because the trace is invariant under cyclic permutation of the matrices in the argument

$$\begin{aligned} \text{tr}(F^{\mu\nu}(x)F_{\mu\nu}(x)) &\rightarrow \text{tr}(F^{\mu\nu'}(x)F'_{\mu\nu'}(x)) = \text{tr}(\Omega(x)F^{\mu\nu}(x)\Omega(x)^\dagger\Omega(x)F_{\mu\nu}(x)\Omega(x)^\dagger) \\ &= \text{tr}(\Omega(x)^\dagger\Omega(x)F^{\mu\nu}(x)\Omega(x)^\dagger\Omega(x)F_{\mu\nu}(x)) \\ &= \text{tr}(F^{\mu\nu}(x)F_{\mu\nu}(x)). \end{aligned} \quad (2.2.13)$$

We now can define the chromo-electric and chromo-magnetic fields in terms of the field strength tensor

$$E_a^j(x) = -\sqrt{-g(x^0)}F_a^{0j}(x), \quad B_a^j(x) = -\frac{1}{2}\sqrt{-g(x^0)}\epsilon^{jkl}F_{kl}^a(x). \quad (2.2.14)$$

with the totally anti-symmetric Levi-Civita symbol ϵ^{jkl} .

Since the gauge fields $A_\mu(x)$ are (in fundamental representation) hermitian and traceless matrices they are elements of $\mathfrak{su}(N_c)$. We can decompose them with the hermitian traceless generators t^a of the Lie group $SU(N_c)$

$$A_\mu = A_\mu^a(x)t^a, \quad (2.2.15)$$

where $A_\mu^a(x)$ is the corresponding adjoint representation with its color components. These generators t^a satisfy the following properties

$$[t^a, t^b] = if^{abc}t^c, \quad \text{tr}(t^a t^b) = \frac{1}{2}\delta^{ab} \quad (2.2.16)$$

where f^{abc} can be interpreted as a totally anti-symmetric tensor and its entries are called structure constants of the given Lie algebra. The gluon action and the field strength tensor in terms of the generators can be restated as

$$F_{\mu\nu}^a = \partial_\mu A_\nu^a - \partial_\nu A_\mu^a + gf^{abc}A_\mu^b A_\nu^c, \quad (2.2.17)$$

$$S_G[A] = -\frac{1}{4} \int d^4x \sqrt{-g(x^0)} F_a^{\mu\nu}(x) F_{\mu\nu}^a(x).$$

using the properties in (2.2.16).

This representation for the gauge fields will also be used when discussing initial conditions for the observed systems. More specific information about the $SU(N_c)$ and $\mathfrak{su}(N_c)$ and the generators t^a can be found in Appendix A.

2.3 Introduction to Lattice QCD

Lattice QCD in Minkowski space-times

We now focus on defining fermion and gauge fields on a discretized spacetime, which is described by a hyper-cubic lattice. More precisely we discretize the space-time in temporal and spatial direction in a hyper-rectangular lattice

$$\Lambda = \{x : x = n_\mu \hat{a}^\mu, \quad n_\mu \in \mathbb{N}\}, \quad (2.3.1)$$

defined by spatial lattice distances a^i and temporal lattices distance a^0 . \hat{a}^μ are scaled unit vectors $a^\mu \hat{e}^\mu$ (no summation implied) and will be abbreviated for the rest of the work by $\hat{\mu}$. Note that this discretization is done for Minkowski space and not appropriate for the expanding case, which will be discussed afterwards. We will first define the most important aspects and later adapt it for longitudinally expanding space-times.

We further define the fermion fields on these lattice sites and define the discretized derivative as finite differences

$$\partial_\mu \psi(x) \rightarrow \frac{\psi_{x+\hat{\mu}} - \psi_{x-\hat{\mu}}}{2a}, \quad (2.3.2)$$

where we write the location of the fermion field in the subscript to distinguish it from the continuous field. We will do the same for all other quantities as well. The discretization for the derivative above leads to the so called “naive” discretization of the fermion action. This gives rise to the

problem of the fermion doubling (see [37]) which appears because there are additional symmetries added when this discretization is added. We do not discuss this problem in detail because we are solely interested in the dynamic of pure gauge systems without any fermions but want to emphasize that this discretization is not unique and can be improved. Nevertheless we will use this discretization to motivate the introduction of link fields. Another problem, which is independent of the discretization, is that the action is no longer gauge invariant. This is due to the fact that when inserting (2.3.2) into (2.2.4) we get terms of the form

$$\bar{\psi}_x \psi_{x+\hat{\mu}} \rightarrow \bar{\psi}'_x \psi'_{x+\hat{\mu}} = \bar{\psi}_x \Omega_x^\dagger \Omega_{x+\hat{\mu}} \psi_{x+\hat{\mu}} \quad (2.3.3)$$

and since $\Omega_x^\dagger \Omega_{x+\hat{\mu}}$ does not cancel identically we have destroyed the gauge invariance by introducing the discretization of the fermion field. As announced this motivates the introduction of link fields $U_{x\mu}$ which are defined on the connection of two lattice sites x and $x + \mu$. The index x specifies the starting site of the link and the index μ gives the direction to which neighboring site the link points to. Figure 2.1 shows an illustration of the link field at a certain lattice site.

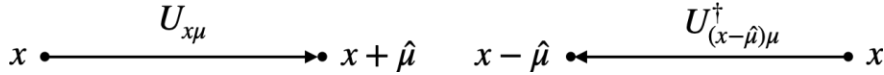


Figure 2.1: Illustration of link variables on a lattice.

The link variables are defined as elements of $SU(N_c)$ and we require the following transformation behavior and that the hermitian conjugate has the reversed direction of the link

$$U_{x\mu} \rightarrow \Omega_x U_{x\mu} \Omega_{x+\hat{\mu}}^\dagger, \quad U_{(x-\hat{\mu})\mu}^\dagger = U_{x(-\mu)}. \quad (2.3.4)$$

Substituting the derivative in (2.2.4) with

$$\partial_\mu \psi(x) \rightarrow \frac{U_{x\mu} \psi_{x+\hat{\mu}} - U_{x\mu}^\dagger \psi_{x-\hat{\mu}}}{2a}, \quad (2.3.5)$$

yields a gauge invariant version of the naively discretized fermion action. We will now justify the introduction of link variables and give them a physical interpretation.

Since the lattice formulation of QCD is built up by discretization of the continuum theory, it is natural that we want to find an analogous object in the continuum theory. In fact, we can identify a link variable $U_{x\mu}$ with the parallel transporter from the site x to the site y along some curve C_{xy}

$$U(C_{x,y}) = \mathcal{P} \exp \left[-i \int_{C_{x,y}} dx_\mu A_\mu(x) \right] \quad (2.3.6)$$

where \mathcal{P} is the path ordering operator which corresponds to the path C_{xy} . It can be shown that this parallel transporter satisfies

$$U(C_{x,y}) \rightarrow U(C_{x,y})' = \Omega(x) U(C_{x,y}) \Omega(y) \quad (2.3.7)$$

under gauge transformation and therefore has the same transformation behavior as the link variables on the lattice. We therefore define the link variables as

$$U_{x,\mu} = \exp \left[i a_\mu A_\mu \left(x + \frac{1}{2} \hat{\mu} \right) + \mathcal{O}(a_\mu^2) \right]. \quad (2.3.8)$$

Since we are mostly interested in the continuum limit or observing small lattice distances in our simulations we drop the $\mathcal{O}(a_\mu)$ terms from now on and take the obtained expression as definition of our link fields.

We will now focus on the gauge action. The simplest gauge-invariant object we can build with the link variables is the trace of a plaquette, which is a rectangle on the lattice that contains one link variable on each side as depicted in Figure 2.2. Mathematically they are given by

$$U_{x,\nu\mu} = U_{x,\nu}U_{x+\hat{\nu},\mu}U_{x+\hat{\mu},\nu}^\dagger U_{x,\mu}^\dagger, \quad (2.3.9)$$

where x in the subscript indicates the starting site of the plaquette and the Greek index pair distinguish the object from ordinary link variables and specify the orientation of the plaquette.

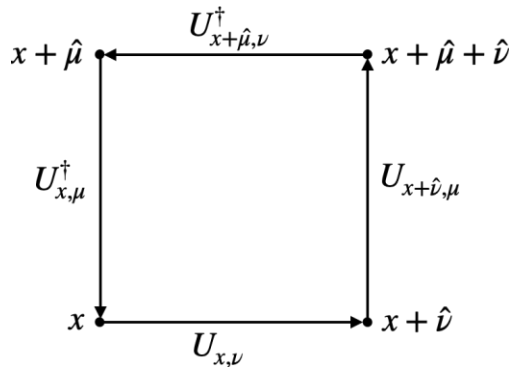


Figure 2.2: Illustration of a plaquette on a lattice.

We can now introduce the Wilson gauge action [38] as a sum of all positively oriented plaquettes. This action is given by

$$S_G[U] = \frac{2}{g^2} \sum_x \sum_{\mu < \nu} \text{Re tr} [\mathbb{1} - U_{x,\mu\nu}] \quad (2.3.10)$$

and it can be shown that it approaches the continuum gauge action for $a \rightarrow 0$ [36].

Lattice QCD in the Bjorken space-time

We will now turn to the lattice formulation in the boost invariant (τ, η) -frame. It will prove useful for numerical simulations to impose temporal gauge $A_0 = 0$. Starting from (2.2.17) we get

$$S_G[A] = \int d^4x \sqrt{-g(x^0)} \left[-\frac{1}{2} g^{jk}(x^0) \partial_0 A_j^a \partial_0 A_k^a - \frac{1}{4} F_a^{jk} F_{jk}^a \right]. \quad (2.3.11)$$

For the boost invariant case, we specify the Bjorken metric and split the integrand into transverse and non-transverse parts yielding

$$S_G[A] = \int d\tau d\eta d^2x^T \left[\frac{\tau}{2} \sum_{i=1,2} \partial_\tau A_i^a \partial_\tau A_i^a + \frac{1}{2\tau} \partial_\tau A_\eta^a \partial_\tau A_\eta^a - \frac{\tau}{4} \sum_{i,j=1,2} F_{ij}^a F_{ij}^a - \frac{1}{2\tau} \sum_{i=1,2} F_{i\eta}^a F_{i\eta}^a \right], \quad (2.3.12)$$

where in the last term we used the anti-symmetry of the field strength tensor. Furthermore, since we impose boost invariance in rapidity direction we have

$$F_{i\eta}^a = \partial_i A_\eta^a - \partial_\eta A_i^a + g f^{abc} A_i^b A_\eta^c = D_i^{ab} A_\eta^b, \quad (2.3.13)$$

where the covariant derivative in adjoint representation is given by

$$D_\mu^{ab} = \delta_{ab} \partial_\mu - g f^{abc} A_\mu^c. \quad (2.3.14)$$

We therefore obtain the following form of the boost invariant gauge action

$$S_G[A] = \int d\tau d\eta d^2 x^T \left[\frac{\tau}{2} \sum_{i=1,2} \partial_\tau A_i^a \partial_\tau A_i^a + \frac{1}{2\tau} \partial_\tau A_\eta^a \partial_\tau A_\eta^a - \frac{\tau}{4} \sum_{i,j=1,2} F_{ij}^a F_{ij}^a - \frac{1}{2\tau} \sum_{i=1,2} D_i^{ab} A_\eta^b D_i^{ac} A_\eta^c \right]. \quad (2.3.15)$$

We now discretize the integral in transverse plane by replacing the gauge fields $A_i(\tau, x^T)$, where x^T denotes the transverse coordinates, by the transverse gauge links

$$U_{x,i}(\tau) = \exp [i a_i A_i^a(\tau, x^T) t^a], \quad i = 1, 2. \quad (2.3.16)$$

To emphasize that we discuss the rapidity boost invariant case the arguments of the fields are written explicitly and the rapidity dependence is neglected. The plaquettes in the traverse plane are given by

$$U_{x,ij} = \exp [i a^i a^j F_{ij,x} + \mathcal{O}((a^i a^j)^2)], \quad i = 1, 2 \quad (2.3.17)$$

which is obtained by using the Baker-Campbell-Hausdorff-Formula

$$\exp[X] \exp[Y] = \exp \left[X + Y + \frac{1}{2}[X, Y] + \dots \right]. \quad (2.3.18)$$

Expanding the matrix exponential yields

$$U_{x,ij} = \mathbb{1} - (a^i a^j)^2 F_{ij,x}^2 + \mathcal{O}((a^i a^j)^3) \quad (2.3.19)$$

with which we get

$$F_{ij,x}^2 = \frac{2}{(a^i a^j)^2} \left(\mathbb{1} - \frac{1}{2} U_{x,ij} - \frac{1}{2} U_{x,ij}^\dagger \right) + \mathcal{O}((a^i a^j)^3). \quad (2.3.20)$$

The last piece that we need to discretize is the covariant derivative in transverse direction, which is achieved by replacing it with

$$D_i^B A_{\eta,x} = \frac{1}{a^i} \left(A_{\eta,x} - U_{x,i}^\dagger A_{\eta,x-\hat{i}} U_{x-\hat{i},i} \right). \quad (2.3.21)$$

It is also called backward derivative because of the direction of the step in the argument. Analogously we can define the forward derivative by going the reverse step. Finally we insert equations (2.3.20) and (2.3.21) into (2.3.15) and use

$$\partial_\tau U_{x,i}(\tau) = i a^i \partial_\tau A_i(\tau) U_{x,i}(\tau) \quad (2.3.22)$$

to obtain an expression for the semi-discretized, boost invariant gauge action given by

$$\begin{aligned}
 S_{G,latt}[A] = \int d\tau d\eta \sum_{x^1, x^2} a^1 a^2 \text{tr} \left[\tau \sum_{i=1,2} \frac{1}{(a^i)^2} \left(\partial_\tau U_{x,i}(\tau) \partial_\tau U_{x,i}^\dagger(\tau) \right) \frac{1}{\tau} (\partial_\tau A_\eta(\tau))^2 \right. \\
 \left. - \sum_{i,j=1,2} \frac{\tau}{(a^i a^j)^2} \left(\mathbb{1} - \frac{1}{2} U_{x,ij}(\tau) - \frac{1}{2} U_{x,ij}^\dagger(\tau) \right) \right. \\
 \left. - \frac{1}{\tau} \sum_{i=1,2} D_i^B A_{\eta,x} D_i^B A_{\eta,x} \right]. \quad (2.3.23)
 \end{aligned}$$

We identify the conjugate momentum with the chromo-electric field and obtain

$$\begin{aligned}
 E_x^i(\tau) &= \partial_\tau A_{x,i}(\tau) = -\frac{i\tau}{a^i} (\partial_\tau U_{x,i}(\tau)) U_{x,i}^\dagger(\tau), \\
 E_x^\eta(\tau) &= \frac{1}{\tau} \partial_\tau A_{x,\eta}(\tau).
 \end{aligned} \quad (2.3.24)$$

We now also derive an expression for the Hamiltonian on a lattice. For this it is practical to start with non-discretized action 2.3.11 and insert the identifications of the conjugate momenta with the chromo-electric fields, and obtain

$$S_G[A, E] = \int dx^0 d^3x \left[-\frac{1}{2\sqrt{-g(x^0)}} g_{jk}(\tau) E_a^j E_a^k - \frac{1}{4} F_{jk}^a F_a^{jk} \right], \quad (2.3.25)$$

where the summation over $j, k = 1, 2, 3$ is implied. The identification of the conjugate momenta also yields the effective Hamiltonian

$$H_G[A, E] = \int d^3x \left[-\frac{1}{2\sqrt{-g(x^0)}} g_{jk}(\tau) E_a^j E_a^k - \frac{1}{4} F_{jk}^a F_a^{jk} \right]. \quad (2.3.26)$$

This Hamiltonian can be discretized by approximating the integral with the sum over all spatial lattice sites and insert expression (2.3.20) for the field strength tensor

$$\begin{aligned}
 H_{G,latt}[U, E] = \sum_{x^i} a^3 \left[-\frac{1}{2\sqrt{-g(x^0)}} g_{jk}(x^0) E_{x,c}^j E_{x,c}^k \right. \\
 \left. + \frac{2N_c}{g^2} \sum_{j=1}^3 \sum_{k>j} C_{jk} \left(1 - \frac{1}{2N_c} \text{tr} U_{x,jk} - \frac{1}{2N_c} \text{tr} U_{x,jk}^\dagger \right) \right]. \quad (2.3.27)
 \end{aligned}$$

With this result we will derive the equations of motion on the lattice in Section 3.3.

2.4 Classical-statistical simulations

In this section our goal is to describe the classical statistical approximation we use for developing our numerical framework to simulate gauge systems. In similarity to [35] and [33] we will first give a short motivation starting from quantum mechanics and further expand the introduced concepts to quantum field theory.

A quantum system with the Hamilton operator $H(t)$ given in the Schrödinger picture can be fully described by the evolution of the density operator $\rho(t)$ which is given by

$$i \frac{\partial \rho}{\partial t} = [H(t), \rho(t)]. \quad (2.4.1)$$

This is known as the Liouville–von Neumann equation. Solving this equation yields

$$\rho(t) = U(t_0, t)\rho_0U(t_0, t), \quad (2.4.2)$$

$$U(t, t') = \int_{t'}^t dt'' H(t''). \quad (2.4.3)$$

The density operator at initial time ρ_0 is normalized such that $\text{tr}(\rho_0) = 1$ and represents all information about the system at initial time. Next, we can write the expectation value of any observable O in terms of the initial density

$$\langle O \rangle(t) = \text{tr}(\rho(t)O) = \text{tr}(\rho_0U(t, t_0)OU(t_0, t)). \quad (2.4.4)$$

Note that the observables O are time independent as we are still in the Schrödinger picture formulation. Since the time dependent observables in the Heisenberg picture are given by

$$O(t) = U(t, t_0)OU(t_0, t) \quad (2.4.5)$$

we can equivalently analyze those systems in the Heisenberg formulation. However, equation (2.4.4) makes it clear that the real time evolution of the expectation value of an observable O can be described by a closed time-path \mathcal{C} starting at t_0 leading to t and back to t_0 again on the real axis as illustrated in Figure 2.3. Figure 2.3 shows that we distinguish between the forward and

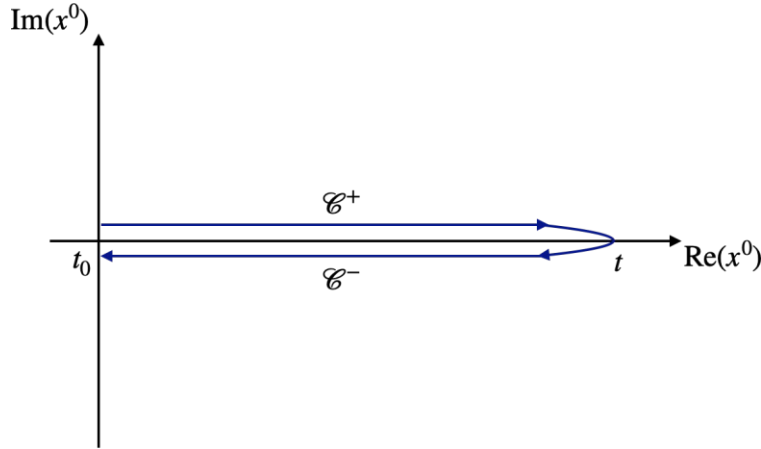


Figure 2.3: Illustration of a closed path on the real time axis.

subsequently backward branch of the contour \mathcal{C} , which we denote by \mathcal{C}^+ and \mathcal{C}^- respectively. \mathcal{C} is often referred to as the Schwinger-Keyldysh time contour.

We generalize this concept to quantum field theory by studying the generating functional

$$Z[J, R; \rho_0] = \text{tr} \left(\rho_0 \text{T}_{\mathcal{C}} \exp \left[i \int_{\mathcal{C}} dx^0 \int d^d x \sqrt{-g(x^0)} J_a(x) \Phi_a(x) + i \int_{\mathcal{C}} dx^0 \sqrt{-g(x^0)} \int d^d x \int_{\mathcal{C}} dy^0 \sqrt{-g(y^0)} \int d^d y R_{ab}(x, y) \Phi_a(x) \Phi_b(y) \right] \right). \quad (2.4.6)$$

Thereby we can express all n -point correlation functions in terms of functional derivatives with

respect to the source terms $J_a(x)$. The 1- and 2-point correlation functions are given by

$$\begin{aligned}\phi_a(x) &= \langle \Phi_a(x) \rangle = \frac{1}{\sqrt{-g(x^0)}} \frac{\delta Z[J, R; \rho_0]}{\delta J_a(x)} \Big|_{J=R=0}, & (\text{condensate}) \\ G_{ab}(x, y) &= \langle T_{\mathcal{C}} \Phi_a(x) \Phi_b(y) \rangle - \phi_a(x) \phi_b(y) & (\text{propagator}) \\ &= -\frac{1}{\sqrt{g(x^0)g(y^0)}} \frac{\delta^2 Z[J, R; \rho_0]}{\delta J_a(x) \delta J_b(y)} \Big|_{J=R=0} - \phi_a(x) \phi_b(y).\end{aligned}\quad (2.4.7)$$

The propagator can be decomposed into two terms

$$G_{ab}(x, y) = F_{ab}(x, y) - \frac{i}{2} \rho_{ab}(x, y) \text{sgn}_{\mathcal{C}}(x^0 - y^0) \quad (2.4.8)$$

where $\text{sgn}_{\mathcal{C}}$ yields 1 if x^0 is “later” on the contour \mathcal{C} than y^0 and otherwise -1 . F and ρ are called statistical and spectral correlation functions respectively. They are given by

$$F_{ab}(x, y) = \frac{1}{2} \langle \{\Phi_a(x) \Phi_b(y)\} \rangle - \phi_a(x) \phi_b(y), \quad (2.4.9)$$

$$\rho_{ab}(x, y) = i \langle [\Phi_a(x), \Phi_b(y)] \rangle. \quad (2.4.10)$$

The statistical correlation function is governed by how often states in the system are occupied. Information about the structure of the excitations is given by the spectral correlation function.

We will first discuss classical statistical simulations for scalar fields $\Phi_a(x)$ and later discuss the more complicated case of non-Abelian quantum fields.

J_a and R_{ab} denote linear and bi-linear source terms respectively. The time ordering operator $T_{\mathcal{C}}$ orders a product of operators it acts on such that they follow the forward time direction along the contour \mathcal{C} . It can be defined by its action on the product of two operators O_1, O_2

$$T_{\mathcal{C}} O_1(x) O_2(y) = \begin{cases} O_1(x) O_2(y), & \text{for } x \in \mathcal{C}^+, y \in \mathcal{C}^- \\ O_2(y) O_1(x), & \text{for } x \in \mathcal{C}^-, y \in \mathcal{C}^+ \\ O_1(x) O_2(y), & \text{for } x^0 \leq y^0 \wedge x, y \in \mathcal{C}^+ \\ O_2(y) O_1(x), & \text{for } x^0 \leq y^0 \wedge x, y \in \mathcal{C}^-.\end{cases} \quad (2.4.11)$$

We now introduce eigenstates and eigenvectors of the field operators $\Phi^{\pm}(t_0)$ on the start and end of the respective branches \mathcal{C}^{\pm}

$$\Phi^{\pm}(x^0 = t_0, x^i) |\varphi^{\pm}\rangle = \varphi_0^{\pm}(x^0 = t_0, x^i) |\varphi^{\pm}\rangle. \quad (2.4.12)$$

With these definitions we can rewrite the generating functional (2.4.6) as

$$\begin{aligned}Z[J, R; \rho_0] &= \\ &= \int [d\varphi_0^+] [d\varphi_0^-] \langle \varphi^+ | \rho_0 | \varphi^- \rangle \times \int_{\varphi_0^-}^{\varphi_0^+} \mathcal{D}' \varphi \left(e^{i(S_{\mathcal{C}} + \int_{x, \mathcal{C}} J_a(x) \Phi_a(x) + \frac{1}{2} \int_{xy, \mathcal{C}} R_{ab} \Phi_a(x) \Phi_b(y))} \right)\end{aligned}\quad (2.4.13)$$

which was shown in [35]. Here we have introduced the shorthand notation

$$\int_{x, \mathcal{C}} = \int dx^0 \sqrt{g(x_0)} \int d^d x, \quad \int_{xy, \mathcal{C}} = \int dx^0 \sqrt{g(x_0)} \int d^d x \int dy^0 \sqrt{g(y_0)} \int d^d y. \quad (2.4.14)$$

We successfully factorized the generating functional in two factors of which the first is determined by the initial conditions of the scalar system. The (pseudo) integration measures are given by

$$\int [d\varphi_0^{\pm}] = \int \prod_{a=1}^N \prod_{x^i} d\varphi_{a,0}(x^i). \quad (2.4.15)$$

The second factor in (2.4.13) is determined by the classical action S_C on the forward and backward branch of the contour given by

$$S_C = S[\varphi^+] - S[\varphi^-],$$

$$S[\varphi] = \int d^4x \sqrt{-g(x^0)} \left(\frac{1}{2} g^{\mu\nu}(x^0) (\partial_\mu \varphi_a) (\partial_\nu \varphi_a) - \frac{\lambda}{24N} (\varphi_a \varphi_a)^2 \right) \quad (2.4.16)$$

and the source terms. It is therefore governed by the quantum dynamics of the system. N denotes the number of scalar components a of the field and λ represents the coupling constant. For this part the path integral $\int_{\varphi_0^-}^{\varphi_0^+} \mathcal{D}'$ excludes the endpoints x of the time contour \mathcal{C} with $x^0 = t_0^\pm$ and implicitly imposes $\varphi(x^0 = t_0^\pm) = \varphi_0^\pm$.

We now split the classical action S by introducing the scalar fields

$$\varphi = \frac{\varphi^+ + \varphi^-}{2}, \quad \tilde{\varphi} = \varphi^+ - \varphi^- \quad (2.4.17)$$

such that the classical action can be written as

$$S[\varphi, \tilde{\varphi}] = S_0[\varphi, \tilde{\varphi}] + S_{cl}^{int}[\varphi, \tilde{\varphi}] + S_{qu}^{int}[\varphi, \tilde{\varphi}]. \quad (2.4.18)$$

They denote the non-interacting, the classical interaction and the quantum interaction contributions respectively. The terms are obtained by substituting

$$\varphi^+ = \frac{2\varphi + \tilde{\varphi}}{2}, \quad \varphi^- = \frac{2\varphi - \tilde{\varphi}}{2} \quad (2.4.19)$$

into (2.4.16) and separating the expression such that

$$S_0[\varphi, \tilde{\varphi}] = \int_{\mathcal{C}^+} d^4x \sqrt{-g(x^0)} g^{\mu\nu} \partial_\mu \tilde{\varphi}_a(x) \partial_\nu \tilde{\varphi}_a(x),$$

$$S_{cl}^{int}[\varphi, \tilde{\varphi}] = -\frac{\lambda}{6N} \int_{\mathcal{C}^+} d^4x \sqrt{-g(x^0)} \tilde{\varphi}_a(x) \varphi_a(x) \varphi_b(x) \varphi_b(x), \quad (2.4.20)$$

$$S_{qu}^{int}[\varphi, \tilde{\varphi}] = -\frac{\lambda}{24N} \int_{\mathcal{C}^+} d^4x \sqrt{-g(x^0)} g^{\mu\nu} \tilde{\varphi}_a(x) \tilde{\varphi}_a(x) \tilde{\varphi}_b(x) \varphi_b(x).$$

Using the inverse product rule on $S_0[\varphi, \tilde{\varphi}]$ we obtain

$$S_0[\varphi, \tilde{\varphi}] = \int_{\mathcal{C}^+} d^4x \sqrt{-g(x^0)} g^{\mu\nu} \partial_\mu (\tilde{\varphi}_a(x) \partial_\nu \tilde{\varphi}_a(x))$$

$$+ \int_{\mathcal{C}^+} d^4x \sqrt{-g(x^0)} g^{\mu\nu} \tilde{\varphi}_a(x) \partial_\mu \partial_\nu \varphi_a(x). \quad (2.4.21)$$

With this result we can now define the classical action

$$S_{cl}[\varphi, \tilde{\varphi}] = \int_{\mathcal{C}^+} d^4x \sqrt{-g(x^0)} \tilde{\varphi}_a(x) \left(g^{\mu\nu} \partial_\mu \partial_\nu \varphi_a(x) - \frac{\lambda}{6N} \varphi_a(x) \varphi_b(x) \varphi_b(x) \right). \quad (2.4.22)$$

Since the explicit expression for (2.4.21) is metric dependent we will proceed by sticking to the Minkowski metric for the rest of the discussion of classical-statistical simulations. In the above expression we introduced the canonical momentum field given by

$$\pi_{0,a} = \sqrt{-g(x^0)} \varphi_{0,a}. \quad (2.4.23)$$

We can now easily rewrite the non-interaction part of the action by

$$S_0[\varphi, \tilde{\varphi}] = - \int d^3x \pi_{0,a} \tilde{\varphi}_{0,a}(x) - \int_{\mathcal{C}^+} d^4x \tilde{\varphi}_a(x) \partial^\mu \partial_\nu \varphi_a(x) \quad (2.4.24)$$

and write the classical action as

$$S_{cl}[\varphi, \tilde{\varphi}] = \int d^3x \pi_{0,a} \tilde{\varphi}_{0,a}(x) + S_0[\varphi, \tilde{\varphi}] + S_{cl}^{int}[\varphi, \tilde{\varphi}]. \quad (2.4.25)$$

We can further introduce the substitutions of the scalar fields above in the initial condition term in the generating functional (2.4.13) and obtain

$$\begin{aligned} \int [d\varphi_0^+] [d\varphi_0^-] \langle \varphi^+ | \rho_0 | \varphi^- \rangle &= \int [d\tilde{\varphi}_0] [d\tilde{\varphi}_0] \left\langle \varphi_0 + \frac{\tilde{\varphi}_0}{2} \middle| \rho_0 \middle| \varphi_0 - \frac{\tilde{\varphi}_0}{2} \right\rangle \\ &= \int [d\tilde{\varphi}_0] [d\tilde{\varphi}_0] [d\pi_0] W[\phi_0, \pi_0] \exp \left(i \int d^3x \pi_{0,a} \tilde{\varphi}_{0,a}(x) \right) \end{aligned} \quad (2.4.26)$$

where $W[\phi_0, \pi_0]$ is the Wigner transformation of the initial density matrix. Combining the results of (2.4.25) and (2.4.26) by plugging them into (2.4.13) leads to

$$Z[J, R; \rho_0] = \int [d\tilde{\varphi}_0] [d\pi_0] W[\phi_0, \pi_0] \int \mathcal{D}'\varphi \mathcal{D}\tilde{\varphi} \exp \left(i S_{cl}[\varphi, \tilde{\varphi}] + S_{qu}^{int}[\varphi, \tilde{\varphi}] + \text{source terms} \right). \quad (2.4.27)$$

The *source terms* are given by substituting φ and $\tilde{\varphi}$ in the linear and bilinear source terms of (2.4.13).

When we rewrite the classical action $S_{cl}[\varphi, \tilde{\varphi}]$ in terms of the original scalar action we obtain

$$S_{cl}[\varphi, \tilde{\varphi}] = \int_{\mathcal{C}^+} d^4x \tilde{\varphi}_a(x) \frac{\delta S[\varphi]}{\delta \varphi_a}. \quad (2.4.28)$$

Finally, we can introduce the classical approximation of the above generating functional by simply dropping the quantum interaction term $S_{qu}^{int}[\varphi, \tilde{\varphi}]$. We observe that the classical part of the generating functional

$$\int \mathcal{D}\tilde{\varphi} \exp \left(i S_{cl}[\varphi, \tilde{\varphi}] \right) = \int \mathcal{D}\tilde{\varphi} \exp \left(i \int_{\mathcal{C}^+} d^4x \tilde{\varphi}_a(x) \frac{\delta S[\varphi]}{\delta \varphi_a} \right) = \delta \left[\frac{\delta S[\varphi]}{\delta \varphi} \right] \quad (2.4.29)$$

yields a Delta functional. Hence, with the classical equation of motion given by

$$\frac{\delta S[\varphi]}{\delta \varphi} = 0 \quad (2.4.30)$$

this justifies the term classical approximation.

Range of validity of the classical approximation

We now discuss the range of validity for the classical approximation presented above. We restate the generating functional by inserting a Delta functional and obtain

$$\begin{aligned} Z[J, R; \rho_0] &= \int [d\varphi_0] [d\pi_0] W[\varphi_0, \pi_0] \int \mathcal{D}'\varphi \mathcal{D}\tilde{\varphi} \exp \left(i S_{cl}[\varphi, \tilde{\varphi}] \right) \\ &= \int [d\varphi_0] [d\pi_0] W[\varphi_0, \pi_0] \int \mathcal{D}'\varphi \delta[\varphi_{cl} = \varphi] \\ &= \int [d\varphi_0] [d\pi_0] W[\varphi_0, \pi_0] |_{\varphi_{cl} = \varphi}. \end{aligned} \quad (2.4.31)$$

Note, that rewriting the Delta functional as $\delta[\varphi_{cl} = \varphi]$ holds only up to a Jacobian which is neglected since it only represents physically irrelevant normalization constant [35]. We dropped all source terms in order to make the presentation more clear.

As can be seen in (2.4.20) the contributions to the full action can be categorized into two types of vertices as depicted in Figure 2.4. Note that the only difference in the vertices are the types

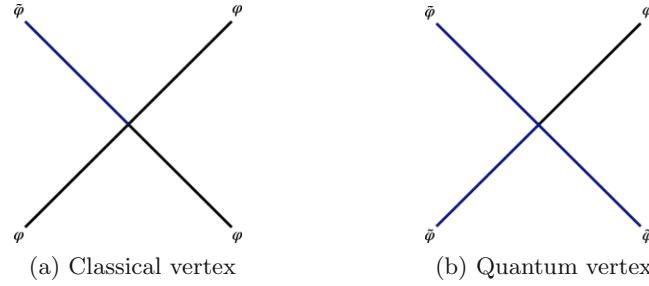


Figure 2.4: Illustration of 4-point vertices diagrams contributing to the full action.

of legs (scalar fields) connected by these vertices. Hence, in order to understand the contributions we need to introduce the correlation functions which connect those legs. In essence the classical statistical approximation neglects all Feynman diagrams which include quantum vertices in Figure 2.4b. The generating functional for connected correlation functions is defined by

$$W[J, R] = -i \ln Z[J, R]$$

The functional derivatives yield the correlation functions

$$\begin{aligned}
 \text{Statistical correlation function:} \quad F_{ab}(x, y) &= \frac{\delta^2 iW[J, R]}{\delta i\tilde{J}_a(x)\delta i\tilde{J}_b(y)} \Big|_{J=\tilde{J}=0}, \\
 \text{Retarded propagator:} \quad -iG_{ab}^R(x, y) &= \frac{\delta^2 iW[J, R]}{\delta i\tilde{J}_a(x)\delta iJ_b(y)} \Big|_{J=\tilde{J}=0} \\
 &= \Theta(x^0 - y^0)\rho_{ab}(x, y), \\
 \text{Advanced propagator:} \quad -iG_{ab}^A(x, y) &= \frac{\delta^2 iW[J, R]}{\delta iJ_a(x)\delta i\tilde{J}_b(y)} \Big|_{J=\tilde{J}=0} \\
 &= \Theta(y^0 - x^0)\rho_{ab}(x, y), \\
 \text{Anomalous propagator:} \quad \tilde{F}_{ab}(x, y) &= \frac{\delta^2 iW[J, R]}{\delta iJ_a(x)\delta iJ_b(y)} \Big|_{J=\tilde{J}=0} = 0.
 \end{aligned} \tag{2.4.32}$$

In Figure 2.5 an illustration of the correlation functions in terms of Feynman sub-diagrams is given. It shows that the spectral correlation function F connects to a φ leg whereas the retarded correlation function G^R connects a φ leg to an $\tilde{\varphi}$ leg and vice versa for the advanced correlation function G^A . All Feynman diagrams which include one of sub-diagrams depicted in Figures 2.5b and 2.5c have to be dropped in the classical approximation because they include quantum vertices. Therefore we need to characterize systems where the contributions of those diagrams is negligible.

All 4-point vertices are either classical or quantum type vertices, therefore we have in fact constructed all one-loop Feynman sub-diagrams in Figure 2.5. We need to sum over all of their contributions in order to get there relative contributions to the action. Hence, we find that the condition for the validity of the classical approximation is given by

$$(G^A)^2(x, y) + (G^R)^2(x, y) \ll F^2(x, y). \tag{2.4.33}$$

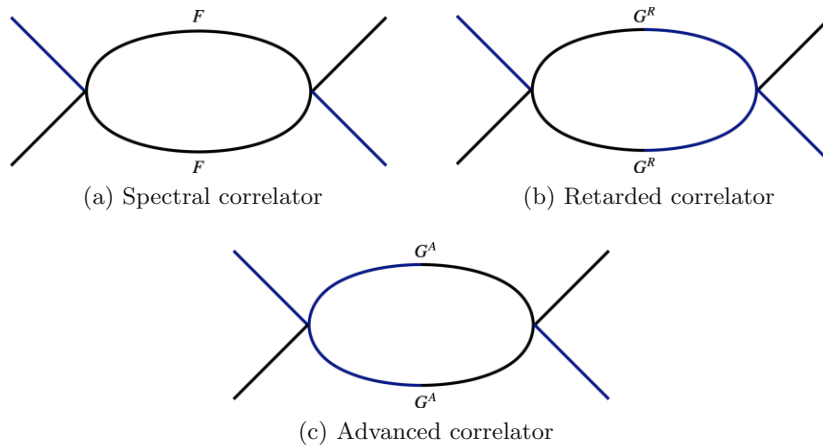


Figure 2.5: Illustration of Feynman diagrams contributing to the full action.

We can further rewrite this condition by using (2.4.32) to obtain

$$\rho_{ab}(x, y) = G_{ab}^R(x, y) - G_{ab}^A(x, y), \quad G_{ab}^R(x, y)G_{ab}^A(x, y) = 0 \quad (2.4.34)$$

which yields

$$\rho^2(x, y) \ll F^2(x, y). \quad (2.4.35)$$

Next, we will continue by restating this condition using the distribution function of the system.

Spectral function and 1- and 2-point correlation functions

We will now derive a single-particle distribution function in momentum space. With this function we can reformulate the validity condition (2.4.35) with the advantage of the clearer interpretation of occupancy numbers.

For homogeneous systems we denote the expectation value of $\Phi_a(x)$ and the canonical momentum $\Pi_a(x)$ by

$$\phi_a(x^0) = \langle \Phi_a(x) \rangle, \quad \pi_a(x^0) = \langle \Pi_a(x) \rangle. \quad (2.4.36)$$

Writing the spatial and temporal dependencies explicitly gives us

$$F_{ab}(x^0, x^{0'}, x^i - x^{i'}) = \frac{1}{2} \langle \{ \Phi_a(x^0, x^i), \Phi_a(x^{0'}, x^{i'}) \} \rangle - \phi_a(x^0)\phi_b(x^{0'}). \quad (2.4.37)$$

We can Wigner transform this expression at equal time in order to obtain

$$F(x^0, p^i) = \frac{1}{N} \sum_{a=1}^N F_{aa}(x^0, x^0, p^i). \quad (2.4.38)$$

Note that in case of the longitudinally expanding Bjorken metric we identify the longitudinal component of the momentum by $p^3 = \nu/\tau$, where ν is the rapidity wave number [33]. The transverse momentum components p_T stay the same as with the Minkowski metric.

Before we give a definition for a distribution function we want to emphasize that this definition is not unique. We introduce the distribution function as a decomposing of the statistical correlation function. We can write the statistical and spectral correlation function in Wigner coordinates

$$X^\mu = \frac{x^\mu + y^\mu}{2}, \quad s^\mu = x^\mu - y^\mu \quad (2.4.39)$$

and Fourier transform them with respect to the coordinates s^μ . Since we are considering spatially homogeneous systems we can drop the X^i dependence and arrive at

$$F(p^\mu, X^0) = -i \left(f(p^\mu, X^0) + \frac{1}{2} \right) \rho(p^\mu, X^0). \quad (2.4.40)$$

We further assume that the system has a free spectral function

$$\rho(p^\mu, X^0) = -2\pi \operatorname{sgn}(p^0) \delta((p^0)^2 - \omega^2(p^i)) \quad (2.4.41)$$

where $\omega(p^i)$ is given by the dispersion relation. Integrating over $p^0 > 0$ of (2.4.40) yields

$$f(x^0, p^i) + \frac{1}{2} = \int_0^\infty \frac{dp^0}{2\pi} 2p^0 F(p^\mu, x^0). \quad (2.4.42)$$

It can be shown that all definitions assuming free spectral functions (2.4.41) are equivalent [33]. Yet another equivalent approach for defining the distribution function over so-called mode vectors will be discussed in Section 2.5 for non-Abelian gauge theories.

With the definition of the distribution function in (2.4.42) and its relation with the statistical correlator function (2.4.40) we can reformulate the validity condition (2.4.35) as

$$f(x^0, p^i) \gg \frac{1}{2}. \quad (2.4.43)$$

Hence, we see that the classical approximation is only valid for high occupation numbers. This also means that the range of validity is also restricted to weakly coupled systems with $\lambda \ll 1$ because otherwise the occupancy numbers become too small after a short duration and the system does not satisfy the validity condition anymore.

Similar to the discussion above we can define a single-particle distribution function and introduce the classical approximation for gauge systems; a comprehensive discussion is given in [33]. In the following section we will introduce observables including a distribution function for pure gauge theories also known as Yang Mills theories.

2.5 Observables

In this chapter we introduce observables we will later calculate in the conducted classical-statistical simulations. We express the stress-energy tensor in terms of the field strength tensor, which yields

$$T_{\mu\nu}(x^\mu) = -g^{\rho\sigma}(x^0) F_{\mu\rho}^a F_{\nu\sigma}^a + \frac{1}{4} g_{\mu\nu}(x^0) F_{\sigma\rho}^a F_a^{\sigma\rho} \quad (2.5.1)$$

in the adjoint representation.

Energy density and pressure

We express the energy density and the transverse and longitudinal pressure in terms of stress-energy tensor components and obtain

$$\begin{aligned} \varepsilon(x^0) &= \langle T_0^0 \rangle, \\ P_T(x^0) &= -\frac{1}{2} \langle T_1^1 + T_2^2 \rangle, \\ P_L(x^0) &= -\langle T_3^3 \rangle. \end{aligned} \quad (2.5.2)$$

We separate the energy density in the contributions of the chromo-electric and chromo-magnetic fields and obtain

$$\varepsilon(x^0) = \varepsilon_{E_T}(x^0) + \varepsilon_{E_L}(x^0) + \varepsilon_{B_T}(x^0) + \varepsilon_{B_L}(x^0), \quad (2.5.3)$$

which are given by

$$F_{ij,x}^2 = \frac{2}{(a^i a^j)^2} \left(\mathbb{1} - \frac{1}{2} U_{x,ij} - \frac{1}{2} U_{x,ij}^\dagger \right) + \mathcal{O}((a^i a^j)^3). \quad (2.5.4)$$

$$\begin{aligned} \varepsilon_{E_T}(x^0) &= \frac{1}{2} \langle E_a^i E_a^i \rangle \approx \frac{1}{2N^2} \sum_x F_{x,a}^{0i} F_{x,a}^{0i}, \\ \varepsilon_{E_L}(x^0) &= \frac{1}{2} \langle E_a^3 E_a^3 \rangle \approx -\frac{1}{2N^2 g(x^0)} \sum_x F_{x,a}^{03} F_{x,a}^{03}, \\ \varepsilon_{B_T}(x^0) &= \frac{1}{2} \langle B_a^i B_a^i \rangle \approx -\frac{1}{2N^2 g(x^0)} \sum_x F_{x,a}^{i3} F_{x,a}^{i3}, \\ \varepsilon_{B_L}(x^0) &= \frac{1}{2} \langle B_a^3 B_a^3 \rangle \approx \frac{1}{4N^2} \sum_x F_{x,a}^{ij} F_{x,a}^{ij}, \end{aligned} \quad (2.5.5)$$

where the summation over $i, j = 1, 2$ and $a = 1, \dots, N_c^2 - 1$ is implied. The expectation value on the lattice is calculated by the ensemble average over all lattice sites. Inserting expression (2.3.20) for the discretized field strength tensor yields the the energy density components in terms of the link fields. Rewriting the pressure components yields

$$\begin{aligned} P_T(x^0) &= \varepsilon_{E_L}(x^0) + \varepsilon_{B_L}(x^0) \\ P_L(x^0) &= \varepsilon_{E_L}(x^0) + \varepsilon_{B_L}(x^0) - \varepsilon_{E_T}(x^0) - \varepsilon_{B_T}(x^0). \end{aligned} \quad (2.5.6)$$

Note that the expressions of the energy density and pressure components are gauge invariant quantities and therefore are physical meaningful observables.

Occupation numbers and correlation functions

We will now turn to the definition of particle numbers in weakly interacting 2+1 dimensional gauge theories. In order to motivate a quasi-free particle picture we expand the gauge fields in terms of mode vectors $\xi_{j,p^i}^{(\lambda)}$ which are solutions of the free equations of motion $D_\mu F^{\mu\nu} = 0$ with vanishing coupling constant $g = 0$. We will present a brief summary for the solution of these equation and refer to the technical calculation to [34] and [32].

Imposing temporal gauge $a_\tau = 0$ yields the following form for the free equations of motion

$$\begin{aligned} \partial_\tau \partial_\tau a_i + \tau \left(p_\perp^2 + \frac{\nu^2}{\tau^2} \right) a_i - \tau p_i p_j a_j - \frac{\nu}{\tau} p_i a_\eta &= 0, \quad i, j = 1, 2 \\ \partial_\tau \tau^{-1} \partial_\tau a_\eta + \tau^{-1} p_T^2 a_\eta - \frac{\nu}{\tau} p_i a_i &= 0, \quad i = 1, 2 \end{aligned} \quad (2.5.7)$$

as shown in [39, 40]. We denote the free solutions of these equations by a lower case a_μ to distinguish them from the general gauge fields. Further, we abbreviate the transverse momentum by $p_T^2 = p_1^2 + p_2^2$ and require the solution to fulfill the Gauss constraint

$$p_i \tau \partial_\tau a_i + \frac{\nu}{\tau} \partial_\tau a_\eta = 0 \quad (2.5.8)$$

and fix the remaining gauge freedom with the Coulomb type gauge given by

$$\tau p_i a_i + \frac{\nu}{\tau} a_\eta = 0. \quad (2.5.9)$$

We can write the free solution in terms of polarization vectors which yields

$$a_{j,p_T,\nu}^{(\lambda)}(x) = \xi_{j,p_T,\nu}^{(\lambda)}(\tau) e^{i(p^i x^i + \nu \eta)} \quad (2.5.10)$$

where $\lambda = 1, 2, 3$ denote different polarizations. The polarizations $\lambda = 1, 2$ denote two transversal polarization while $\lambda = 3$ denotes the longitudinal polarization direction. Inserting the longitudinal mode vector

$$\xi_{j,p_T,\nu}^{(3)}(\tau) = \begin{pmatrix} p_1 \\ p_2 \\ \nu \end{pmatrix} \xi_{p_T,\nu}^{(3)}(\tau) \quad (2.5.11)$$

into the Gauss constraint yields $\partial_\tau \xi_{p_T,\nu}^{(3)}(\tau) = 0$. We therefore obtain a vanishing longitudinal mode vectors $\xi_{p_T,\nu}^{(3)}(\tau) = 0$ when employing the Coulomb gauge. The other polarizations which specify the directions of the mode-vectors can be formulated in terms of Hankel function - for an explicit form for the mode vectors $\xi_{j,p_T,\nu}^{(\lambda)}(\tau)$ we refer to [32], [34].

The first transversal mode vector

$$\xi_{j,p_T,\nu}^{(1)}(\tau) = \begin{pmatrix} -p_2 \\ p_1 \\ \nu \end{pmatrix} \xi_{p_T,\nu}^{(1)}(\tau) \quad (2.5.12)$$

yields $a_{\eta,p_T,\nu}^{(1)}(\tau) = 0$. When inserting this solution into the free equations of motion (2.5.7) we obtain

$$\left(\partial_\tau^2 + \frac{1}{\tau} \partial_\tau + p_T^2 + \left(\frac{\nu}{\tau} \right)^2 + m^2(\tau) \right) \xi_{p_T,\nu}^{(1)}(\tau) = 0. \quad (2.5.13)$$

This equation corresponds to the free dispersion relation for the longitudinally expanding case given by

$$\omega(p_T, \nu, \tau)^2 = p_T^2 + \left(\frac{\nu}{\tau} \right)^2 + m^2(\tau). \quad (2.5.14)$$

where a vanishing mass term $m^2(\tau) = 0$ is assumed. We identify this mode-vector $\xi_{j,p_T,\nu}^{(1)}$ with the gluonic part of the color-fields and the mode vector $\xi_{j,p_T,\nu}^{(2)} = (0, 0, \xi_{\eta,p_T,\nu}^{(2)})^T$ with the scalar part.

We assume the expansion of gauge fields A_j^a in terms of the mode vectors and obtain

$$A_j^a(t_0, x^i) = \int \frac{d^3 \tilde{p}}{(2\pi)^3} \left(\alpha_{a,\tilde{p}^i}^{(\lambda)} \xi_{j,\tilde{p}^i}^{(\lambda)}(t^0) e^{i\tilde{p}^i x^i} + \alpha_{a,\tilde{p}^i}^{(\lambda)*} \xi_{j,\tilde{p}^i}^{(\lambda)*}(t^0) e^{-i\tilde{p}^i x^i} \right). \quad (2.5.15)$$

Assuming the expansion of the chromo-electric field in terms of the mode vectors yields

$$E_a^j(t_0, x^i) = \sqrt{-g(t^0)} g^{jk}(t_0) \int \frac{d^3 \tilde{p}}{(2\pi)^3} \left(\alpha_{a,\tilde{p}^i}^{(\lambda)} \partial_0 \xi_{j,\tilde{p}^i}^{(\lambda)}(t^0) e^{i\tilde{p}^i x^i} + \alpha_{a,\tilde{p}^i}^{(\lambda)*} \partial_0 \xi_{j,\tilde{p}^i}^{(\lambda)*}(t^0) e^{-i\tilde{p}^i x^i} \right). \quad (2.5.16)$$

Note, that the mode vectors above satisfy the normalization condition

$$\xi_{j,\tilde{p}^i}^{(\lambda)}(x^0) \overleftrightarrow{\partial}_0 \xi_{j,\tilde{p}^i}^{(\lambda)*}(x^0) = \frac{i}{\sqrt{-g(x^0)}}, \quad (2.5.17)$$

where we have written \tilde{p}^i to emphasize that the third component of the momentum depends on the imposed metric. With this expansion we can further define the analogous objects to annihilation and creation operators in quantum mechanics

$$\alpha_{a,\tilde{p}^i}^{(\lambda)}(x^0) = i\sqrt{-g(x^0)} \int d^3x e^{-ix^i\tilde{p}^i} g^{jk}(x^0) \left(\xi_{j,\tilde{p}^i}^{(\lambda)*}(x^0) \overleftrightarrow{\partial}_0 A_k^a(x^\mu) \right). \quad (2.5.18)$$

Indeed, the condition (2.5.17) is chosen such that the generalizations of the fields A and E to quantum fields satisfy suitable commutation relations.

In Section 3.2 we will impose the Gauss constraint and the Coulomb gauge which read

$$D_j E^j = 0, \quad -g^{ij} \partial_i A_j = 0. \quad (2.5.19)$$

Note that since we impose the temporal gauge $A^0 = 0$ in our simulations the Coulomb gauge condition is not conserved during the simulation and has to be restored at each time we calculate the observables which are not gauge invariant. With these conditions the third polarization, which is the polarization parallel to the p^i direction, vanishes $\alpha_{a,p^i}^{(3)} = 0$ and can therefore be neglected. In analogy to the quantum theory we can now define occupation numbers as

$$f_{gluon}(x^0, \tilde{p}^i) = \frac{1}{(N_c^2 - 1)} \sum_{a=1}^{N_c^2 - 1} \left\langle |\alpha_{a,\tilde{p}^i}^{(1)}(x^0)|^2 \right\rangle, \quad (2.5.20)$$

$$f_{scalar}(x^0, \tilde{p}^i) = \frac{1}{(N_c^2 - 1)} \sum_{a=1}^{N_c^2 - 1} \left\langle |\alpha_{a,\tilde{p}^i}^{(2)}(x^0)|^2 \right\rangle, \quad (2.5.21)$$

where we distinguish between scalar and gluonic distributions. We emphasize that this definition is gauge dependent and not unique. As already discussed we impose the Coulomb gauge in order to make this quantity physically meaningful.

For the definition above we have assumed that the observed system is weakly interacting $g \rightarrow 0$ and that the mass is vanishing $m = 0$. These assumptions were imposed in order to use Hankel functions for the solution of the free equations of motion in the expanding space-time. We make clear that this definition is not ideal because it is known that gluons create an effective mass which should be taken into account in the particle definition since this mass contributes to the dispersion relation. We will use this definition despite its complications since we use the mode vector expansion in order to initialize the fields according to a specified distribution function. For more details about the initial conditions see Section 3.2. Furthermore we are focusing on the large momentum occupancy numbers for our analysis which is expected to not to be disturbed by the creation of effective gluon and scalar masses.

A different definition is motivated by the Hamilton formalism of scalar field theory and assuming the free dispersion relation [41]. It is suggested to define the occupation numbers as

$$f(\tau, p_T) = \frac{2}{N^2 p_T} \left[\frac{1}{2\tau} \sum_{i=1,2} E_i^a(p_T) E_i^a(-p_T) + \frac{\tau}{2} E_3^a(p_T) E_3^a(-p_T) \right] \quad (2.5.22)$$

for the expanding case on the lattice. With this definition it was shown that $\omega(p_T) \approx p_T$ which justifies using the free dispersion relation $\omega(p_T)^2 = p_T^2 + m^2$ and neglecting the mass term.

This definition motivates the separation of the total occupation numbers in a purely gluonic contribution given by the transversal field components and a scalar part

$$f(\tau, p_T) = f_{gluons}(\tau, p) + f_{scalars}(\tau, p). \quad (2.5.23)$$

The approach in (2.5.22) amounts to the following definitions of the respective occupation numbers

$$\begin{aligned}
 f_{gluon}(\tau, p_T) &= \frac{1}{\omega(p_T)} \sum_{i=1,2} \langle E_i^a E_i^{a*} \rangle, \\
 f_{scalar}(\tau, p_T) &= \frac{1}{\omega(p_T)} \langle E_3^a E_3^{a*} \rangle,
 \end{aligned}
 \tag{2.5.24}$$

where we assume $\omega(p_T) \approx p_T$. A similar definition was also used in [31]. We therefore also include equal time correlation functions in our analysis.

Using mode vectors to define the occupation numbers yields the possibility of projecting out the polarization components to distinguish between the gluonic and the scalar particle numbers. This enables us to use our original occupancy definitions (2.5.20), (2.5.21) and distinguish both contributions during the simulation.

Another single-particle number definition which does not rely on the free dispersion relation was suggested in [41]. By interpreting the longitudinal field components as scalar fields we can translate the suggested definition to

$$f_{gluon}(\tau, p_T) = \frac{1}{\tau} \sqrt{\langle E_i^a E_i^{a*} \rangle \langle A_j^a A_j^{a*} \rangle}, \quad f_{scalar}(\tau, p_T) = \tau \sqrt{\langle E_3^a E_3^{a*} \rangle \langle A_3^a A_3^{a*} \rangle}.
 \tag{2.5.25}$$

The dispersion relations for gluonic and scalar contributions can be approximated by

$$\omega_{gluon}(\tau, p_T) = \frac{1}{\tau} \sqrt{\frac{\langle E_i^a E_i^{a*} \rangle}{\langle A_j^a A_j^{a*} \rangle}}, \quad \omega_{scalar}(\tau, p_T) = \tau \sqrt{\frac{\langle E_3^a E_3^{a*} \rangle}{\langle A_3^a A_3^{a*} \rangle}},
 \tag{2.5.26}$$

where the summations over $i = 1, 2$ and $j = 1, 2$ is implied.

Chapter 3

Initial Conditions

In this section we introduce two types of initial conditions for 2+1 dimensional gauge systems which provide examples for gauge systems that are far from equilibrium. We discuss the so-called Glasma which is described by the McLerran-Venugopalan model. This model is motivated by two colliding ultra-relativistic nuclei and describes the first (very short) period of the gluonic system after the collision where boost invariance can be assumed. Thereafter we discuss Gaussian initial conditions which pose a second example of a gauge system far from equilibrium. Both systems are analyzed by conducting classical-statistical simulations. In Section 3.1 and Section 3.2 we will provide a description of both initial conditions and afterwards restate them in the lattice formulation. Next, in Section 3.3 we discuss the equations of motions given by the classical statistical approximation discussed in Section 2.4 and formulate the update rules we use in our lattice simulations.

3.1 Glasma Initial Conditions

Continuum formulation of the McLerran-Venugopalan model

We introduce initial conditions which describe two nuclei colliding in an ultra relativistic heavy-ion collision. Specifically we adopt the McLerran-Venugopalan model often referred to as the MV-model which was introduced in [28]. Since we assume the energy in this collision to be very high the Lorentz contraction justifies the assumption of a peaked charged density distribution in direction of the collision trajectory. Additionally, we assume that the nuclei collide head on and therefore the so-called color sheets, which describe the charge distributions of the nuclei, are parallel to each other. Importantly the high energy nuclei translate to large number gluons which means that the MV-model describes a highly occupied system. Hence, as it was shown in Section 2.4 the contribution from quantum vertices in the gauge action can be neglected and the classical approximation is justified.

We first employ light cone coordinates in order to solve the classical Yang-Mills equation

$$D_\mu F^{\mu\nu} = J^\nu, \quad (3.1.1)$$

where J^ν denotes the color charge current. Light cone coordinates are given by

$$x^\pm = \frac{x^0 \pm x^3}{\sqrt{2}}, \quad t = x^0, \quad z = x^3, \quad (3.1.2)$$

and yield the following form of the Minkowski metric

$$g_{LC}^{\mu\nu} = \begin{pmatrix} 0 & 1 & 0 & 0 \\ 1 & 0 & 0 & 0 \\ 0 & 0 & -1 & 0 \\ 0 & 0 & 0 & -1 \end{pmatrix}^{\mu\nu}. \quad (3.1.3)$$

We consider a nucleus moving in longitudinal direction which gives us the following form for the color current

$$J^\mu = \delta^{\mu+} \rho_a(x^-, x^T) t_a, \quad (3.1.4)$$

where we neglect the x^+ -dependency because we assume the valence quarks to be static in this direction. Next, we impose the covariant gauge condition

$$\partial_\mu A^\mu = 0 \quad (3.1.5)$$

and use the Ansatz

$$A^\mu = \delta^{\mu+} A_a^+(x^+, x^-, x^T) t_a \quad (3.1.6)$$

for the color fields. Inserting the Ansatz in the gauge condition yields

$$\partial_+ A^+ = 0. \quad (3.1.7)$$

Hence, the color fields are independent of x^+ . This justifies the choice of light cone coordinates. Further, lowering the index by using the derived form of the metric yields

$$A_+ = g_{+\nu} A^\nu = g_{+\nu} \delta^{\nu+} A_a^+ t_a = 0 \quad (3.1.8)$$

and therefore the color charge is conserved

$$\begin{aligned} D_\mu J^\mu &= \partial_\mu J^\mu + i A_\mu J^\mu \\ &= \partial_+ J^+ + i A_+ J^+ = 0. \end{aligned} \quad (3.1.9)$$

Since, $A^i = A_i = 0$ for $i = 1, 2$ we have $D_i = \partial_i$ and obtain

$$\partial_i \partial^i A^+(x^-, x^T) = \partial_i F^{i+} = J^+ = \rho_a(x^-, x^T). \quad (3.1.10)$$

This Poisson equation can be solved by partially Fourier transforming it with respect to the transverse coordinates. Equation (3.1.10) in transverse momentum space is given by

$$k_T^2 \tilde{A}^+(x^-, k_T) = \tilde{\rho}_a(x^-, k_T). \quad (3.1.11)$$

Transforming the charge density into this space can be used to obtain an explicit expression for the color fields. Applying an inverse Fourier transformation back to the normal space yields

$$A^+(x^-, x^T) = \int d^2 k_T \frac{1}{(2\pi)^2 k_T^2} \tilde{\rho}_a(x^-, k_T) \exp \left[i k_T^j x_T^j \right], \quad (3.1.12)$$

where the summation of the transverse directions $j = 1, 2$ is implied.

In prospect of initializing the color field of two nuclei which are moving in opposite directions it will prove useful to switch to another gauge given by $A^+ = 0$. This gauge condition is called light cone gauge. We keep discussing the color fields for only one nucleus in the continuum as they are equivalent for the second nucleus with swapped +- and -- components. For a more detailed discussion see [8]. In the lattice formulation of the MV-model we will take the second nucleus into account.

We employ the light cone gauge condition by finding a gauge transformation $V(x)$ such that

$$A_\mu(x) \rightarrow V(x^-, x^T) (A_\mu - i \partial_\mu) V^\dagger(x^-, x^T) \quad (3.1.13)$$

yields $A^+ = 0$. By rewriting this gauge condition for the transformed field we obtain

$$\partial_- V^\dagger(x^-, x^T) = -i A^+(\tilde{x}^-, x^T) V^\dagger(x^-, x^T), \quad (3.1.14)$$

where the gauge field in the integrand is denotes the gauge field before the transformation in covariant gauge. This represents an ordinary differential equation and thus is solved by

$$V^\dagger(x^-, x^T) = \mathcal{P} \exp \left(-i \int_{-\infty}^{x^-} d\tilde{x}^- A^+(\tilde{x}^-, x^T) \right). \quad (3.1.15)$$

We assume that the gauge transformation is independent of x^+ . Otherwise we would introduce a x^+ -dependence for the color fields by imposing the light cone gauge. Hence, we assume that $\partial_+ V^\dagger(x^-, x^T) = 0$. Taking into account that the transverse components of the gauge fields are vanishing in the covariant gauge yields the following expressions for the other components of the color fields

$$A^- = 0, \quad A_i = -iV(x^-, x^T) \partial_i V^\dagger(x^-, x^T) \quad (3.1.16)$$

in light cone gauge.

In the ultra relativistic limit of the system we can derive expressions for the gauge fields in covariant gauge. In this limit the charge density is given by

$$\rho_a(x^-, x^T) = \delta(x^-) \rho_a(x^T) \quad (3.1.17)$$

which can be plugged into (3.1.12) and since we only Fourier transformed the transverse coordinates this translates into

$$A^+(x^-, x^T) = \delta(x^-) A^+(x^T) \quad (3.1.18)$$

in covariant gauge. Since the longitudinal support of the charge density remains unchanged in the Fourier transformation we find an explicit expression for the gauge transformation (3.1.15) because the delta function in the integrand yields a Heaviside step-function. We obtain

$$A^+ = A^- = 0, \quad A^i = \Theta(x^-) V(x^T) \partial^i V^\dagger(x^T), \quad (3.1.19)$$

with the continuous Wilson lines

$$V(x^T) = \lim_{x^- \rightarrow \infty} V(x^-, x^T). \quad (3.1.20)$$

As pointed out in [8] the extent of the color field in transverse directions is merely a result of the gauge we used to formulate the relations above. In fact, the physical chromo-electric and chromo-magnetic fields are still concentrated at $x^- = 0$ at initial time. These physical fields are given by

$$\partial_i F^{i+} = J_{LC}^+(x^-, x^T), \quad (3.1.21)$$

where

$$J_{LC}^+(x^-, x^T) = \rho_{LC}(x^-, x^T), \quad \rho_{LC}(x^-, x^T) = \delta(x^-) V(x^T) \rho(x^T) V^\dagger(x^T) \quad (3.1.22)$$

are the color-charge density and current in light cone gauge.

We now introduce the color charge density, which can be defined by a Gaussian distribution. We can define the charge density by specifying the 1- and 2-point correlation functions, employing the following properties [29, 28]

$$\begin{aligned} \text{Color charge neutrality:} \quad & \langle \rho_a(x^T) \rangle = 0, \\ \text{Color charge fluctuation:} \quad & \langle \rho^a(x^T) \rho^b(y^T) \rangle = \mu^2 \delta^{ab} \delta(x^T - y^T). \end{aligned} \quad (3.1.23)$$

The parameter μ is known as the MV-parameter and is of phenomenological nature. We will discuss the magnitude and units of all given parameters in Section 5. A generalization of the above color density is given by

$$\begin{aligned} \langle \rho_a(x^-, x^T) \rangle &= 0, \\ \langle \rho^a(x^-, x^T) \rho^b(y^-, y^T) \rangle &= \mu^2 \delta^{ab} \delta(x^- - y^-) \delta(x^T - y^T), \end{aligned} \quad (3.1.24)$$

which yields the generalized MV-model [42]. Here the additional x^- -dependence is introduced because we do not assume the ultra relativistic limit for the color charge density (3.1.17). This leads to the additional longitudinal dependence. In Section 5 we will see that this adaption will have a big effect on the dynamics of the gauge system.

Lattice formulation of the McLerran-Venugopalan model

We will now formulate the initial conditions described by the MV-model on a hyper cubic lattice as introduced in Section 2.3. We will do this in the reverse chronology compared to the continuum. First we will define the charge density on the lattice, which can be written as [8, 6, 43]

$$\langle \rho_{x^T, n}^a \rangle = 0, \quad (3.1.25)$$

$$\langle \rho_{x^T, n}^a \rho_{x^T, m}^b \rangle = \frac{\mu^2}{N_\eta a^1 a^2} \delta^{ab} \delta_{mn} \delta(x^T - y^T). \quad (3.1.26)$$

Here we discretized the longitudinal direction by introducing N_η so-called color-sheets which can be described by parallel transverse planes. Note that we the 3 dimensional support of the charge density (3.1.25) is taken into account by introducing the color sheets which discretize the charge density in longitudinal direction. Since the gauge transformations which yield the color fields in light cone gauge are defined by light-like Wilson lines, we can describe this system effectively in 2+1 dimensions. Each site in the transverse lattice slice is visited by exactly one of those Wilson lines and therefore the gauge transformations are independent in the longitudinal direction. We neglect the longitudinal support of the color field can therefore describe the system in 2+1 dimensions. Figure 3.1 shows a visualization of the color-sheet approximation. The next step is to discretize

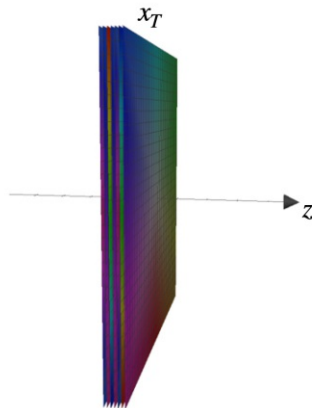


Figure 3.1: Illustration of the color-sheet approximation on a lattice. The label z represents the longitudinal direction whereas x_T denotes the transverse directions.

the relation of the color fields with the color-charge density given by the Poisson equation (3.1.10).

This is achieved in a straight forward manner by approximation the transverse Laplacian by finite differences which yields [44, 8]

$$\partial_i \partial^i A^+(x^-, x^T) = \sum_{i,a} \frac{1}{(a^i)^2} \left(A_{x+\hat{i},n}^{a,+} - A_{x-\hat{i},n}^{a,+} + 2A_{x,n}^{a,+} \right) = \rho_{x,n}^a(x^-, x^T). \quad (3.1.27)$$

Solving this equation can be done with the same strategy as in the continuum formulation. We first Fourier transform the equation to momentum space and after initializing it with the transformed charge density transforming it back to normal space. This is done using the fast Fourier transformation algorithm. We obtain

$$k_T^2 \tilde{A}_{k,n}^{a,+} = \tilde{\rho}_{k,n}^a \quad (3.1.28)$$

with

$$k_T^2 = \sum_{i=1,2} \left(\frac{2}{a^i} \right)^2 \sin^2 \left(\frac{k_i a^i}{2} \right). \quad (3.1.29)$$

In momentum space the discretization of the transverse plane is defined by the momentum lattice spacing $\Delta k = 2\pi/(N_i a)$, where N_i is the number of lattice points in direction x^i , for $i = 1, 2$. For the remainder of this work we will assume $a = a_1 = a_2$ and $N = N_1 = N_2$ in order to avoid any distinction of cases depending on the lattice spacings. An important aspect of these initial conditions is that they are very sensitive to the granularity of the discretization. This means that the system will suffer from infrared divergences by choosing small (transverse) lattice volume V_T because the smallest non-zero momentum is given by

$$k_{min} = \frac{2\pi}{Na} = \frac{2\pi}{\sqrt{V_T}}. \quad (3.1.30)$$

We also have to deal with ultra violet divergences because the largest momentum is given by

$$k_{max} = \frac{2}{a}, \quad (3.1.31)$$

which poses a problem for sufficiently small lattice spacings. These divergences need to be taken into account since the lattice volume is dictated by the physical volume of the gauge system and the lattice spacing needs to be assumed sufficiently small in order to keep numerical errors small. We emphasize that it is not possible to get rid of both divergences by rescaling the lattice distances since both divergences are proportional to the reciprocal of a .

In order to deal with both types of divergences we introduce the screening mass m and the ultra violet regulator Λ_{UV} . For regularizing the system the solution for color fields (3.1.28) in momentum space is very useful because we introduce the regularized color fields

$$\tilde{A}_{k,n}^{a,+} = \frac{1}{k_T^2 + m^2} \Theta(\Lambda_{UV}^2 - k_T^2) \tilde{\rho}_{k,n}^a \quad (3.1.32)$$

in momentum space [44, 8]. Additionally, we introduced set the zero-momentum modes of the color fields to 0 in order to ensure color neutrality.

In order to obtain the color-fields for the nucleus moving in the x^+ -direction we can repeat all of the steps above and swap the $+$ - and $-$ -components.

As we have discussed in Section 2.3 we can identify the parallel transporter with the link variables $U_{x,\mu}$. We can enhance this identification by introducing Wilson lines, which are products of link variables connecting consecutive lattice sites. These objects can therefore be seen as the analogous object to the parallel transporter along a path C_{xy} , where x and y are not necessarily neighboring

lattice sites. Therefore the discretization of the integral in (3.1.20) can be rewritten in terms of light-like Wilson lines [44, 8]

$$V_{A,x} = \prod_{n=1}^{N_\eta} \exp [iA_{x,n}^{a,+} t^a], \quad V_{B,x} = \prod_{n=1}^{N_\eta} \exp [iA_{x,n}^{a,-} t^a]. \quad (3.1.33)$$

The letters A, B denote the x^- -moving and x^+ -moving nucleus respectively. Note, that the path ordering in (3.1.15) represents a very important aspect in this step, because the calculation of the light-like Wilson lines is neither linear, nor is it commutative. However, in practice we sample the color density from a Gaussian distribution where the ordering which component we sample first is not relevant due to the stochastic nature of the process. At this point it makes sense to justify the construction of this Wilson loop because this step reduces the $3 + 1$ dimensional gauge system to an effectively $2 + 1$ dimensional system. The longitudinal direction of the lattice which was occupied by the color-sheets is collapsed onto the transverse plane. As given in (3.1.20) the light-like Wilson lines would span from negative light-like infinity to positive light-like infinity in x^- - and x^+ -direction respectively.

In practice we cannot realize an infinitely long lattice because of finite computational resources. Nevertheless the description of the Wilson lines in (3.1.33) is correct because we assumed that the charge density vanishes outside of the color-sheets and therefore does not contribute to the Wilson lines. Multiple color-sheets are used in order not to assume the full boost invariant form of the system where the charge distribution is concentrated in a transverse plan. Multiple color-sheets impose a non-vanishing longitudinal support of the charge density.

Next, we introduce the transverse link variables. Because in the covariant gauge formulation the transverse color-fields A^i , $i = 1, 2$ vanish the link variables are given by identity matrices. We obtain the expressions for the transverse link fields in light-cone gauge by transforming identity matrices

$$U_{x,i}^A = V_{A,x} V_{A,x+\hat{i}}^\dagger, \quad U_{x,i}^B = V_{B,x} V_{B,x+\hat{i}}^\dagger. \quad (3.1.34)$$

In [8] the gauge fields at initial time τ_0 in the MV-model for two colliding nuclei are discussed in more detail.

We emphasize that U^A and U^B are the link fields which replace the transverse continuous color fields of the nuclei A and B respectively in the lattice formulation. These color fields are given in light-cone gauge. The Minkowski diagram depicted in Figure 3.2 shows that the collision between the nuclei cannot effect the regions II-IV since these regions are not causally connected to the event. However, region I (the future light-cone) is affected by the collision and a non-trivial color field, which is referred to as Glasma, is created in this process [43]. For the color currents which describe each of the nuclei we assume that they do not lose any momentum and that they stay on their light-like trajectories despite the collision. From these properties we can follow that the color charges are conserved for both currents [8]. This causal separation enables us to derive the color field in region I by the separate, independent solutions for the color fields of the colliding nuclei. In order to take into account that the presence of the fields can lead to color rotations of the charge densities for the nuclei we employ the Fock-Schwinger gauge condition

$$x^+ A^- + x^- A^+ = 0, \quad x^+, x^- > 0, \quad (3.1.35)$$

in light-cone coordinates for region I. In the other regions II-IV we fix $A^- = A^+ = 0$ which can be analytically connected to the gauge condition in the future light-cone. The boost invariance of the color current is inherited from the color currents to all other observables of this system as it is the only quantity that the Yang-Mills equation depends on. We therefore transform the Glasma color

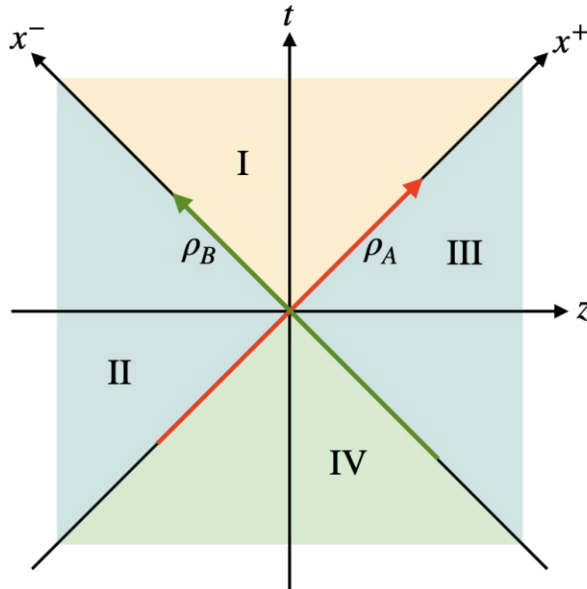


Figure 3.2: Minkowski diagram which illustrates the separation of the space-time into four different regions by the color currents. ρ_A and ρ_B denote the color current for the colliding nuclei on their light-like trajectories in opposite directions. Region I is the only causally connected region for the collision at $\tau \rightarrow 0$. The color field created in this region due to the collision of the nuclei is called Glasma. II and III are the regions of the color fields for the nuclei B and A respectively.

field to (τ, η) -coordinates (2.1.2) with which the boost invariance translates into an independence of the η -coordinate. In these coordinates the Fock-Schwinger gauge yields the temporal gauge

$$A_\tau = 0. \quad (3.1.36)$$

In the continuum we can express the color field of the Glasma in terms of the solutions for each of the nuclei by

$$A_i(\tau_0, x_T) = -(\alpha_A^i(x_T) + \alpha_B^i(x_T)), \quad i = 1, 2 \quad (3.1.37)$$

$$A_\eta(\tau_0, x_T) = 0, \quad (3.1.38)$$

in the (τ, η) -coordinates at initial time $\tau_0 \rightarrow 0$ [8]. We write α_A and α_B for the color fields of each nuclei in the continuum to distinguish them from the Glasma color field $A_\mu(\tau, x_T)$.

In [45] a lattice formulation for the transverse link fields of the total color fields for both nuclei is derived, they are given implicitly by

$$\left[(U_{x,i}^A + U_{x,i}^B) (\mathbb{1} + U_{x,i}(\tau_0))^\dagger \right]_{ah} = 0, \quad (3.1.39)$$

at initial time τ_0 . The subscript in above expression denotes the anti-hermitian and traceless part of a matrix in the brackets. For an arbitrary element M of $SU(N_c)$ this is given by

$$[M]_{ah} = \frac{1}{2i} \left((M - M^\dagger) - \frac{1}{N_c} \text{tr} (M - M^\dagger) \right). \quad (3.1.40)$$

In Appendix B we discuss how to obtain an explicit solution for $SU(2)$ theories. For $SU(3)$ the equation has to be solved numerically. The longitudinal components of the link variables are given by identity matrices.

In order to avoid boundary effects due to the finite lattice volume we impose periodic boundary conditions. We can realize these for the transverse link field $U_{x,i}$ by requiring

$$U_{x_0,i} = U_{x_1+\hat{j},i} \quad \text{for } i, j = 1, 2, \quad (3.1.41)$$

with

$$x_0^j = 0, \quad x_1^j = Na. \quad (3.1.42)$$

The chromo-electric and chromo-magnetic fields can be identified using the interpretation of the field strength tensor components in analogy to classical electrodynamics. Note that since we are using the temporal gauge and assume that the color fields are boost invariant in rapidity direction we have

$$\begin{aligned} D_\tau &= \partial_\tau, \\ \partial_\eta A^\mu &= 0. \end{aligned} \quad (3.1.43)$$

The chromo-electric fields are therefore given by

$$E_i = g_{\tau\mu} g_{i\nu} F^{\mu\nu} = \partial_\tau A_i \quad \text{for } i = +, -, \quad (3.1.44)$$

$$E_\eta = g_{\tau\mu} g_{\eta\nu} F^{\mu\nu} = \frac{1}{\tau} \partial_\tau A_\eta \quad (3.1.45)$$

and the chromo-magnetic field can be written as

$$B_i = -\frac{1}{2} g_{il} g_{jm} g_{kn} \epsilon^{ljk} F^{mn} = -\epsilon_{ij} D_j A_\eta, \quad (3.1.46)$$

$$B_\eta = -\frac{1}{2} g_{\eta l} g_{m} g_{kn} \epsilon^{ljk} F^{mn} = -F_{12}. \quad (3.1.47)$$

Additionally, we can relate the components of the chromo-electric fields to the canonical momenta

$$E_i = \frac{1}{\tau} P^i, \quad E_\eta = P^\eta. \quad (3.1.48)$$

It therefore suffices to initialize the chromo-electric field in our simulations next to the link fields in order to fully describe the gauge system at an initial time $\tau_0 > 0$. We can write the longitudinal chromo-electric field in the lattice formulation as [8]

$$E_{x,\eta}(\tau_0) = \frac{1}{2a^2} \sum_{i=1,2} \left[(U_{x,i} - \mathbb{1}) (U_{x,i}^{B\dagger} - U_{x,i}^{A\dagger}) + (U_{x-\hat{i},i}^\dagger - \mathbb{1}) (U_{x-\hat{i},i}^{B\dagger} - U_{x-\hat{i},i}^{A\dagger}) \right]_{ah}. \quad (3.1.49)$$

The transverse chromo-electric fields vanish at initial time.

3.2 Gaussian Initial Conditions

We now introduce a second type of initial conditions, which are known as Gaussian initial conditions [35], [33]. Before we come to a detailed discussion of these conditions we introduce an expression for the distribution function in terms of so-called mode vectors, which we denote by $\xi_{j,p^i}^{(\lambda)}$. We require that these vectors satisfy

$$\left(\partial_0 \xi_{j,p^i}^{(\lambda)}(x^0) \right)^* = \partial_0 \xi_{j,p^i}^{(\lambda)*}(x^0) \quad (3.2.1)$$

and the normalization condition

$$g^{jk}(x^0) \left(\xi_{j,p^i}^{(\lambda)}(x^0) \overset{\leftrightarrow}{\partial}_0 \xi_{k,p^i}^{(\lambda')}(x^0) \right) = \delta_{\lambda,\lambda'} \frac{i}{\sqrt{-g(x^0)}} \quad (3.2.2)$$

as well as free classical equations of motion. The superscript $\lambda = 1, 2$ denote the polarization directions. We assume two polarizations because our goal is to employ Glasma-like initial conditions which yield that number of polarizations [31]. Note, that for the expanding case we identify the longitudinal component of the momentum by the rapidity wave number divided by the proper time $p^3 = \frac{\nu}{\tau}$. The double-sided arrow over the derivative is a short hand notation for

$$A \overset{\leftrightarrow}{\partial}_\mu B = A \partial_\mu B - (\partial_\mu A) B \quad (3.2.3)$$

for arbitrary fields A and B. For the explicit form of the mode vectors see [32], [34].

We introduce operators $\alpha_{a,p^i}^{(\lambda)}$ as classical analogous objects to annihilation and creation operators given by

$$\alpha_{a,p^i}^{(\lambda)}(x^0) = i \sqrt{-g(x^0)} \int d^3x \exp(-ix^i p^i) g^{jk}(x^0) \left(\xi_{j,p^i}^{(\lambda)*}(x^0) \overset{\leftrightarrow}{\partial}_0 A_k^a(x^\mu) \right), \quad (3.2.4)$$

where V denotes the volume of the observed system. We require that these operators satisfy

$$\left\langle \alpha_{a,p^i}^{(\lambda)} \alpha_{a,p^{i'}}^{(\lambda')*} \right\rangle = \left(f(t_0, p^i) + \frac{1}{2} \right) (2\pi)^3 \delta_{ab} \delta_{\lambda\lambda'} \delta^{(3)}(p^i - p^{i'}), \quad (3.2.5)$$

$$\left\langle \alpha_{a,p^i}^{(\lambda)} \alpha_{b,p^{i'}}^{(\lambda')*} \right\rangle = \left\langle \alpha_{a,p^i}^{(\lambda)*} \alpha_{b,p^{i'}}^{(\lambda')*} \right\rangle = 0. \quad (3.2.6)$$

This enables us to define the distribution function in terms of mode vectors

$$f_{gluon}(x^0, \tilde{p}^i) = \frac{1}{(N_c^2 - 1)} \sum_{a=1}^{N_c^2 - 1} \left\langle |\alpha_{a,\tilde{p}^i}^{(1)}(x^0)|^2 \right\rangle, \quad (3.2.7)$$

$$f_{scalar}(x^0, \tilde{p}^i) = \frac{1}{(N_c^2 - 1)} \sum_{a=1}^{N_c^2 - 1} \left\langle |\alpha_{a,\tilde{p}^i}^{(2)}(x^0)|^2 \right\rangle, \quad (3.2.8)$$

We dropped the $\frac{1}{2}$ factor since we require high occupancy numbers (2.4.43). Furthermore, it can be shown that this definition of the distribution is equivalent to (2.4.42) [33]. Hence, the interpretation in terms of occupation numbers is thereby justified.

We can see that the operators $\alpha_{a,p^i}^{(\lambda)}$ are dependent on the gauge fields A . Therefore the distribution function is not a gauge independent quantity. As in the discussion about the MV-model it proves useful to chose the temporal gauge $A_\tau = 0$. However, this gauge condition leaves residual gauge freedoms which we fix by choosing the Coulomb gauge

$$-g^{ij}(x^0) \partial_i A_j^a(x^\mu) = 0 \quad (3.2.9)$$

at a fixed time in order to make the distribution function comparable.

The temporal gauge enables us to neglect the A_a^0 component of the gauge field completely in our simulation. Hence, implicitly this gauge condition is fulfilled at all times of the simulation. The downside of this approach is that the Coulomb gauge gets destroyed during the simulation and has to be reestablished each time when calculating gauge dependent quantities such as the distribution function. We use the Fourier acceleration method presented in [46] to restore this gauge condition.

In order to describe the system completely we have to initialize the gauge field and the chromo-electric field at initial time t_0 . These are given by their mode expansions

$$A_j^a(\tau_0, x^i) = \int \frac{d^3p}{(2\pi)^3} \left(\alpha_{a,p^i}^{(\lambda)} \xi_{j,p^i}^{(\lambda)}(\tau_0) e^{ip^i x^i} + \alpha_{a,p^i}^{(\lambda)*} \xi_{j,p^i}^{(\lambda)*}(\tau_0) e^{-ip^i x^i} \right), \quad (3.2.10)$$

$$E_a^j(\tau_0, x^i) = \sqrt{-g(\tau_0)} g^{jk}(t_0) \int \frac{d^3p}{(2\pi)^3} \left(\alpha_{a,p^i}^{(\lambda)} \partial_0 \xi_{j,p^i}^{(\lambda)}(\tau_0) e^{ip^i x^i} + \alpha_{a,p^i}^{(\lambda)*} \partial_0 \xi_{j,p^i}^{(\lambda)*}(\tau_0) e^{-ip^i x^i} \right). \quad (3.2.11)$$

The chromo-electric and color field can be discretized by approximating the above integral with a finite sum and by defining the fields and mode vectors on the lattice sites. The link fields $U_{x,j}$ on the lattice are given by

$$U_{x,\mu} = \exp [ia_\mu A_{x,\mu}]. \quad (3.2.12)$$

In the conducted simulations we assume that the distribution function is of the form

$$f(x^0 = \tau_0, p^i) = n_0 \frac{Q}{g^2} \left(\frac{p}{Q} \right)^{-\kappa} e^{-\frac{p^2}{2p_0^2}}, \quad (3.2.13)$$

which fulfills the high occupancy property for small couplings $g \ll 1$ and therefore we can use the classical approximation discussed in Section 2.4. We refer to n_0 and Q as the initial amplitude and the conserved momentum scale respectively.

The energy density of the system is given by

$$\varepsilon = 2(N_c^2 - 1) \int \frac{d^2 p}{(2\pi)^2} p (f_{gluon}(x^0, p^i) + f_{scalar}(x^0, p^i)). \quad (3.2.14)$$

The factor $(N_c^2 - 1)$ is introduced because we assume that all color components are governed by the distribution functions f_{gluon} and f_{scalar} . Note that unlike the non-expanding case the energy density is expected to decrease over time, due to the expansion in longitudinal direction. Using polar coordinates for the evaluation of this integral yields the following expression for the energy density

$$\varepsilon = \frac{2(N_c^2 - 1)Q^{\kappa+1}n_0}{2\pi g^2} 2^{-(\kappa-1)/2} \Gamma\left(\frac{3-\kappa}{2}\right) p_0^{3-\kappa}. \quad (3.2.15)$$

We assumed $\kappa < 3$ to ensure that the integral is finite. We can now use this equation to define the conserved momentum as

$$Q^4 = \frac{C(\kappa)g^2\varepsilon}{2(N_c^2 - 1)} = \frac{2^{-(\kappa-1)/2}}{2\pi} \Gamma\left(\frac{3-\kappa}{2}\right) C(\kappa)n_0Q^{\kappa+1}p_0^{3-\kappa} \quad (3.2.16)$$

where $C(\kappa)$ denotes a constant which relates p_0 and Q . As suggested in [31] we choose this constant such that for $n_0 = 0.1$ we have $Q = p_0$. For $\kappa = 0$ and $N_c = 2$ this gives $C(0) = 20\sqrt{2\pi}$.

Finally, we have to take into account that for that the equations of motion derived in Section 3.3 include the Gauss constraint. Therefore the fields defined by the Gaussian initial conditions have to satisfy this condition. In the lattice formulation the Gauss constrain reads

$$\sum_{j>0} \frac{E_x^j - U_{x-\hat{j},j}^\dagger E_{x-\hat{j}}^j U_{x-\hat{j},j}}{a_j} = 0. \quad (3.2.17)$$

We have approximated the covariant derivative with a backward derivative defined in terms of the links as discussed in Section 2.3. Since the equations of motion preserve this constraint we only need to restore it at the beginning of the simulation. We use an adapted version of the Gauss restoration algorithm presented in [47] in order to restore the Gauss constraint. Note that the Gauss constraint is automatically satisfied for the Glasma initial conditions since the transverse chromo-electric field components vanish at initial time t_0 and the fields are assumed to be boost invariant.

3.3 Equations of motion

In this section we introduce the equations of motion for the continuum theory and discretize them. Starting from the gauge action

$$S_G[A] = -\frac{1}{2} \int d^4x \sqrt{-g(x^0)} F_a^{\mu\nu}(x) F_{\mu\nu}^a(x) \quad (3.3.1)$$

we impose the temporal gauge $A^0 = 0$ which yields an expression for the effective action

$$S_{G,eff}[A] = -\frac{1}{2} \int d^4x \sqrt{-g(x^0)} \left(g^{jk}(x^0) \partial_0 A_j^a \partial_0 A_j^a + \frac{1}{2} g^{jk}(x^0) g^{mn}(x^0) F_{jm}^a F_{kn}^a \right). \quad (3.3.2)$$

Identifying the chromo-electric field with the conjugate momentum fields

$$E_a^j(x^\mu) = \frac{\delta S_{G,eff}}{\delta(\partial_0 A_j^a(x^\mu))} = \sqrt{-g(x^0)} A_0^a(x^\mu) \quad (3.3.3)$$

the effective Hamiltonian can be written as

$$H_{G,eff}[A, E] = -\frac{1}{2} \int d^3x \left(\frac{1}{\sqrt{-g(x^0)}} g_{jk}(x^0) E_a^j E_a^k - \frac{1}{2} g^{jk}(x^0) g^{mn}(x^0) F_{jm}^a F_{kn}^a \right). \quad (3.3.4)$$

We can now state the equations of motion as functional derivatives of the effective Hamiltonian

$$\begin{aligned} \partial_0 E_a^j(x) &= -\frac{\delta H_{G,eff}}{\delta A_a^j(x)} = \sqrt{-g(x^0)} D_k^{ab}(x) F^{kj}(x), \\ \partial_0 A_j^a(x) &= \frac{\delta H_{G,eff}}{\delta E_a^j(x)} = -\frac{1}{\sqrt{-g(x^0)}} g_{jk}(x^0) E_a^k(x). \end{aligned} \quad (3.3.5)$$

These equations are equivalent to the classical equation of motion given by the functional derivatives of the gauge action with respect to spatial components of the color fields

$$\frac{\delta S_G}{\delta A_j^a(x^\mu)} = 0. \quad (3.3.6)$$

Imposing the temporal gauge and deriving the effective action we implicitly neglected the functional derivative with respect to the temporal gauge field component. In order to be consistent with the full classical equations of motions we additionally require

$$\frac{\delta S_G}{\delta A_0^a(x^\mu)} = 0 \quad \Rightarrow \quad D_j E^j(x) = 0, \quad (3.3.7)$$

which is also known as the Gauss constraint. This property is preserved by the equations (3.3.5). Hence, we only need to ensure that this constraint is satisfied at initial time of our simulation.

Equations of motion on a lattice

We now discretize the Hamiltonian (3.3.4) with the formalism developed in Section 2.3 and approximate the integral with the finite sum over all lattice sites. The lattice regularized Hamiltonian is given by

$$\begin{aligned} H_{G,latt}[U, E] &= \sum_{x^i} a^3 \left[-\frac{1}{2\sqrt{-g(x^0)}} g_{jk}(x^0) E_{x,c}^j E_{x,c}^k + \right. \\ &\quad \left. \frac{2N_c}{g^2} \sum_{j=1}^3 \sum_{k>j} C_{jk} \left(1 - \frac{1}{2N_c} \text{tr} U_{x,jk} - \frac{1}{2N_c} \text{tr} U_{x,jk}^\dagger \right) \right], \end{aligned} \quad (3.3.8)$$

where the summation over the color components c is implied. We assume that all spatial lattice distances are equal $a_i = a$, $i = 1, 2, 3$ and distinguish between the Minkowski and Bjorken (longitudinally) expanding system with the symmetric coefficients C_{jk} given by

$$C_{jk} = \frac{1}{a^4} \sqrt{-g(x^0)} g^{jj}(x^0) g^{kk}(x^0). \quad (3.3.9)$$

We can show that the above expression matches the effective Hamiltonian (3.3.4) in the continuum limit $a \rightarrow 0$. This can be shown using the expansion of the plaquettes and expressing the field strength tensor in terms of the plaquettes as given in (2.3.20).

In order to find explicit expressions for the equations of motion we vary the Hamiltonian in analogy to the continuous case

$$\partial_0 E_{x,a}^k = \frac{\delta H_{G,latt}}{\delta A_{x,k}^a}. \quad (3.3.10)$$

Since the plaquettes in the equation (3.3.8) are composed of four link fields we first calculate the variation of the link fields with respect to the color fields at equal time $x^0 = y^0$

$$\begin{aligned} \frac{\delta U_{x,j}}{\delta A_{y,k}^c} &= \delta_{jk} \delta^{(3)}(x-y) \frac{1}{a^3} \frac{\partial}{\partial \alpha} [e^{iga\alpha t^c} U_{x,j}]_{\alpha=0} = \frac{ig}{a^2} \delta_{jk} \delta^{(3)}(x-y) t^c U_{y,k}, \\ \frac{\delta U_{x,j}^\dagger}{\delta A_{y,k}^c} &= \delta_{jk} \delta^{(3)}(x-y) \frac{1}{a^3} \frac{\partial}{\partial \alpha} [U_{x,j}^\dagger e^{-iga\alpha t^c}]_{\alpha=0} = -\frac{ig}{a^2} \delta_{jk} \delta^{(3)}(x-y) t^c U_{y,-k}. \end{aligned} \quad (3.3.11)$$

This yields the variation of the trace of a plaquette

$$\frac{\delta \text{tr} U_{x,jk}}{\delta A_{y,l}^c} = \frac{g}{a^2} \delta^{(3)}(x-y) \delta \sum_{k \neq 0, l} \text{Re} [it^c (U_{y,lk} + U_{y,l(-k)})]. \quad (3.3.12)$$

Inserting this result into (3.3.10) we obtain

$$\partial_0 E_{x,c}^j = -\frac{a}{g} \sum_{k \neq 0, j} C_{jk} \text{Re} [-2it^c (U_{x,jk} + U_{x,j(-k)})]. \quad (3.3.13)$$

We find the equations of motion for the link field by calculating

$$\partial_0 U_{x,j} = \frac{\delta H_{G,latt}}{\delta E_{x,a}^j}, \quad (3.3.14)$$

and obtain

$$\partial_0 U_{x,j} = a^3 \sum_y^i \partial A_{y,k}^a \frac{\delta U_{x,j}}{\delta A_{y,k}^a} = -iga \frac{g_{jj}(x^0)}{\sqrt{-g(x^0)}} \sum_{c=1}^{N_c^2-1} E_{x,c}^j t^c U_{x,j}. \quad (3.3.15)$$

We have now derived the classical equations of motion in the lattice formulation (3.3.13) and (3.3.15). They define the way how the color and the chromo-electric fields evolve over time and are therefore a crucial part of our simulations.

Specifically at starting time $x^0 = t_0$ we initialize the fields as discussed in Section 3.1 and 3.2. We offset the chromo-electric field by a half time step $a_0/2$ in forward time direction. During the simulation the link and the chromo-electric fields are updated in an alternatingly. This process is known as the leapfrog algorithm and is illustrated in Figure 3.3. For each time step the chromo-electric

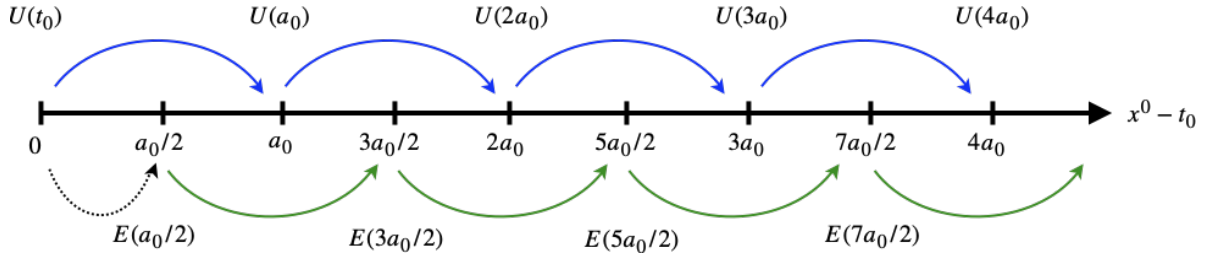


Figure 3.3: Illustration of the leapfrog algorithm for the link fields U and chromo-electric fields E .

and the link fields are updated using the forward Euler scheme. This is done by approximating the temporal derivative with a finite difference

$$\partial_0 E_{x,a}^j \approx \frac{E_{x+\hat{0},a}^j - E_{x,a}^j}{a_0}. \quad (3.3.16)$$

Inserting the equation of motion (3.3.13) and rewriting the approximation above yields

$$\begin{aligned} E_{x+\hat{0},a}^j &\approx a_0 \partial_0 E_{x,a}^j + E_{x,a}^j \\ &= -\frac{aa_0}{g} \sum_{k \neq 0,j} C_{jk} \text{Re} [-2it^c (U_{x,jk} + U_{x,j(-k)})] + E_{x,a}^j. \end{aligned} \quad (3.3.17)$$

Similarly we can deduce an update step for the link field, where the forward Euler scheme gives

$$\partial_0 U_{x,j} \approx \frac{U_{x+\hat{0},j} - U_{x,j}}{a_0}, \quad (3.3.18)$$

which yields

$$\begin{aligned} U_{x+\hat{0},j} &\approx a_0 \partial_0 U_{x,j} + U_{x,j} \\ &= -igaa_0 \frac{g_{jj}(x^0)}{\sqrt{-g(x^0)}} \sum_{c=1}^{N_c^2-1} E_{x,c}^j t^c U_{x,j} \\ &= \left(\mathbb{1} - igaa_0 \frac{g_{jj}(x^0)}{\sqrt{-g(x^0)}} E_{x,c}^j t^c \right) U_{x,j}. \end{aligned} \quad (3.3.19)$$

The summation of the color components is implied. For sufficiently small time steps a_0 we can rewrite the update rule for the link fields as

$$U_{x+\hat{0},j} \approx \exp \left[-igaa_0 \frac{g_{jj}(x^0)}{\sqrt{-g(x^0)}} E_{x,c}^j t^c \right] U_{x,j}. \quad (3.3.20)$$

Note that in order to ensure the stability of the described procedure we have to use sufficiently small time steps a_0 such that the update rules (3.3.17) and (3.3.20) are justified. In particular, we require

$$a_0 \ll a \quad (3.3.21)$$

to ensure the approximation in (3.3.20) is justified. In practice we initialize the time step size by specifying the ratio to the lattice distance. We also want to emphasize that the Bjorken metric is singular for the initial time $t_0 = 0$ and we therefore require $t_0 > 0$ for the expanding case.

Lattice simulations in a nutshell

We now want to recapitulate the steps taken in simulations on a two dimensional lattice:

1. Initialize color fields $A_{x,j}^a$ according to the Glasma or Gaussian initial conditions given in equation (3.1.32) or (3.2.10) respectively at initial time t_0 .
2. Calculate link and chromo-electric fields given by (3.1.39) and (3.1.49) for Glasma initial conditions and (3.2.12) and (3.2.11) for Gaussian initial conditions.
3. Employ periodic boundary conditions for both fields given by

$$U_{x,i} = U_{y+\hat{j},i}, \quad E_{x,a}^i = E_{y+\hat{j},i}, \quad i = 1, 2 \quad (3.3.22)$$

where we assume $x^j = 0$, $y^j = Na$ for fixed $j = 1, 2$.

4. For Gaussian initial conditions we need to ensure that the Gauss constraint (3.2.17) is fulfilled. This is done via a modified version of the Gauss restoration algorithm presented in [47].
5. Introduce an offset in the time of the chromo-electric field

$$E_{x,a}^j \mapsto E_{x+\hat{0}/2,a}^j \quad (3.3.23)$$

by applying the update rule (3.3.17) for a half time step $a_0/2$.

6. Run update rules (3.3.20) and (3.3.17) for the link and the chromo-electric fields alternatingly

$$\begin{aligned} U_{x,j} &\mapsto E_{x+\hat{0}/2,j} \\ E_{x+\hat{0}/2,a}^j &\mapsto E_{x+\hat{0}/2+\hat{0},a}^j \end{aligned} \quad (3.3.24)$$

until the end of the simulation.

Note that in practice we will re-scale the gauge fields and the chromo-electric fields according to

$$A_{x,j}^a \mapsto \frac{1}{g} A_{x,j}^a \quad (3.3.25)$$

$$E_{x,a}^j \mapsto \frac{1}{g} E_{x,a}^j \quad (3.3.26)$$

in order to get rid of the coupling constants in the update rules (3.3.20) and (3.3.17). Furthermore, we rescale all dimensional quantities in the simulation with a scaling constant denoted Q_{latt} . For more details about this rescaling to lattice units see Appendix C.

Chapter 4

Energy densities for expanding space-times

In order to ensure that the initial conditions described in Section 3.1 and 3.2 as well as the simulation procedure discussed in Section 3.3 are implemented correctly we will present the most important results for the evolution of the energy density in this chapter and compare them with the literature. In addition, we will compare the MV-model with the Gaussian initial conditions by choosing the parameters of the distribution function (3.2.13) such that they approximate the occupation numbers obtained for the Glasma simulations at $\tau = 0.1$ fm/c. This observation time is chosen because at initial time the MV-model imposes no longitudinal chromo-electric field component [6]. Furthermore this set of initial conditions are known to suffer from UV-divergences [48], [49] and therefore are hardly comparable to Gaussian initial condition for the same initial time.

4.1 Energy densities for Glasma initial conditions

In this subsection we present the results achieved by our numerical framework using initial conditions imposed by the MV-model as presented in Section 3.1. We especially focus on a time scale where the boost invariance may still hold and hence the description of the gauge system motivated by the MV-model is valid.

MV-model parameters

Following common choices in the literature, we derive and motivate our choice of MV-model parameters which are used to define the initial conditions. As this model was motivated by a central ultra-relativistic collision of two nuclei we choose the lattice volume according to the size of a gold nucleus projected onto a plane. We assume an atomic number $A = 197$ and estimate the radius of the nucleus by $R_A = 1.2A^{1/3}$ fm. This yields the width of the two dimensional lattice

$$L \approx \sqrt{R_A^2 \pi} \approx 12.4 \text{ fm} \quad (4.1.1)$$

in transverse direction. We further choose the granularity of the lattice by the number of lattice points in each direction. This yields the transverse lattice spacing

$$a = L/N. \quad (4.1.2)$$

Throughout this work we will use different lattice spacings since the number of lattice sites influences the computing time of the simulations drastically. It has been shown that the MV-model is dependent on the lattice spacing but the qualitative behavior for sufficiently small lattice distances is not influenced [44]. We therefore choose the number of lattice sites such that we minimize

unphysical effects due to the discretization while keeping the computation time low. We further choose a lattice scaling parameter given by

$$Q_{latt} = 0.197326 \frac{N}{L} \text{ GeV} \quad (4.1.3)$$

to rescale the lattice spacing to $a_{latt} = 1Q_{latt}$.

The MV-parameter μ is estimated by

$$\mu^2 \approx 1.1A^{1/3} \text{ fm}^{-2} \quad (4.1.4)$$

as it yields the color-charge squared per unit area in a nucleus with an atomic number A [28]. This approximation yields $\mu \approx 0.5 \text{ GeV}$ for the gold nucleus and we adopt this parameter as it is often used in the literature. Also, it can be shown that this parameter relates to the saturation momentum $Q_s \approx Q = g^2\mu$, which was shown in [50]. Additionally, it is estimated that an Au-Au-collision at the Relativistic Heavy Ion Collider (RHIC) results in a saturation momentum of $Q_s = 2 \text{ GeV}$ [51]. We therefore assume that the coupling constant is given by $g = 2$.

In Section 3.1 we introduced the screening mass m and the parameter Λ_{UV} in order to regularize infra-red and ultra-violet divergences respectively. We emphasize that the finite lattice already implicitly regularizes the system because the finite lattice spacing translates into minimal and maximal momentum modes (the zero-momentum node is neglected in the MV-model). However we introduce both parameters since the Glasma initial conditions are known to suffer from ultra-violet divergences [43] and the screening mass relates to the scale Λ_{QCD} in the continuum theory. Throughout this work we adopt the value $\Lambda_{UV} = 20 \text{ GeV}$. Note, that the most dominant modes are the non-vanishing yet small momentum modes. Hence, the UV regularization does not disturb our results but reduces artifacts from the UV-divergences at early times $\tau < 0.1 \text{ fm}/c$.

As mentioned above we expect that the screening mass is assumed to be related to the QCD scale Λ_{QCD} . In the classical treatment of the Glasma we cannot find an exact relation since we would need the full description including quantum effects. We motivate our choice of $m = 0.2 \text{ GeV} \approx 1 \text{ fm}^{-1}$ by pointing out that this is approximately the inverse length scale of a proton which is assumed to be color neutral. A detailed discussion about the dependency of the screening mass can be found in [44].

Energy densities of gauge systems with Glasma initial conditions

We now discuss the results we obtained by using our numerical framework which implements the leapfrog algorithm following the equations of motion as derived in Section 3.3. Throughout this presentation we will fix the screening mass $m = 0.2 \text{ GeV}$ and UV-cutoff $\Lambda_{UV} = 20 \text{ GeV}$. We show simulation results for two different color-sheet approximations in order to ensure that the qualitative dynamical behavior is independent of the number of color-sheets and observe differences in the quantitative dynamical behavior for both discretizations. A detailed discussion about the behavior of the energy densities for the MV-model with respect to a change of lattice spacings and the regulator parameters can be found in [44]. We can reproduce the described dynamics to good accuracy and will show the most essential results in this section by distinguishing between the single color-sheet approximation and the generalized MV-model with $N_\eta = 30$.

Figure 4.1 shows the energy density for gauge systems simulated using the original MV-model and with the generalized version with 30 color-sheets for $0.0001 - 0.5 \text{ fm}/c$. At $\tau = Q^{-1} = 0.1 \text{ fm}/c$ it is observed that the energy densities behave as $1/\tau$. This behavior is expected since the system is expanding in longitudinal direction at this rate. We also observe that for earlier times the behavior of the energy density changes dramatically. This change can be explained with the fact that in the ultra-relativistic limit the transverse chromo-electric fields are created immediately after the initial time. In practice, the creation of the so-called flux tubes takes a certain amount of time. This creation leads the circular pattern in the energy density distribution [8, Figure 2.4]. These field

components contribute to the total energy density of the system as will be discussed in Figure 4.3 which results in the $1/\tau$ -behavior.

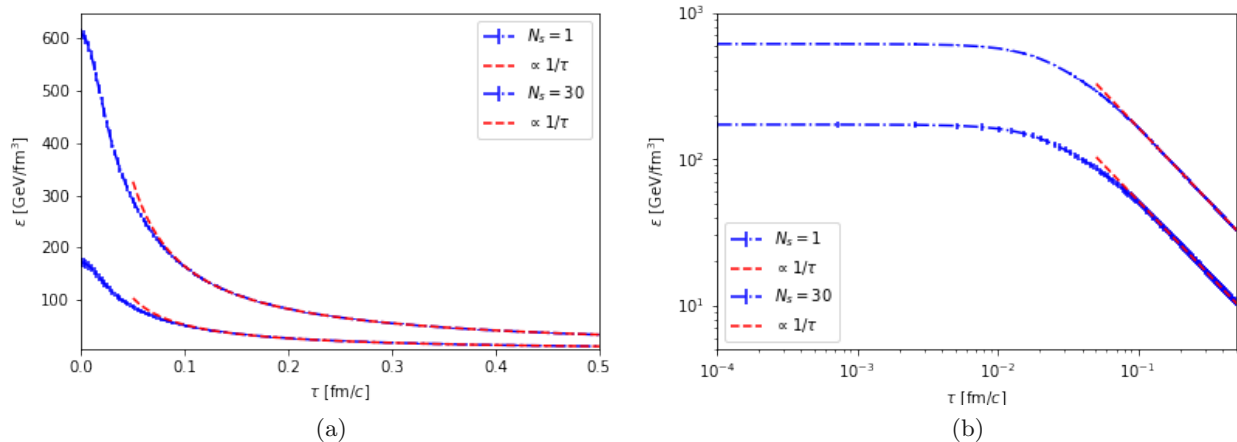


Figure 4.1: Total energy density simulated on a 1024^2 lattice with $L = 12.9$ fm averaged over 25 events plotted on a linear (left) and on logarithmic (right) grid. A screening mass $m = 0.2$ GeV and a UV-cutoff $\Lambda_{UV} = 20$ GeV were chosen. The results for the single color-sheet approximation are compared with the generalized MV-model using $N_\eta = 30$ color-sheets.

Since the MV-model suffers from UV-divergences at early times and thus is strongly lattice spacing dependent we do not compare the energy densities for initial times. Instead these values are compared at $\tau = Q^{-1} = 0.1$ fm/c with [8], [44]. This observation time is chosen since the near boost invariance of the Glasma is expected to hold at this time and the UV-divergences are no longer dominant. At this observation time we achieved an energy density for the single color-sheet approximation of 50.3 GeV/fm³. For 30 color-sheets we calculated an energy density of 162.3 GeV/fm³. These values agree with the ones stated in [8] and [44] to good accuracy¹. As shown in Figure 4.1 the energy densities for $N_\eta = 30$ differ very much, however the qualitative behavior remains the same. It can be observed that the energy densities increases with the number of color-sheets. This increase slows down at approximately $N_\eta \approx 100$ since the sampling from the Gaussian distribution for the color charge density leads to a convergence towards the expectation value of the distribution [45].

The nature of the Glasma initial condition introduces another feature when investigating the behavior of the pressure components. The longitudinal and transversal pressure relative to the total energy density show that at initial time we have a fully anisotropic system in the sense that $p_T/\varepsilon = 1$ and $p_L/\varepsilon = -1$ [8]. For later times the expansion of the flux tubes is advanced due to the creation of transverse chromo-electric and chromo-magnetic fields which results in a decrease in the anisotropy of the system. Figure 4.2 shows that the isotropization phase ends at $\tau \approx 0.1$ fm/c and the system appears to settle in an (an-)isotropic state with $p_T/\varepsilon = 0.5$ and vanishing longitudinal pressure $p_L/\varepsilon = 0$. This feature can be observed independent of the number of color-sheets as it is dictated by structure of the initial conditions.

We separate the total energy density as described in Section 2.5 in its contributions of the transverse and longitudinal field components. In Figure 4.3 we see that the transverse field components are created shortly after the initialization and during the isotropization phase. This behavior was also shown in [43]. Further, we show the rescaled components in the second row of Figure 4.3

¹These values serve as a validation of the Glasma initial conditions that were implemented as part of the thesis.

since the absolute behavior creates the misleading impression of converging field contributions. In fact, we see in Figure 4.3c and 4.3d that the energy density components do not converge and show distinct dynamical behavior after the initialization. We will discuss these contribution in more detail in Section 5.

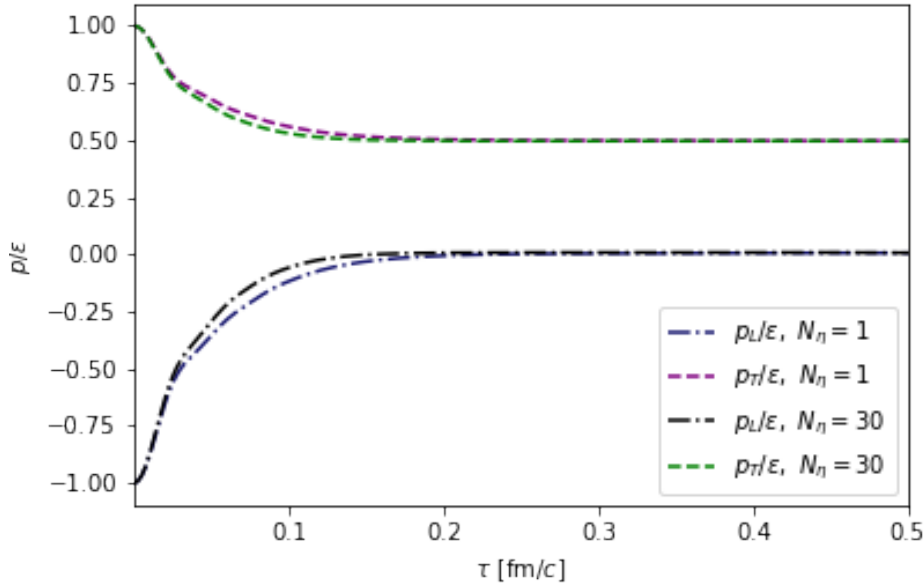


Figure 4.2: Transverse and longitudinal pressure components relative to the total energy on a 1024^2 lattice with $L = 12.9$ fm averaged over 25 events. A screening mass $m = 0.2$ GeV and a UV-cutoff $\Lambda_{UV} = 20$ GeV were chosen. The results for the single color-sheet approximation are compared with the generalized MV-model using $N_\eta = 30$ color-sheets.

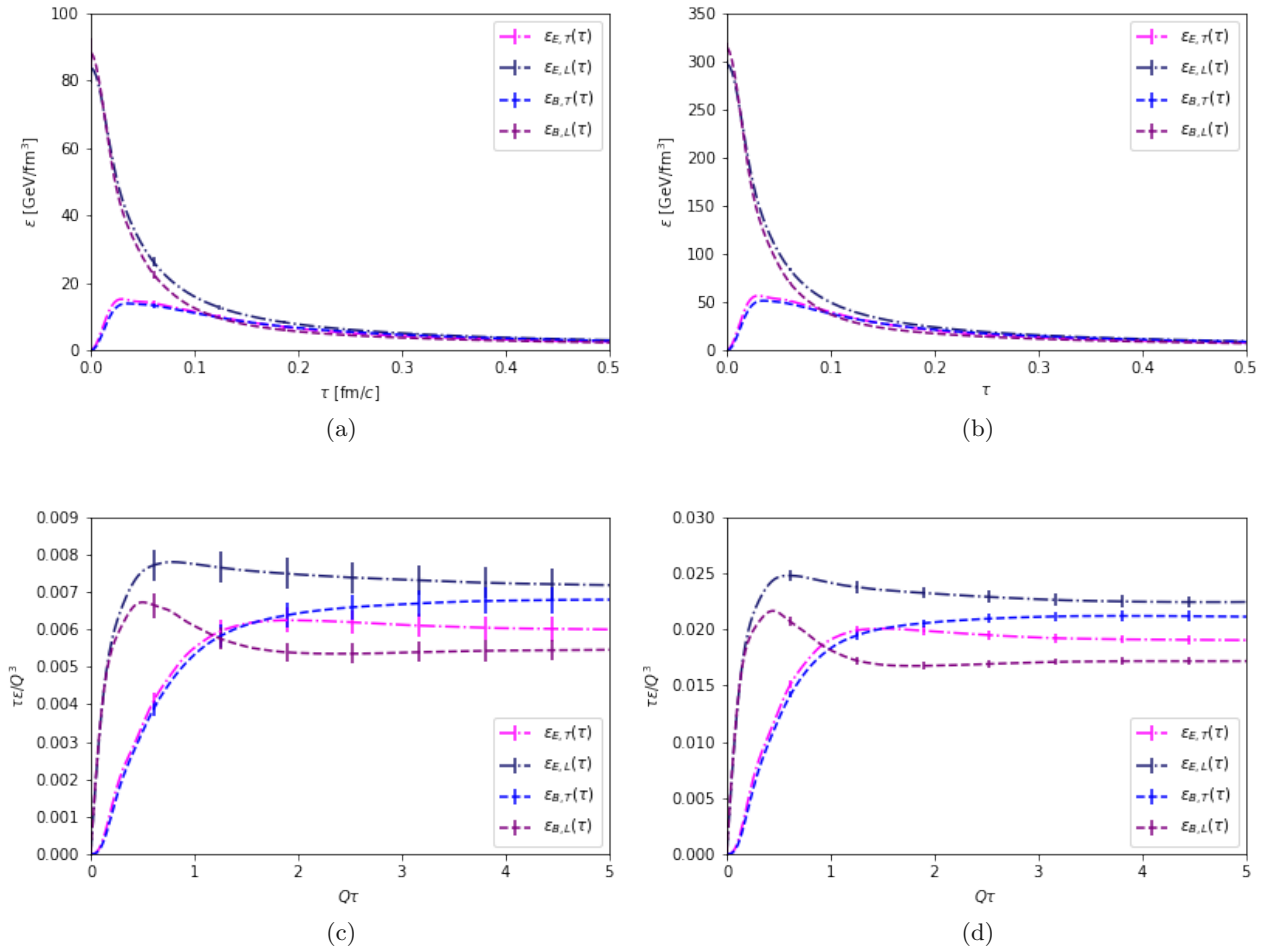


Figure 4.3: Energy density components on a 1024^2 lattice with $L = 12.9$ fm averaged over 25 events with a screening mass $m = 0.2$ GeV, UV-cutoff $\Lambda_{UV} = 20$ GeV and $Q = \mu g^2 = 2$ GeV. The results for the single color-sheet approximation (left column) and with $N_\eta = 30$ color-sheets (right column) are shown. The first row shows the absolute behavior for the energy density components, the second row shows the rescaled values for a more comprehensive comparison of the components.

4.2 Energy densities of gauge systems with Gaussian initial conditions

In this section we conduct an analogous discussion of the energy density as in Section 4.1 for Gaussian initial conditions and present a comparison between the expanding and the non-expanding case. Furthermore, we choose the conserved momentum Q , the initial amplitude n_0 and power law exponent κ such that the distribution function matches the computed occupancy numbers for the MV-model. In order to make this comparison physically meaningful we calculate the distribution at $\tau = 0.1$ fm/c. We do not use the initialization time $\tau = 0.0001$ fm/c for the MV-model because at this time the flux tubes are purely longitudinal and therefore no transverse fields have yet been created at that time. Table 4.1 shows the obtained parameters for the distribution function. Figure 4.4 shows a comparison between the distribution function of the Glasma at $\tau = 0.1$ fm/c and an approximation which we initialize for the Gaussian initial conditions of the form (3.2.13). Note, that we only approximate the gluonic distribution of the Glasma.

We emphasize that the Glasma initial conditions take all contributions from higher-order correlation function into account. In contrast, the Gaussian initial condition neglect these higher-order contributions and only initialize the 2-point correlation function. This means that the observed differences in the results for both types of condition (with similar distribution functions at $\tau = 0.1$ fm/c) can be used to assess the importance of higher-order contribution for 2+1 dimensional gauge systems in longitudinally expanding space-times.

Table 4.1: Parameters used for the comparison of the Glasma with the Gaussian initial conditions, obtained by fitting a curve at $\tau = 0.1$ fm/c with the computed distribution function for the MV-model. Both types of conditions were run on a 512^2 lattice with $L = 12.9$ fm.

Glasma IC			Gaussian IC		
N_η	m	Λ_{UV}	n_0	Q	κ
1	0.2	20	0.0036	6.1	1
30	0.2	20	0.0072	6.35	0.87

In Figure 4.5 we show the behavior of the energy densities for the expanding and non-expanding case where we used the parameters of Table 4.1 for the different color-sheet approximations with $N_\eta = 1, 30$. As expected we observe that the energy density in Minkowski space-times stay constant whereas the energy density for the Bjorken-expanding case shows a $1/\tau$ -behavior due to the longitudinal expansion.

At the observation time $\tau = 0.1$ fm/c the Glasma yields energy densities of 50.3 GeV/fm³ and 162.3 GeV/fm³ for $N_\eta = 1, 30$ respectively. For Gaussian initial conditions with the corresponding approximated distribution functions we obtained a smaller energy densities of 30.5 GeV/fm³ and 61.1 GeV/fm³.

However, one would expect that the Glasma and the Gaussian systems have the same energy densities as they are simulated on lattices of the same volume and have similar distribution functions. We emphasize that a possible explanation for this discrepancy is the fact that we neglected all higher-order connected correlation functions for the initialization with Gaussian initial conditions and only initialized the 2-point correlator. This would mean that we have to take higher-order contributions into account for expanding 2+1 dimensional gauge systems as they clearly are of significant importance.

Another possible source of the deviation of the energy densities for both types of initial conditions

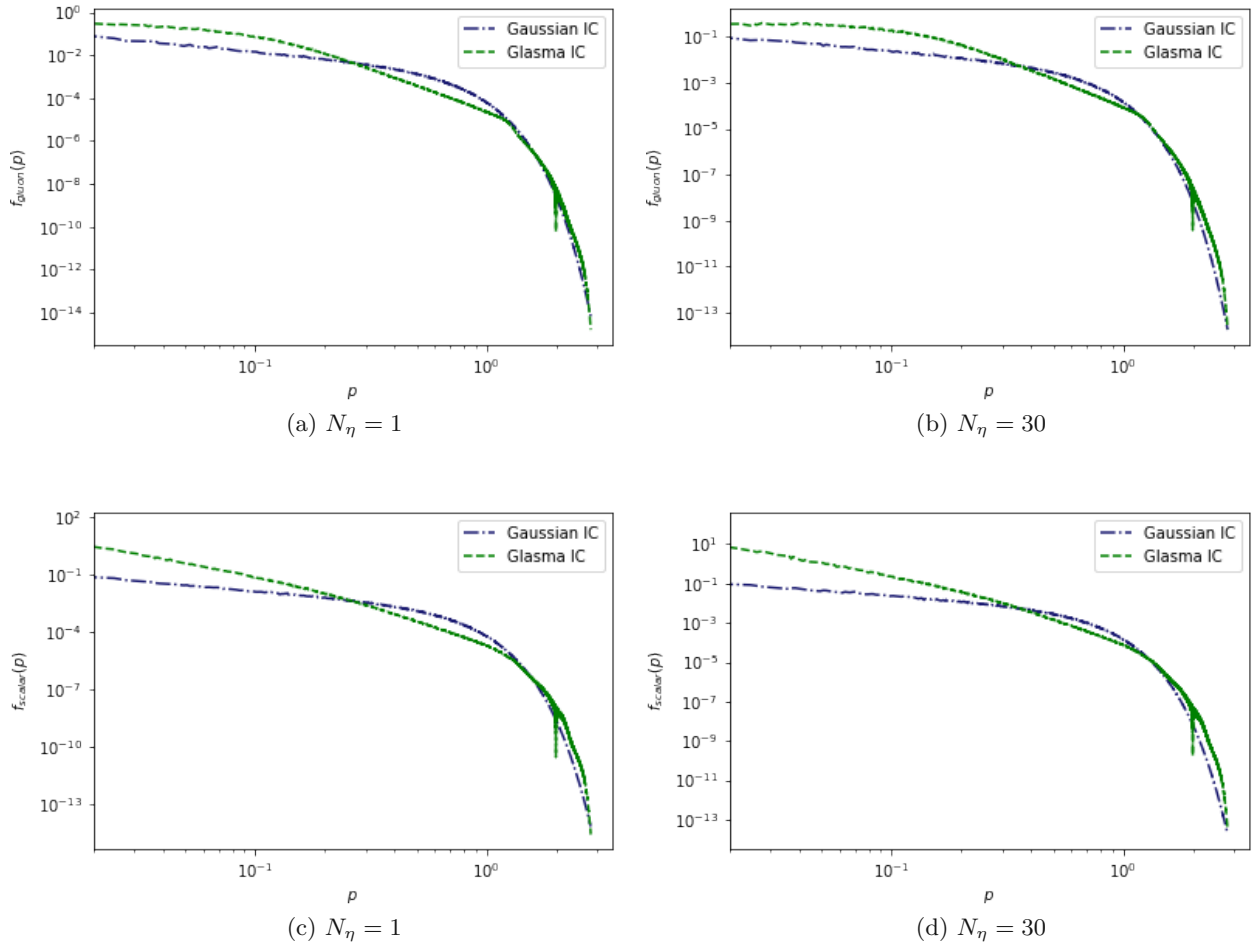


Figure 4.4: Comparison of distribution functions of simulated gauge systems at $\tau = 0.1$ fm/c for Gaussian and Glasma initial conditions for $N_\eta = 1, 30$. The gluonic distribution function for the Gaussian initial conditions was fitted such that it approximates the gluonic distribution function of the Glasma initial conditions at the observation time $\tau = 0.1$ fm/c and has the form (3.2.13). The obtained parameters are given in Table 4.1.

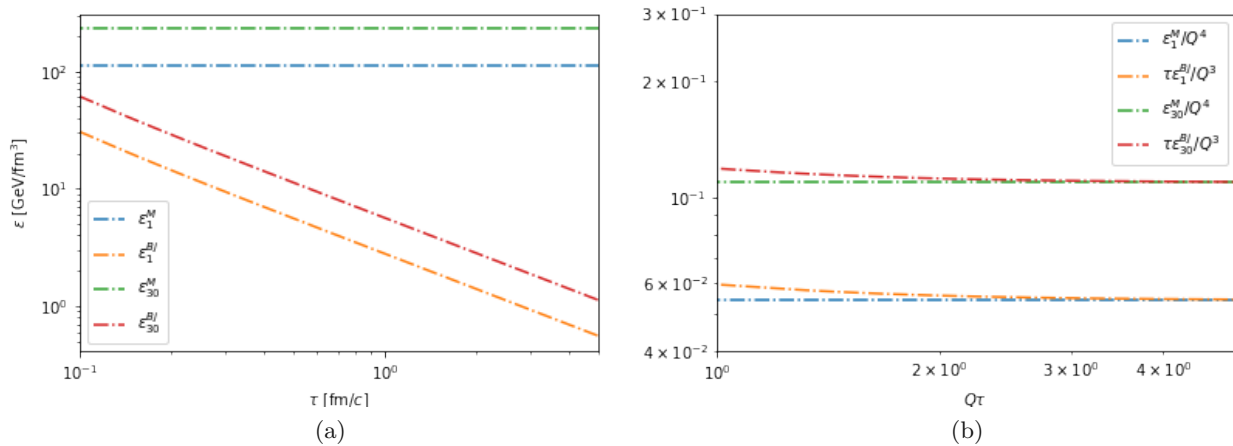


Figure 4.5: Energy density for Gaussian initial conditions. ϵ_1^M and ϵ_{30}^M denote the energy density for the non-expanding case using the parameter sets calculated for the distribution function of the MV-model at $\tau = 0.1$ fm/c for $N_\eta = 1, 30$ respectively. Similarly, ϵ_1^{Bj} and ϵ_{30}^{Bj} denote the energy densities for the expanding case. See Table 4.1 for the parameters of the initial distribution functions. The simulations were run for $\tau = 0.1 - 5$ fm/c on a 512^2 lattice with $L = 12.9$ fm.

yields the approach we used to approximate the distribution function. We approximated only the gluonic part of the distribution function which yields a deviation for the scalar distribution at the low momentum range as shown in Figure 4.4. The perturbative approximation of the energy density in Equation (3.2.14) suggests that this yields a deviation for the total energy densities, however it does not give a quantitative estimate of this deviation.

Furthermore, no initial isotropization phase as for the MV-model is observed. This can be explained by emphasizing that an essential difference between the MV-model and the Gaussian initial conditions are the non-vanishing transverse field components at initial time. Figure 4.6 shows the relative longitudinal and transverse pressure of the gauge system. The non-expanding system remains in the same (an-)isotropic state over the whole observation period with $p_T/\epsilon \approx 0.5$ and $p_L/\epsilon \approx 0$. In contrast to the MV-model we observe that the system experiences a phase where the system becomes less isotropic but settles at the same state as the static case. It is also observed that this behavior is independent of the parameter set calculated for the different approximations $N_\eta = 1, 30$.

For a better comparison between the expanding and the non-expanding systems we rescale the energy densities according to

$$\text{Minkowski:} \quad \epsilon \mapsto \frac{\tau\epsilon}{Q^3}, \quad (4.2.1)$$

$$\text{Bjorken:} \quad \epsilon \mapsto \frac{\epsilon}{Q^4}. \quad (4.2.2)$$

This yields dimensionless quantities and compensates the expansion rate with the multiplication of the proper time τ . In Figure 4.5b we observe that the rescaled quantities for the expanding and non-expanding case are converging.

Figure 4.7 shows the field contributions for the energy densities. We observe in Figure 4.7a and 4.7b that the longitudinal field components are increasing in the non-expanding case. Although the Bjorken space-time is longitudinally expanding this behavior appears to be reinforced by the expansion of the system. On the other hand, the fall-off behavior of the transverse field contributions is increased for the expanding case compared to the system in Minkowski space-time. Note that we refer to the rescaled quantities in this discussion in order to compare the non-expanding with

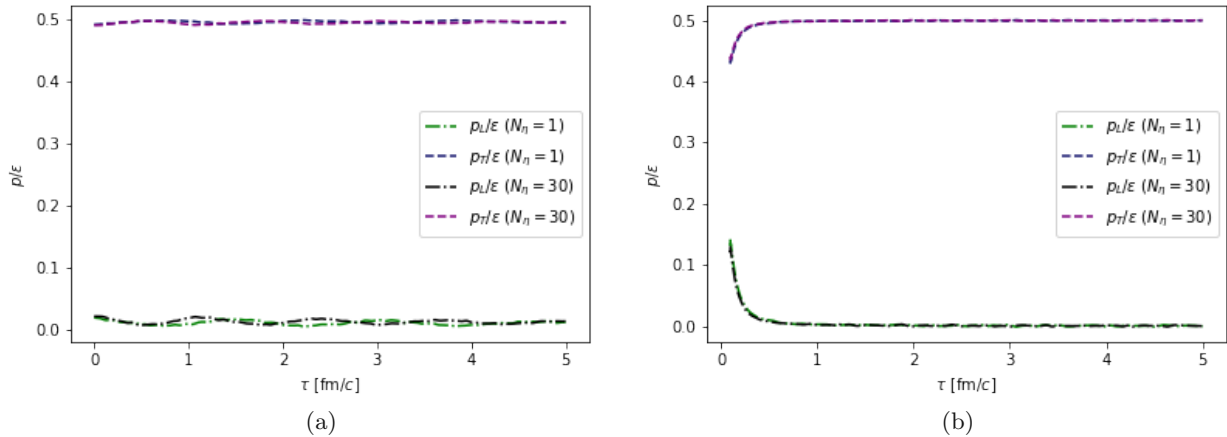


Figure 4.6: Transverse and longitudinal pressure components relative to the total energy density on a 512^2 lattice with $L = 12.9$ fm averaged over 50 events. Figure 4.6a shows the non-expanding case while Figure 4.6b shows the longitudinally expanding case for Gaussian initial conditions.

the expanding systems. For the absolute values of the energy density contributions the described behavior translates to the fact that the longitudinal energy densities decrease slower than $1/\tau$ while the transverse components are decreasing faster. This means that the dynamics of the expanding systems changes compared to the non-expanding system. Additionally, the system appears to converge to an isotropic system where all field components contribute the same to the total energy density. We will resume this discussion in Section 5.1 where we discuss the dynamics of these systems for a larger time scale.

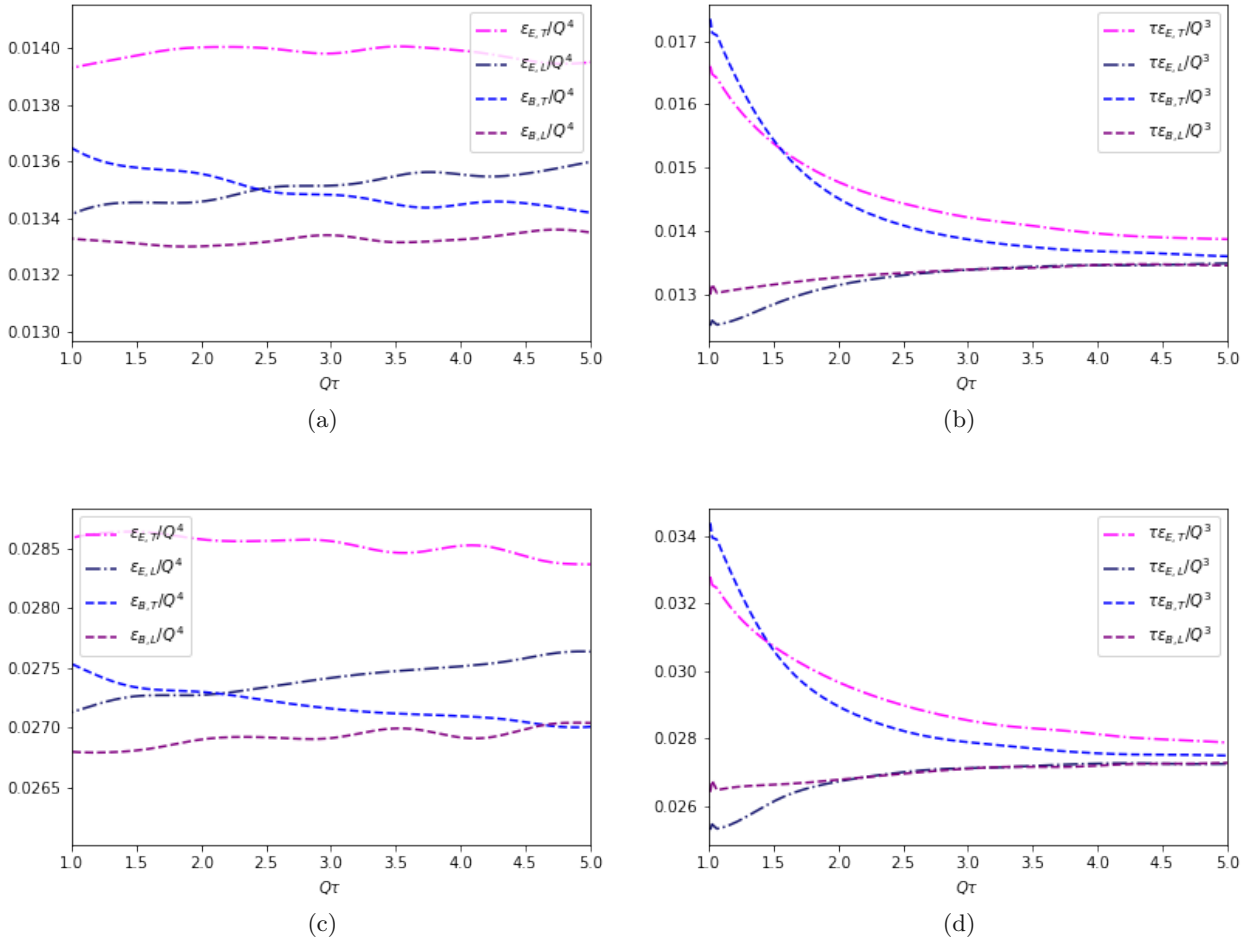


Figure 4.7: Energy density components for Gaussian initial conditions. Figures 4.7a and 4.7c show the energy density components in the Minkowski space-time for the parameter set for $N_\eta = 1$ and $N_\eta = 30$ respectively according to Table 4.1. The same is shown in Figures 4.7b and 4.7d for the expanding case. The simulations were run for $\tau = 0.1 - 5$ fm/c on a 512^2 lattice with $L = 12.9$ fm.

Chapter 5

Results for large time scales

In this section we discuss the dynamical behavior for Bjorken-expanding gauge systems in 2+1 dimensions on a large time scale and investigate the differences between Glasma and Gaussian initial conditions. Furthermore, we provide evidence that the longitudinal contribution of chromo-electric fields to the energy density grows linearly at late times for Glasma initial conditions when compared to the other contributions, while for Gaussian IC this is not the case. This marks an important difference between both sets of initial conditions, and we also give an explanation for this late-time property of Glasma initial conditions.

In Section 5.1 we observe the evolution of the energy density for Glasma initial conditions and its contributions. Next, in Section 5.2 we present the results obtained for the 2-point correlation function for the chromo-electric fields E and the color fields A and analyze the behavior for distribution functions introduced in Section 2.5. In order to underpin our understanding of the results we introduce four additional observables: hard momentum scales and characteristic occupancy numbers for gluons and scalars in Section 5.3. In Section 5.4 we discuss the dependence of the simulation results with respect to the lattice spacings and find that the granularity of the discretization does not have an effect on the observed dynamics. Finally, we discuss the most important differences to Gaussian initial conditions in Section 5.5.

5.1 Energy densities at large time scales of the Glasma

We now investigate the long-time behavior of the energy densities of gauge systems with Glasma initial conditions. Throughout this section all simulation results are shown for a screening mass $m = 0.2$ GeV and a UV-cutoff $\Lambda_{UV} = 20$ GeV. The coupling constant and the MV-parameter are chosen such that $Q = g^2\mu = 2$ GeV which we motivated in Section 4.1. For short simulation times we have already shown in Figure 4.1 that the energy density of the system evolves according to $\epsilon(\tau) \propto 1/\tau$ after $\tau = 0.1$ fm/c.

In Figure 5.1, we show the total energy density over an extended time window $0.0001 \leq \tau \leq 100$ fm/c for $N_\eta = 1$ and $N_\eta = 30$. We observe that at $\tau \approx 2$ fm/c the evolution of the energy density slows down. This change in behavior can be explained by computing the field contributions of the energy density, as shown in Figure 5.2. There we plot the rescaled energy density contributions $\tau\epsilon_\alpha$, where α denote the respective component of the chromo-electric and chromo-magnetic field. We see that the change of behavior for the total energy density is imposed by the longitudinal contribution of the chromo-electric field, which seems to grow linearly at late times and dominates the total energy density.

Further, in Figure 5.2, we observe that the transverse chromo-electric and the longitudinal chromo-magnetic contributions are converging and settle at a $1/\tau$ -behavior. We will give an interpretation of these observation by introducing a quasi-particle picture using the introduced single-particle distribution functions in Section 5.2. The transverse chromo-magnetic field on the

other hand is decreasing at a faster rate than the expansion.

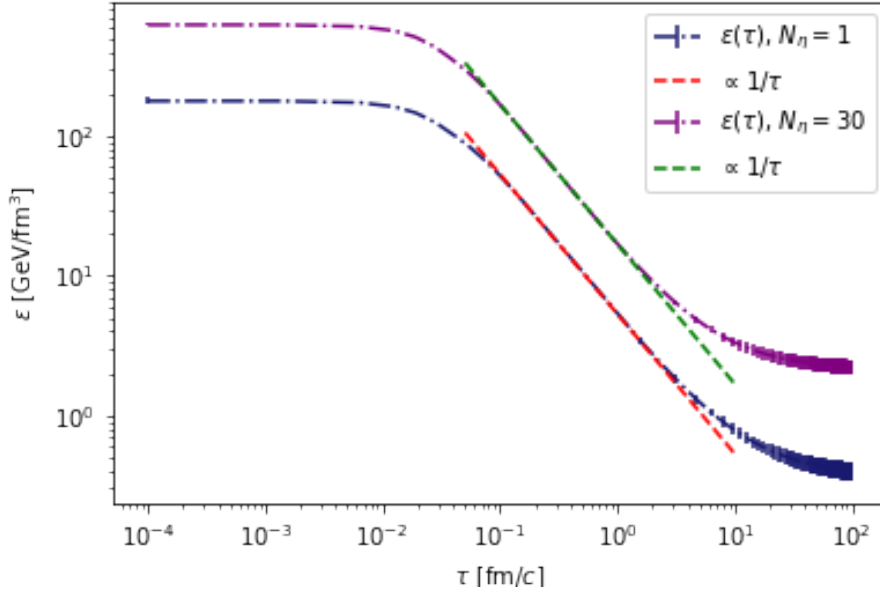


Figure 5.1: Total energy density of gauge systems with Glasma initial conditions simulated on a 512^2 lattice with $L = 12.9$ fm averaged over 50 events. The results for the single color-sheet approximation are compared with the approximation using $N_\eta = 30$ color-sheets. The simulations were run for $0.0001 - 100$ fm/c.

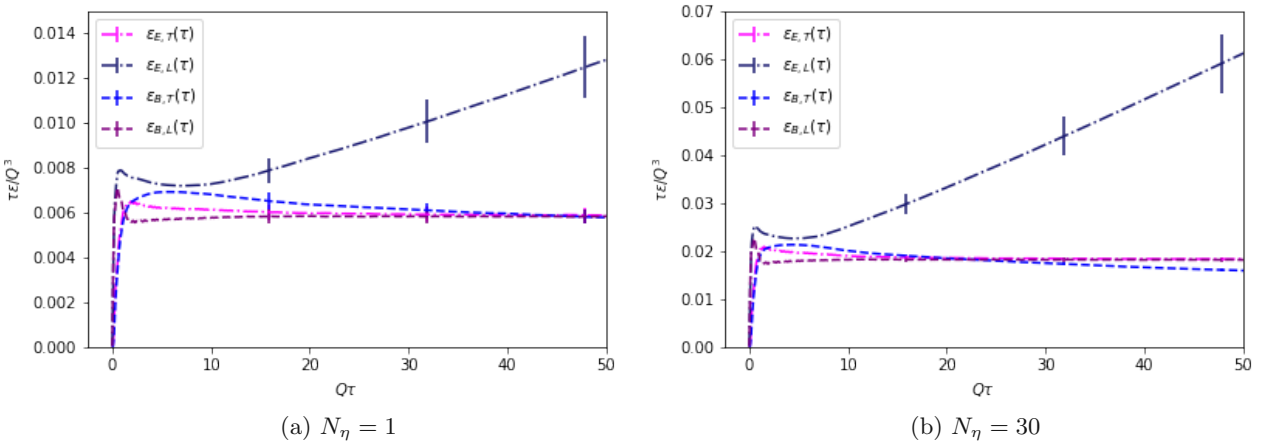


Figure 5.2: Rescaled energy density components τE of gauge systems with Glasma initial conditions simulated on a 512^2 lattice with $L = 12.9$ fm averaged over 50 events. The evolution for the single color-sheet approximation (left) and with $N_\eta = 30$ (right) color-sheets are shown. Both graphs show the results for $\tau = 0.0001$ fm/c – 5 fm/c.

Another feature of the dynamics at late times can be observed by focusing on the transverse and longitudinal pressure relative to the total energy density. As we already discussed in Section 4.1, the Glasma initial condition at initialization time are maximally anisotropic with $p_T/\epsilon = 1$ and $p_L/\epsilon = -1$ since the chromo-electric fields in transverse direction are not yet created. In Figure 4.2 it was shown that the system appears to transition into a system with $p_T/\epsilon = 0.5$ and $p_L/\epsilon = 0$ and settles there. However, after the isotropization phase we observe that the system returns into a maximally anisotropic state. This is shown in Figures 5.3a and 5.3b where we plot the longitudinal and transverse pressure of the Glasma relative to the total energy density for $0.0001 - 5$ fm/c and $0.0001 - 100$ fm/c respectively. Each of the figures compares the relative pressure component for the color-sheet approximation $N_\eta = 1, 30$.

One not only finds that the system starts to become more anisotropic after $\tau \gtrsim 1$ fm/c, but this transition is also faster for an increasing number of color sheets.¹ This evolution of the pressure components can be explained by taking into account that the longitudinal component of the chromo-electric field dominates the other contributions in the expression for both pressure components (2.5.6) at late times.

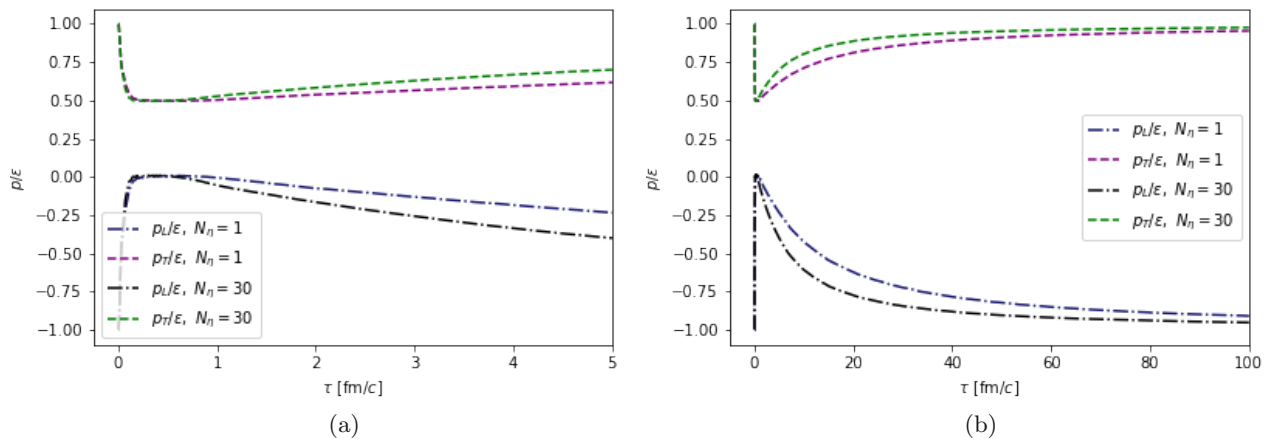


Figure 5.3: Transverse and longitudinal pressure components relative to the total energy density of gauge systems with Glasma initial conditions simulated on a 512^2 lattice with $L = 12.9$ fm averaged over 50 events. The results for the single color-sheet approximation are compared with the generalized MV-model using $N_\eta = 30$ color-sheets. The left figure shows the results for $0.0001 - 5$ fm/c where an almost constant behavior is observed for all shown quantities at $0.1 - 1$ fm/c. The right figure shows a larger time interval of $0.0001 - 100$ fm/c.

5.2 Distribution function and correlations at late-times of the Glasma

In this section we present the dynamical behavior of the 2-point correlation functions of the color field A and the chromo-electric field E at equal time of the conducted simulation for gauge systems described by the MV-model at initial time. We will continue to distinguish between the single-color sheet approximation and the generalized MV-model using 30 color-sheets because we have seen in

¹We have checked that for large $N_\eta > 100$ the behavior of the pressure evolution does not change with respect to the number of color sheets which is consistent with the dependency of the total energy density with respect to the color sheets.

Section 5.1 that they show different dynamical behavior. Throughout this section we assume a screening mass $m = 0.2$ GeV, a UV-regulator $\Lambda_{UV} = 20$ GeV and $Q = g^2\mu = 2$ GeV. We motivate the analysis of the dynamical behavior for these correlation functions by emphasizing that we can define a particle distribution function in terms of these function as given in Section 2.5.

In Figure 5.4 we show the total correlation function of the color field A in the sense that we sum over all 2-point correlation functions of the components of the gauge field A . We distinguish the components parallel to the momentum A_{\parallel} and orthogonal to the momentum A_{\perp} . As discussed in Section 2.5 we interpret the third component of the color-field as a scalar field and therefore denote this component with A_{Sc} . We observe no change in the evolution speed of the total correlation function for the color field A . Due to the expansion of the system we see that the amplitudes of this correlation function fall-off for increasing times independent on the number of color-sheets. For late times at $Q\tau = 625$ we see that the a steep decline with increasing momentum stops which indicates that quantities we observe diverge for large times since the integral over the momentum space will diverge.

Note that before we calculate the correlation functions we apply the Fourier acceleration method in order to impose the Coulomb gauge to make the results comparable and physically meaningful. The Coulomb gauge condition

$$\partial_i A^i = 0, \quad (5.2.1)$$

translates to $A_{\parallel} = p_i A^i / p \rightarrow 0$.

We plot the 2-point correlation function of each component of the color field in Figure 5.5. We can see that our implementation of the gauge fixing algorithm worked correctly Figures 5.5c and 5.5d, since the components parallel to the momentum are orders of magnitude smaller than the other components.

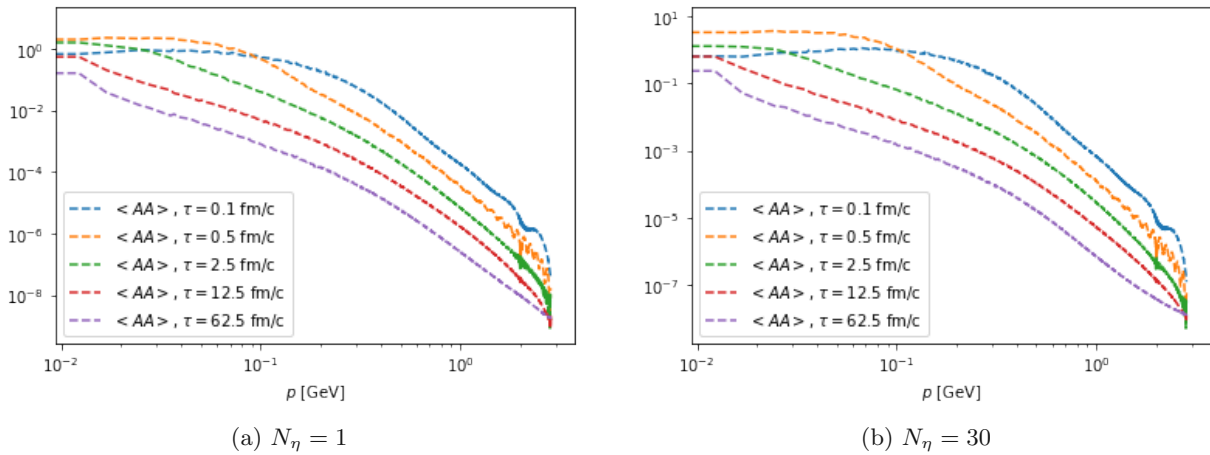


Figure 5.4: Total 2-point correlation function of the color field A at equal time for gauge systems described by Glasma initial conditions simulated on a 512^2 lattice with $L = 12.9$ fm averaged over 25 events. The results for the single color-sheet approximation are compared with the generalized MV-model using $N_{\eta} = 30$ color-sheets.

We set the relative numerical precision of 10^{-10} for the gauge-fixing algorithm in order to ensure that observation are not disturbed by a deviation of the gauge condition. However we point out the gauge fixing algorithm we used did not converge for all configurations following the MV-model. We therefore sampled the simulation runs were this was not the case and reached the desired precision. It is expected that the cause for this divergences are statistical outliers due to the stochastic nature

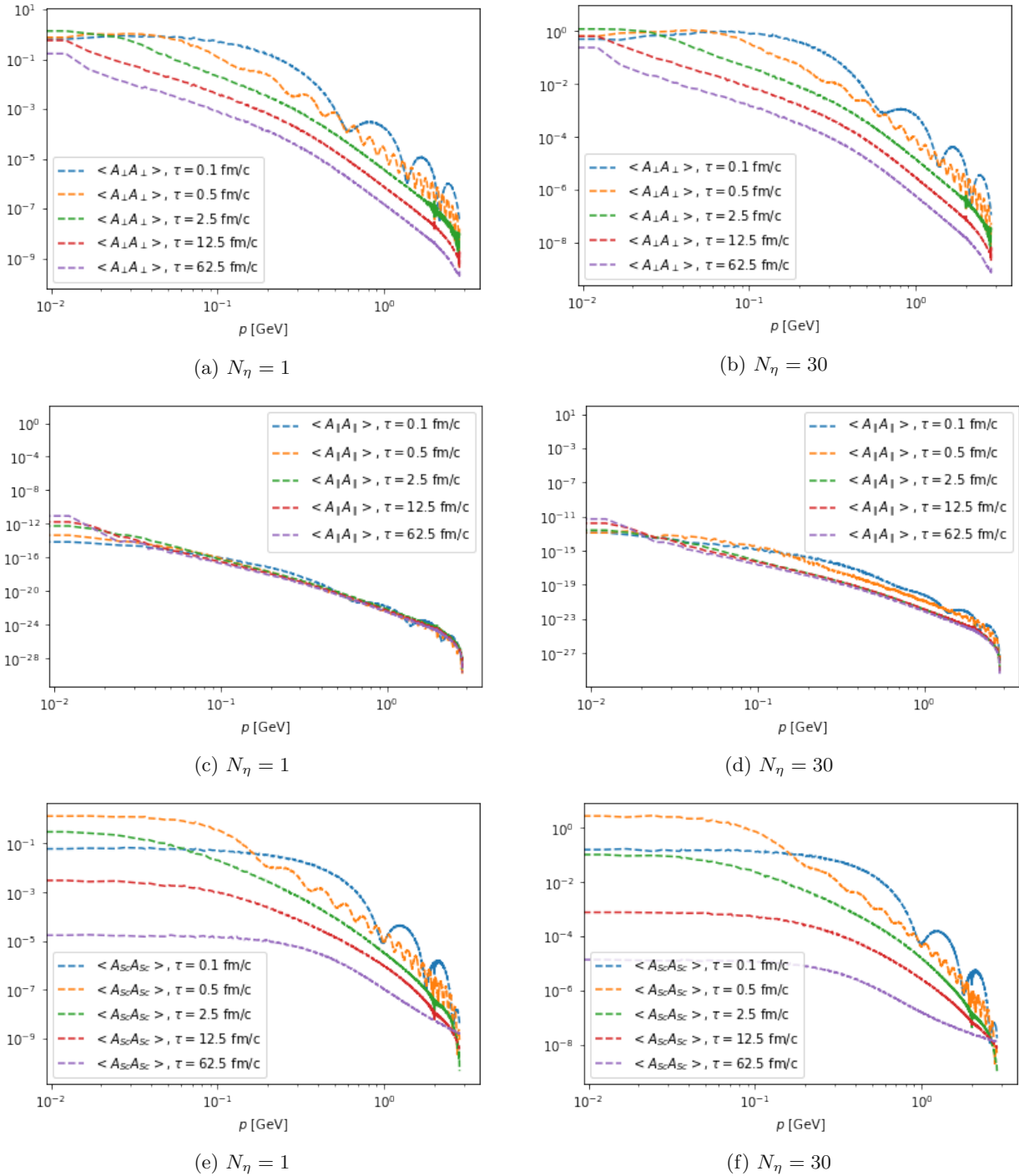


Figure 5.5: 2-point correlation functions for different color field components at equal time for gauge systems described by Glasma initial conditions on a 512^2 lattice with $L = 12.9$ fm averaged over 25 events. A_{\perp} and A_{\parallel} denote the field component perpendicular and parallel to the momentum respectively while A_{Sc} denotes the third color component which we interpret as a scalar field. The results for the single color-sheet approximation are compared with the generalized MV-model using $N_{\eta} = 30$ color-sheets.

of Glasma initial conditions but we did not investigate this further since no physically relevant information is expected to be obtained from such an analysis.

We further see in Figures 5.5a, 5.5b, 5.5e and 5.5f that both the transverse and the scalar parts of the 2-point correlation function do not change their dynamical behavior with respect to their velocity of the evolution. As expected both components decrease due to the longitudinal expansion of the system. In Figure 5.5a and 5.5b we see that the a step fall-off behavior with respect to the momentum is also given for later times whereas the scalar field components given in Figure 5.5e and 5.5f start flattening out with respect to the momentum at late times. Hence, the scalar component is responsible for the flattening out of total 2-point correlation function of the color field for large momenta.

Although we employed a different particle definition in this work the gluon and scalar occupancy defined in (2.5.25) and the fact that we observe that the longitudinal chromo-electric field contribution dominates the energy density at late times motivate the analysis of the correlation function of the chromo-electric field components. In Figure 5.6 we show the total chromo-electric field correlation function for $N_\eta = 1, 30$ and observe that it increases over time at the same rate regardless of the number of color-sheets. Similarly to the color field we see that for late times this correlation function does not decrease exponentially at late times for increasing momenta. This fact is interesting since it indicates that the occupation numbers for late times increase when employing the particle definition

$$f(\tau, p) = \frac{\langle E_a^i E_a^i \rangle(\tau, p)}{p} \quad (5.2.2)$$

introduced in Section 2.5. Note, that the depicted behavior needs to be multiplied by τ in order to account for the expanding Bjorken metric. Similar to the gauge fields we see that the described behavior is more pronounced for increasing numbers of color-sheets.

Figure 5.7 shows the components of the 2-point correlation function for the chromo-electric field. The parallel component appears static for large momenta. On the other hand Figures 5.7e and 5.7f show that the fall-off behavior with respect of the momenta flattens at late times for the scalar contribution. This suggests that specifically the occupation numbers for scalars increase at late times.

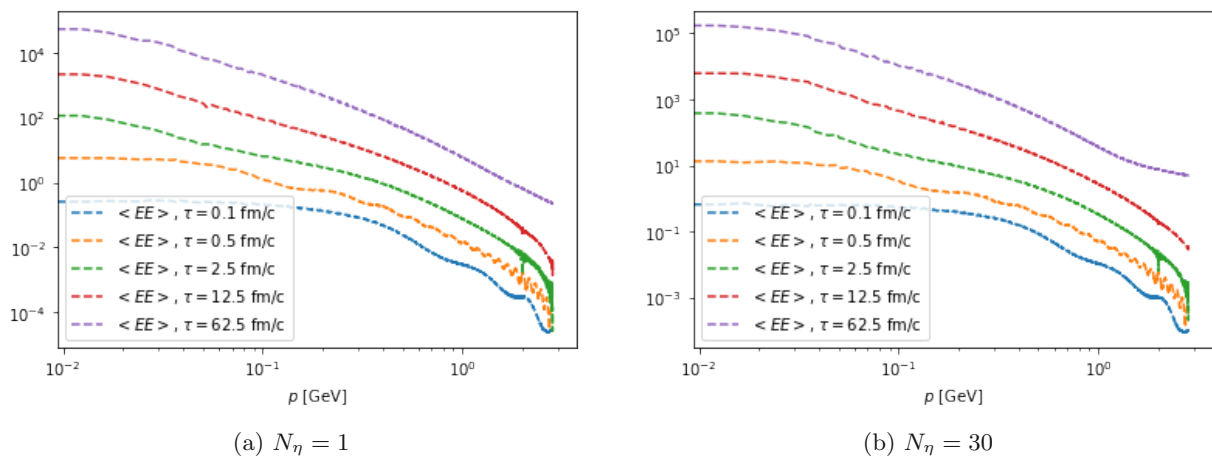


Figure 5.6: Total 2-point correlation function of the chromo-electric field E at equal time for gauge systems described by Glasma initial conditions simulated on a 512^2 lattice with $L = 12.9$ fm averaged over 25 events. The results for the single color-sheet approximation are compared with the generalized MV-model using $N_\eta = 30$ color-sheets.

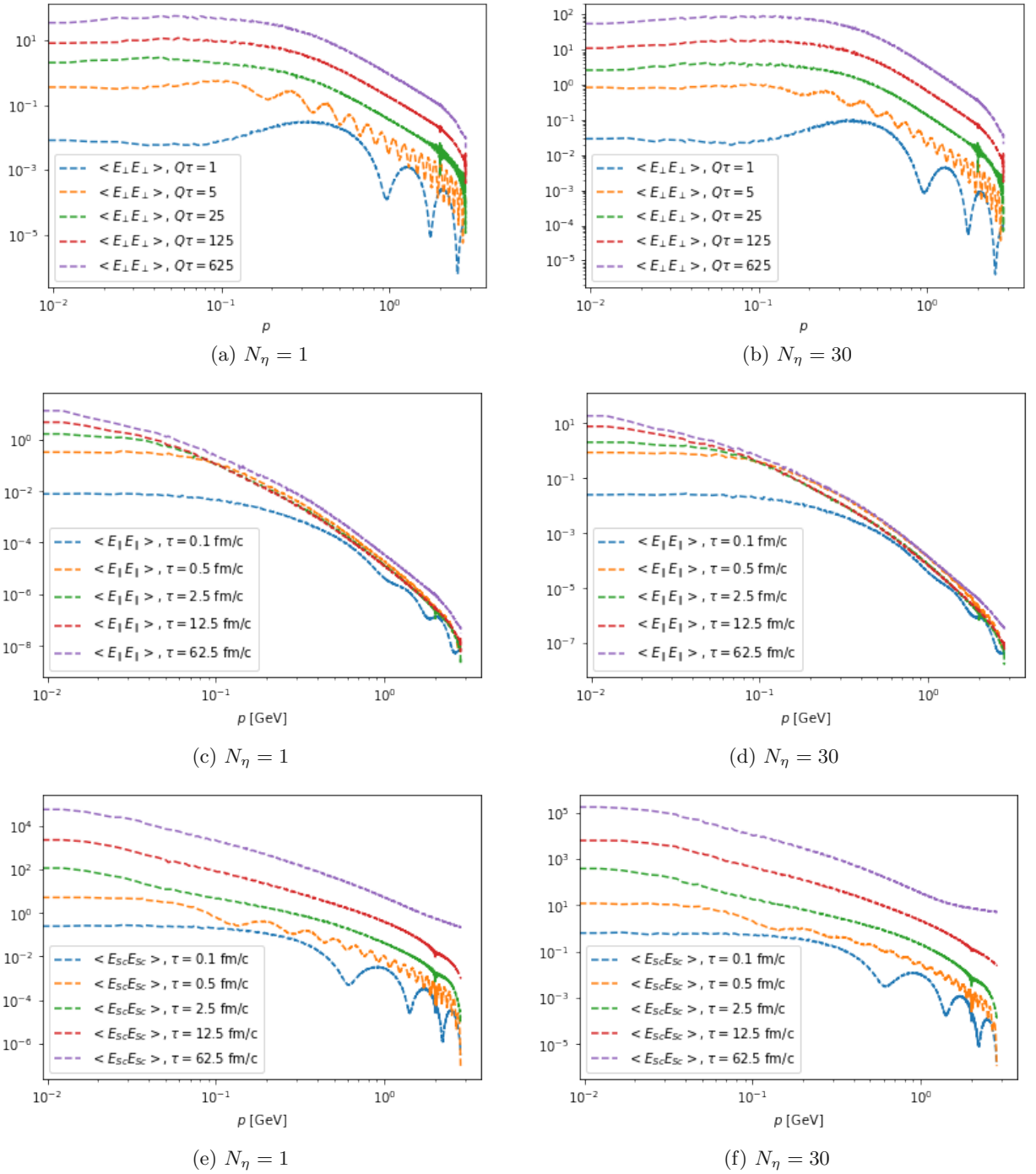


Figure 5.7: 2-point correlation functions for different color field E at equal time for gauge systems described by Glasma initial conditions simulated on a 512^2 lattice with $L = 12.9$ fm averaged over 25 events. E_{\perp} and E_{\parallel} denote the field component perpendicular and parallel to the momentum respectively while E_{Sc} denotes the third color component which we interpret as a scalar conjugate momentum field. The results for the single color-sheet approximation are compared with the generalized MV-model using $N_{\eta} = 30$ color-sheets.

In order to investigate the occupancy numbers for gluons and scalars we calculate the distribution functions for gluons and scalars introduced in Equations (2.5.20), (2.5.21). We plot these functions in Figure 5.8 for times growing by a factor five in order to get a clearer picture with regards to the relative growth in the logarithmic plot. We observe that the gluonic particle numbers show no dynamic for sufficiently large momenta. On the other hand Figures 5.8c and 5.8d show that the evolution of the scalar occupation number increases for late times and eventually shows the same flattening of the fall-off behavior as we already observed for the correlation functions.

We could find indicators for the unexpected blow-up for the contribution of the longitudinal chromo-electric field to the energy density at sufficiently late times which leads to an anisotropization phase yielding a maximally an-isotropic system. However, the correlation and distribution function do not give a full explanation of the dynamics observed on large time scales because the influence of higher-order contributions is not taken into account.

For a clearer picture we introduce a hard momentum scale which shall give a characteristic particle momentum of the system. Additionally, we introduce characteristic occupancy numbers in the next section.

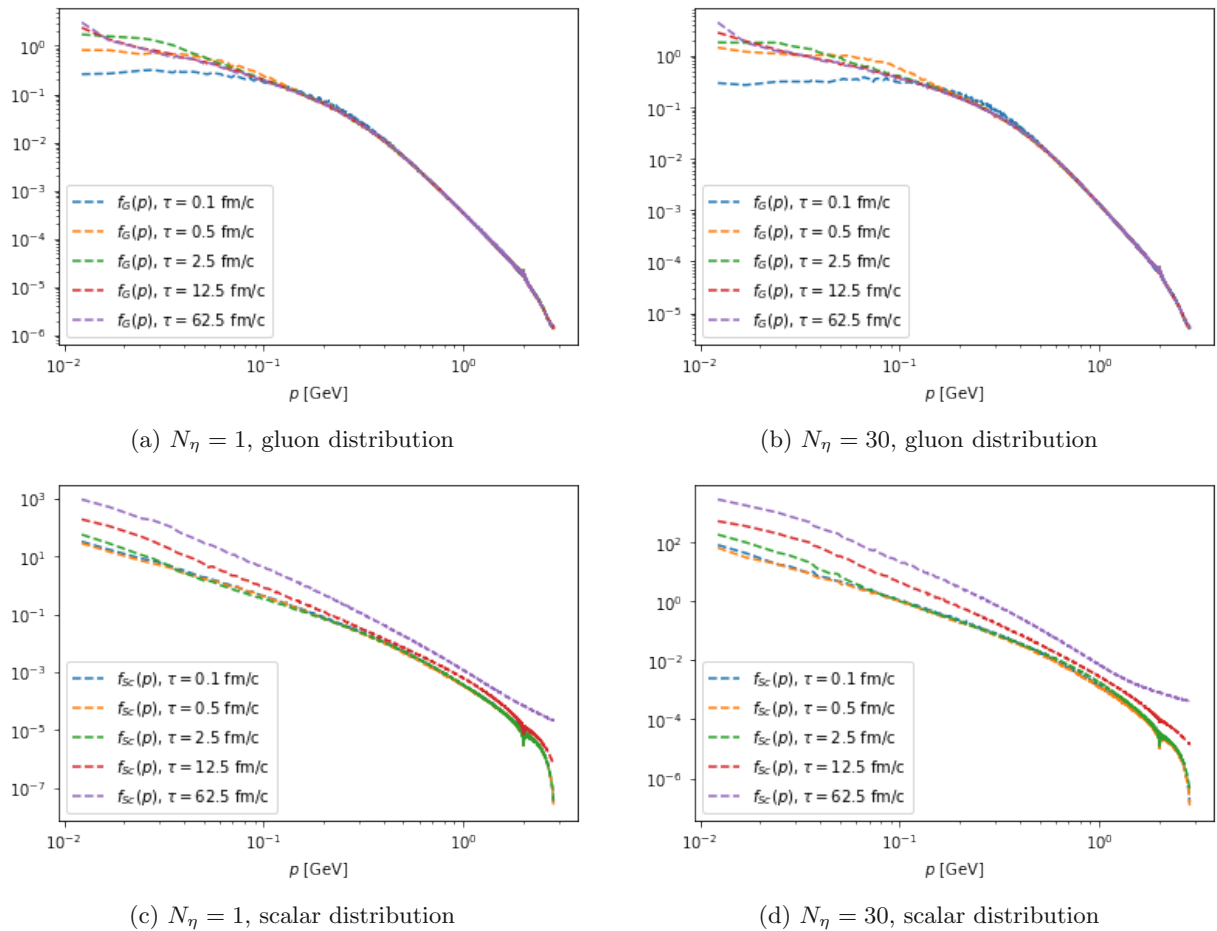


Figure 5.8: Distribution function for gluons f_G and scalars f_{Sc} for gauge systems described by Glasma initial conditions simulated on a 512^2 lattice with $L = 12.9$ fm averaged over 25 events. The results for the single color-sheet approximation are compared with the generalized MV-model using $N_\eta = 30$ color-sheets.

5.3 Hard momentum scales and characteristic occupancy of the Glasma

In order to get a better understanding of the dynamics of the observed systems we introduce the hard momentum scale given by²

$$\Lambda_G(\tau) = \frac{\int d^2p p^2 f_G(\tau, p)}{\int d^2p p f_G(\tau, p)}, \quad \Lambda_{Sc}(\tau) = \frac{\int d^2p p^2 f_{Sc}(\tau, p)}{\int d^2p p f_{Sc}(\tau, p)}. \quad (5.3.1)$$

This quantity yields a scale for the characteristic momentum of the gluons and scalar particles respectively. Figure 5.9 shows the simulation results of these scales and compares them for the single color-sheet approximation and the generalized MV-model with $N_\eta = 30$. We observe, that although the energy density contribution of the longitudinal chromo-electric component and the occupation for scalar fields change dramatically, the hard momentum scale of the scalars remains approximately constant. It only changes by 10% over the observation time of $0.0001 - 5 \text{ fm}/c^3$ and therefore does not provide an explanation for the dynamics of the system.

We further introduce the characteristic occupancy numbers for gluons and scalars, given by

$$N_G(\tau) = \frac{\int d^2p f_G^2(\tau, p)}{\int d^2p f_G(\tau, p)}, \quad N_{Sc}(\tau) = \frac{\int d^2p f_{Sc}^2(\tau, p)}{\int d^2p f_{Sc}(\tau, p)}. \quad (5.3.2)$$

This scale can be interpreted as the average number of gluons and scalars in the observed gauge systems. Figure 5.10 shows that the characteristic occupancy for gluons at early time for $0.0001 - 1 \text{ fm}/c$ grows which can be explained with the creation of the transverse chromo-electric fields after the initialization. For later times we observe that the gluon occupancy only changes marginally. The characteristic particle number of the scalars however stays constant until $1 \text{ fm}/c$ and grows linearly from that point on. Hence, for late times the gauge system settles in a state of significant scalar particle production. We can therefore conclude that not an increase of the momentum of the scalar particles is responsible for the change in the behavior of the energy density but rather the production of scalar particles.

²In the simulation we approximate the integrals with a finite sum over all lattice sites in momentum space.

³We observe the described behavior for a larger time scale of $0.0001 - 100 \text{ fm}/c$. The computational resources needed for these calculations are very high since at we have to restore the Coulomb gauge condition at each output time.

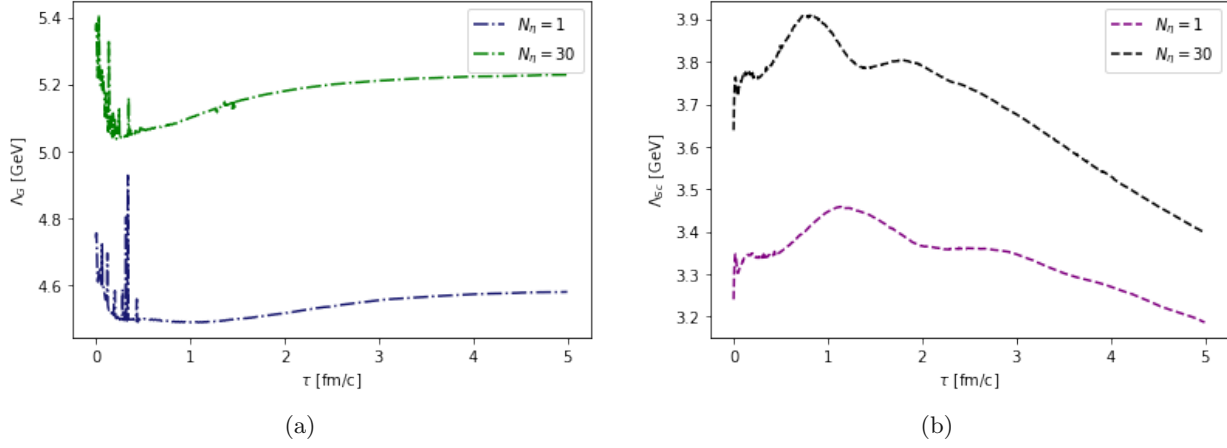


Figure 5.9: Hard momentum scales for gluons (left) and scalars (right) simulated for 0.0001–5 fm/c for gauge systems described by Glasma initial conditions simulated on a 512^2 lattice with $L = 12.9$ fm averaged over 25 events. The results for the single color-sheet approximation are compared with the generalized MV-model using $N_\eta = 30$ color-sheets in each figure.

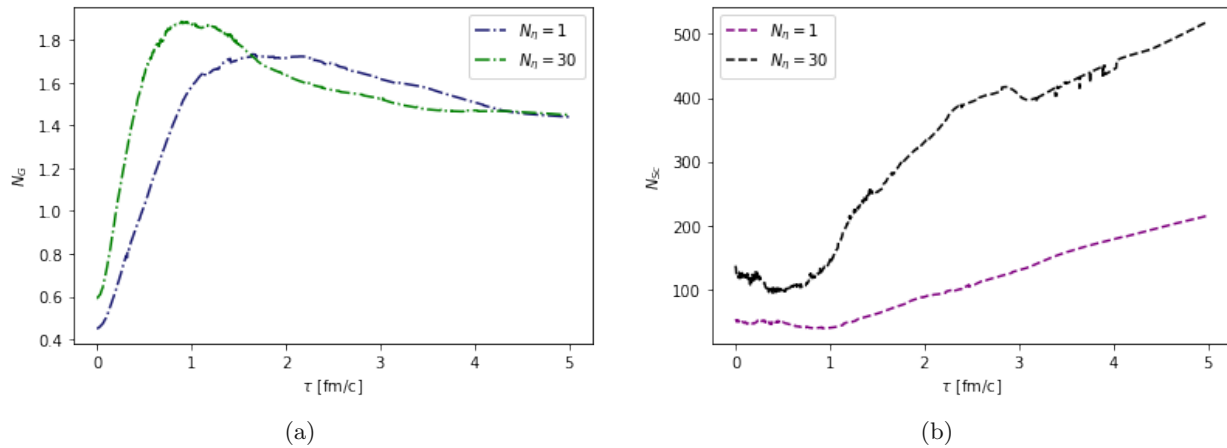


Figure 5.10: Characteristic occupancy numbers for gluons (left) and scalars (right) simulated for 0.0001–5 fm/c for gauge systems described by Glasma initial conditions simulated on a 512^2 lattice with $L = 12.9$ fm averaged over 25 events. The results for the single color-sheet approximation are compared with the generalized MV-model using $N_\eta = 30$ color-sheets in each figure.

5.4 Lattice spacing (in-)dependence of Glasma initial conditions

In order to ensure that the observed behavior is not an artifact from the discretization we discuss the differences we see in the dynamics depending on the lattice spacing. In Figure 5.11 we see that the total energy density remains unchanged for a sufficiently fine lattice with $N \geq 512$ and constant $L = 12.9$ fm. The total energy density shows the same deviation from $1/\tau$ -behavior at late times for all depicted discretizations. We further observe that the energy density in the initial phase of $0.0001 - 0.1$ fm/c for $a = 12.9/256 \approx 0.05$ fm deviates from the finer discretizations. This quantitative deviation can be explained by calculating the maximum momentum given by

$$p_{max} \approx \frac{2}{a} = \frac{2N}{L}. \quad (5.4.1)$$

For fewer lattice sites N in each direction and with constant lattice volume it is clear that the maximal momentum decreases. Therefore the UV cutoff, which was chosen as $\Lambda_{UV} = 20$ GeV in all results shown in Figure 5.11, has a greater effect on coarser discretized systems because it cuts off more modes relative to the total spectrum. However, the behavior after $\tau \approx 0.1$ fm/c aligns with the other discretization. For completeness we show the results for the energy density contribution

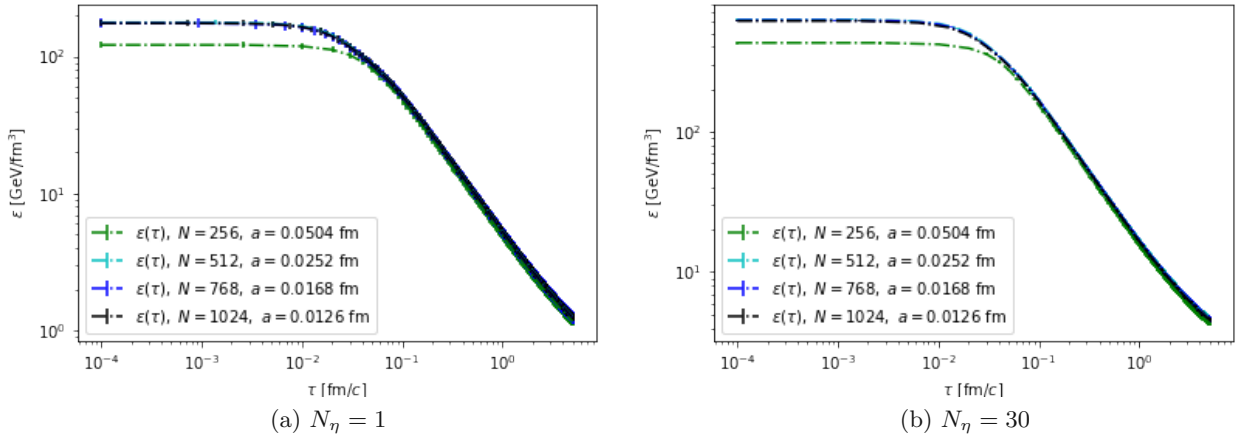


Figure 5.11: Total energy density simulated for gauge systems simulated on different lattice discretizations with $L = 12.9$ fm averaged over 25 events. The single color-sheet approximation (right) is shown next to the generalized MV-model using $N_\eta = 30$ color-sheets. The simulations were run for $0.0001 - 5$ fm/c. The results for the discretization $N = 512, 768, 1024$ yield near identical results which leads to indistinguishable curves for both approximations.

of the field components in Figures 5.12 and 5.13 for different discretizations. As for the total energy densities we observe that the dynamical behavior shows independence of the lattice discretization when taking the effect of the UV-cutoff into account. We emphasize that the rate of the increase for the longitudinal chromo-electric field contribution is independent of the lattice spacing.

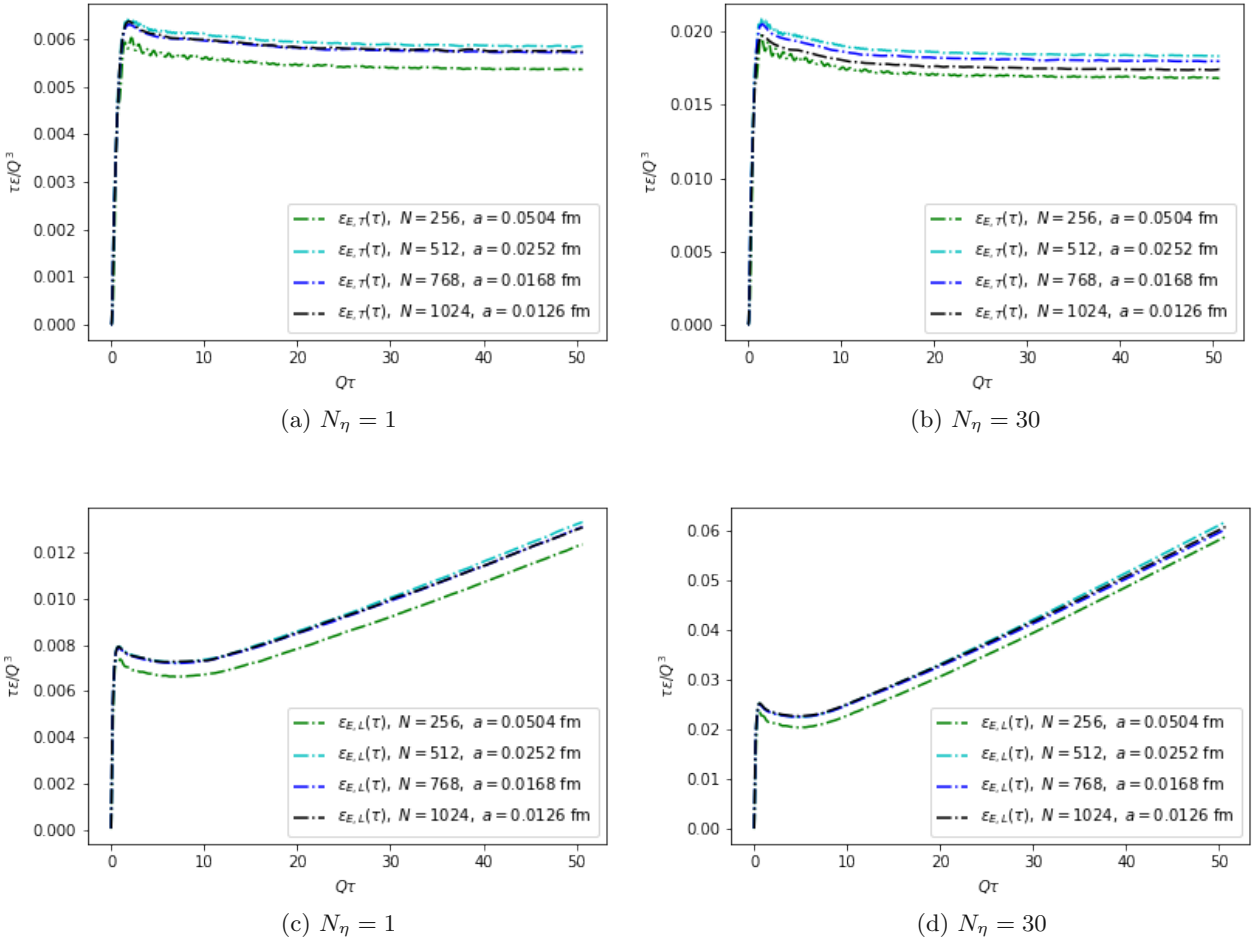


Figure 5.12: Energy density components of the chromo-electric field for gauge systems described by Glasma initial conditions and simulated on different lattice discretizations with $L = 12.9$ fm averaged over 25 events. The evolution for the single color-sheet approximation (top row) and with $N_\eta = 30$ (bottom row) color-sheets are shown. The results are shown for $\tau = 0.0001 - 5$ fm/c.

In Figures 5.14 and 5.15 we observe that the characteristic momentum scale and characteristic particle number show the same behavior for different lattice discretization. From these quantities we derived the physical interpretation of increasing scalar particle numbers which explains the increase of the longitudinal chromo-electric field and the correlated an-isotropization phase. We therefore conclude that the features of dynamical behavior described in the previous section do not originate from lattice artifacts.

We conducted similar analysis of the dependence with respect to the lattice spacing for the Gaussian initial condition and found no significant change for any of the computed observables.

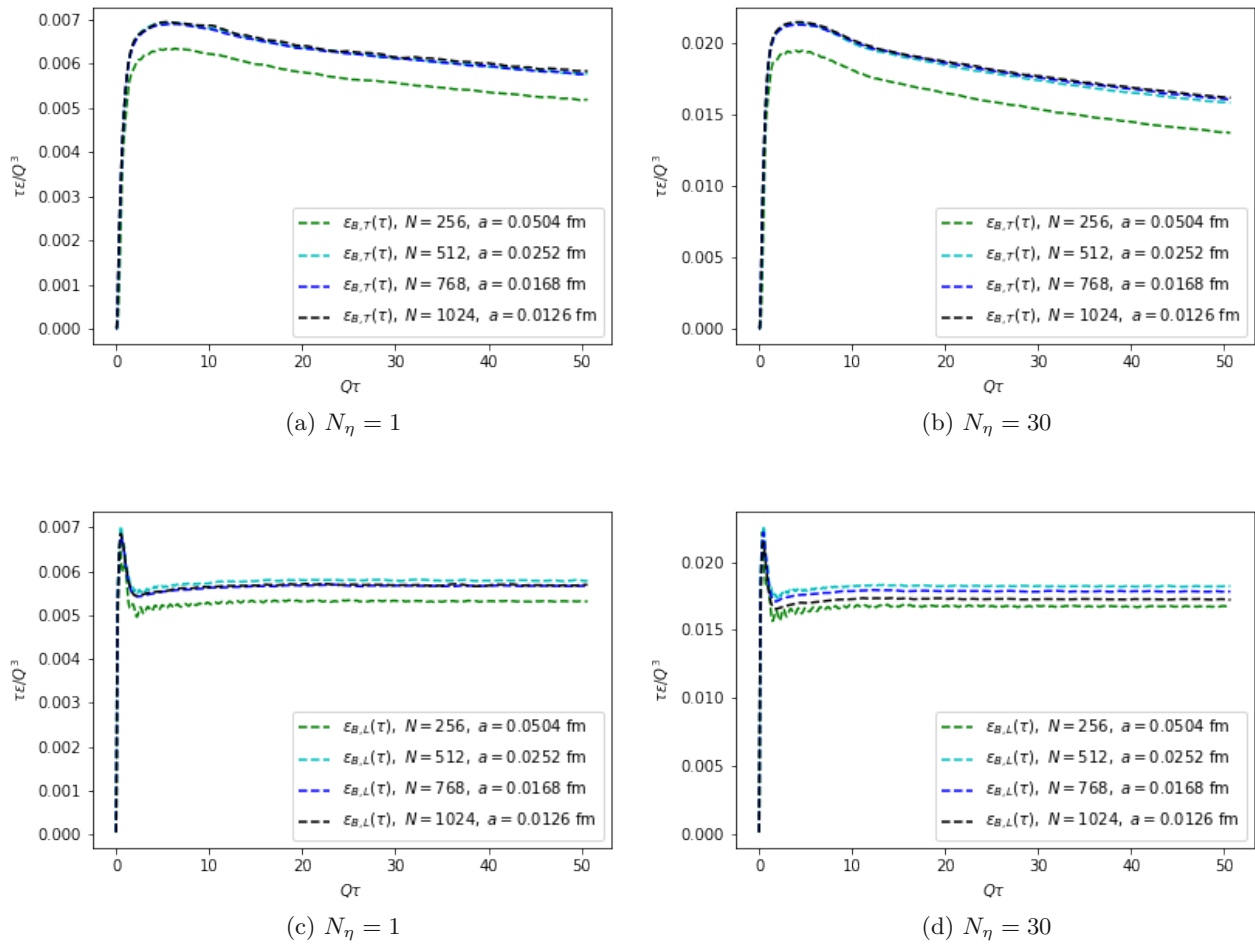


Figure 5.13: Energy density components of the chromo-magnetic field for gauge systems described by Glasma initial conditions and simulated on different lattice discretizations with $L = 12.9$ fm averaged over 25 events. The evolution for the single color-sheet approximation (top row) and with $N_\eta = 30$ (bottom row) color-sheets are shown. The results are shown for $\tau = 0.0001 - 5$ fm/c.

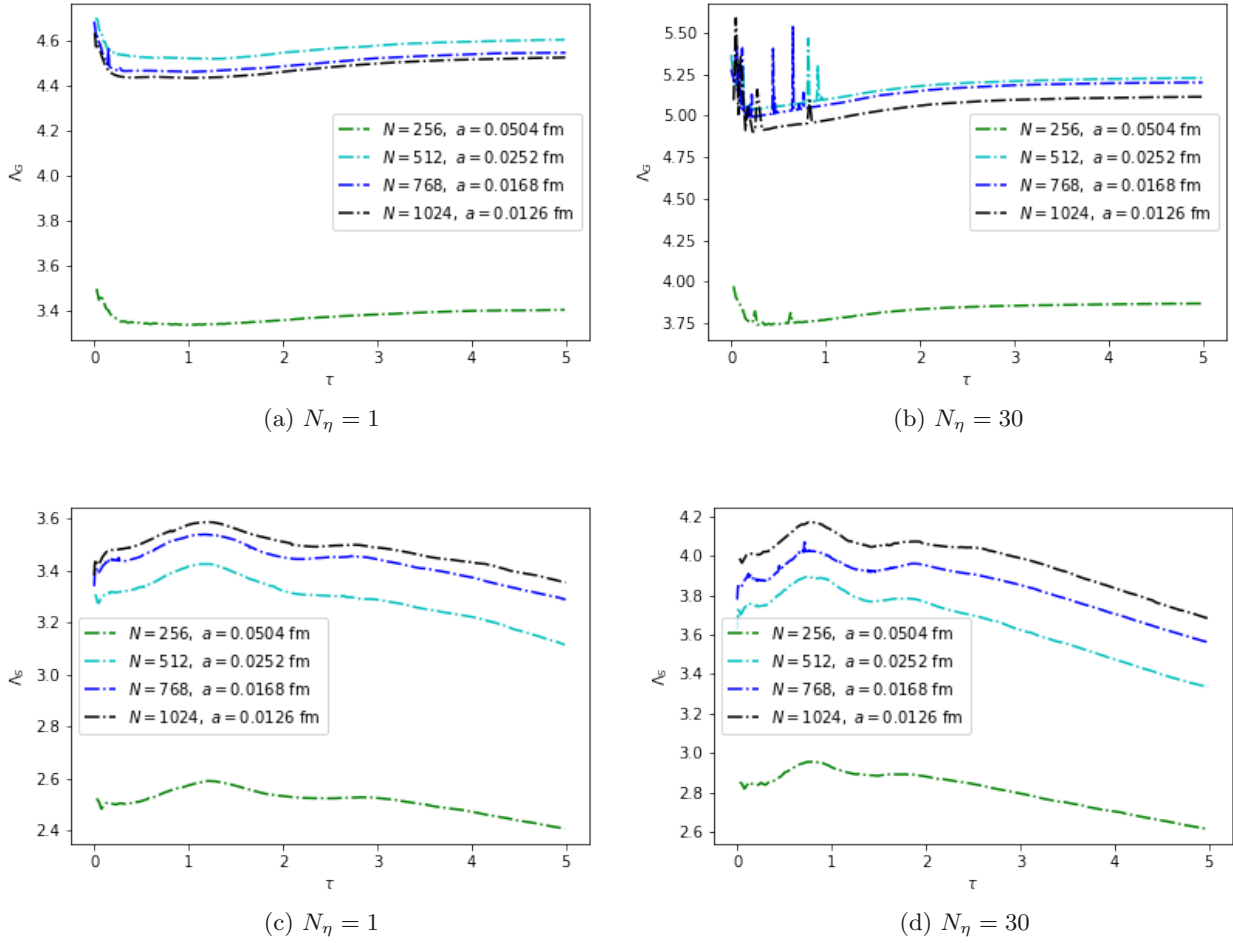


Figure 5.14: Hard momentum of gluons and scalars for gauge systems described by Glasma initial conditions and simulated on different lattice discretizations with $L = 12.9$ fm averaged over 25 events. The evolution for the single color-sheet approximation (top row) and with $N_\eta = 30$ (bottom row) color-sheets are presented. The results are shown for $\tau = 0.0001 - 5$ fm/c.

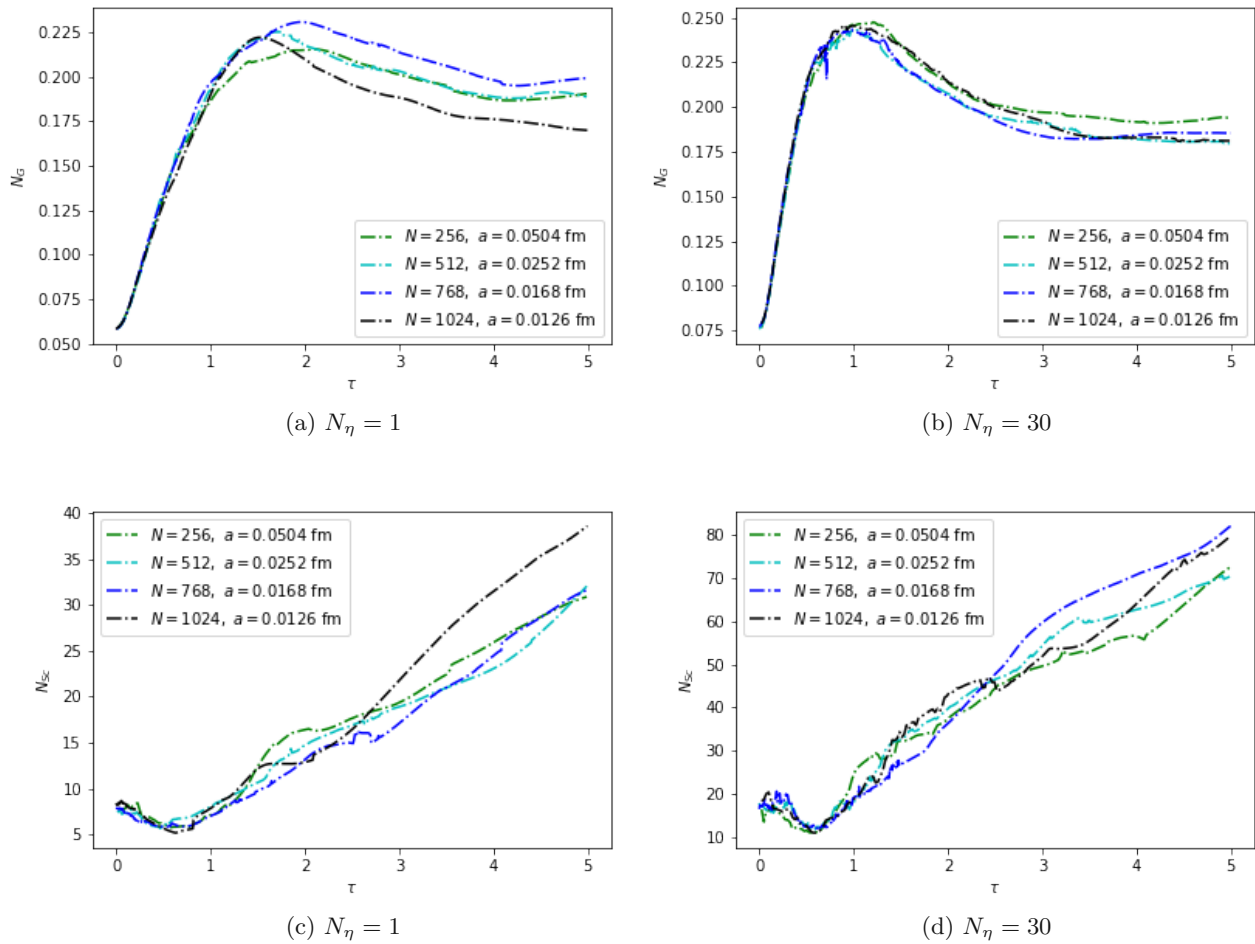


Figure 5.15: Characteristic occupancy numbers of gluons and scalars for gauge systems described by Glasma initial conditions and simulated on different lattice discretizations with $L = 12.9 \text{ fm}$ averaged over 25 events. The evolution for the single color-sheet approximation (top row) and with $N_\eta = 30$ (bottom row) color-sheets are presented. The results are shown for $\tau = 0.0001 - 5 \text{ fm}/c$.

5.5 Gaussian initial conditions for large time scales

In this section we conduct a similar discussion as in Sections 5.1-5.3 for Gaussian initial conditions. In Figures 5.16 and 5.17 we show the energy densities for Gaussian initial condition given by the parameter sets which emulate the distribution function given by the MV-model for $N_\eta = 1$ and $N_\eta = 30$ respectively at initial time $\tau = 0.1$ fm/c.

In Figure 5.16a we see that unlike for the MV-model the simulations show that there is no deviation from the $1/\tau$ -behavior for the total energy density at late times. Additionally, we observe in Figure 5.16b that the system undergoes no an-isotropization phase that we have seen for the Glasma initial conditions because the relative pressure components stay constant after a short initial phase.

Furthermore, in Figure 5.17 we see that the field contributions for the rescaled energy density settle at a constant level. This behavior is consistent with the relative pressure components shown above. The parameters for each approximation are given in Table 4.1. We can see that the former parameter set yields identical energy density components after an initial phase. The parameters given for $N_\eta = 30$ on the other-hand show distinguishable but almost congruent behavior of the energy density components at late times.

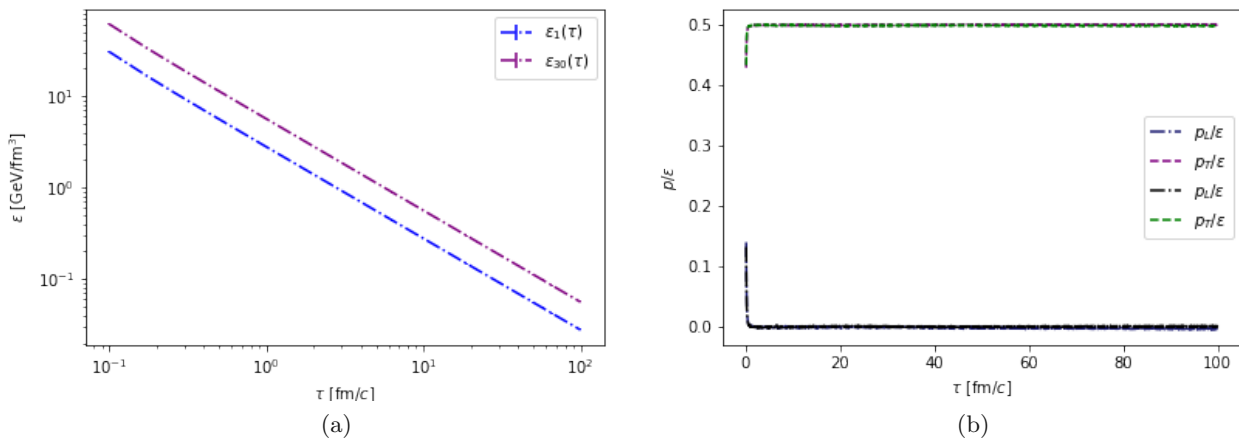


Figure 5.16: Total energy density (left) and relative pressure components (right) for Gaussian initial conditions simulated on a 512^2 lattice with $L = 12.9$ fm/c. The late time dynamics for each of the quantities are shown where we denote the Gaussian initial conditions with the parameters given in Table 4.1 by ϵ_1 and ϵ_{30} which specify the distribution function at $\tau = 0.1$ fm/c for the two color-sheet approximations used for the Glasma initial conditions.

The evolution of single-particle distribution functions of gluons and scalars for the Gaussian initial conditions is depicted in Figure 5.18. We observe that the gluonic occupancy numbers are completely frozen and do not change over time. We saw a very similar behavior for hard momenta of the gluon distribution function for Glasma initial condition, see Figure 5.8. However the scalar distribution function shows a very behavior. While for Glasma initial conditions the characteristic momentum scale changes slowly and mainly the occupation numbers grow, for Gaussian initial conditions the situation is completely different. The characteristic occupation numbers barely change while the main dynamics proceeds at hard momenta but changes characteristic momentum scales only slowly.

Hence, in contrast to the results we obtained for the characteristic occupancy numbers for Glasma initial conditions given in Figure 5.10 we do not observe a production of scalar particles for late

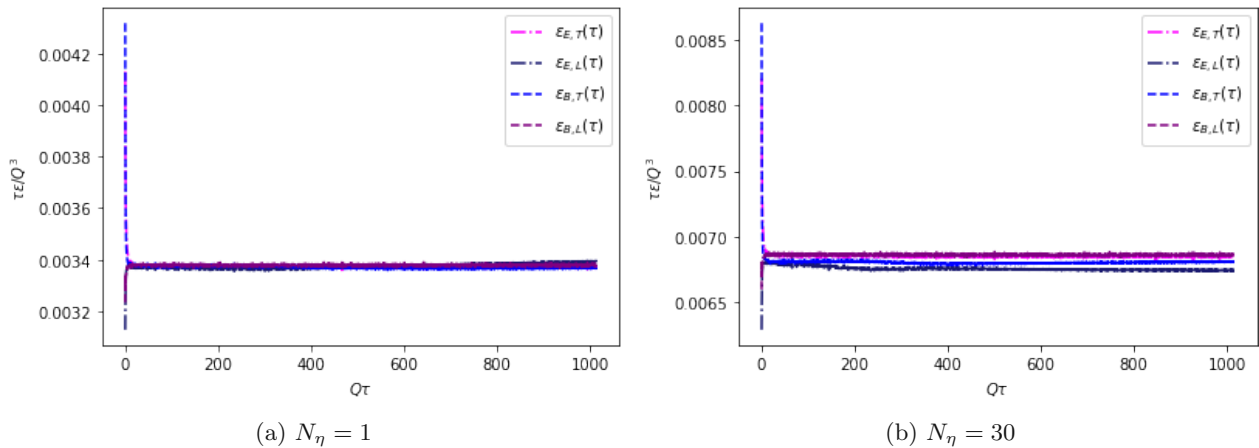
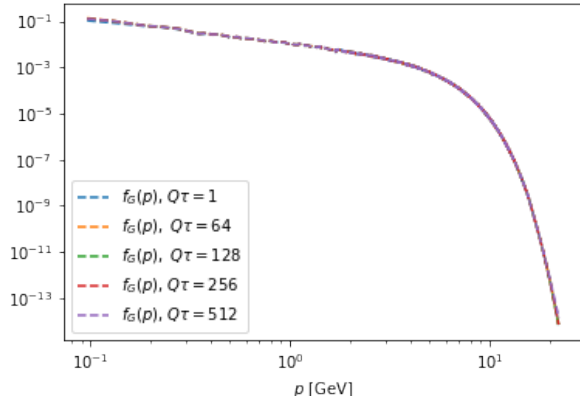
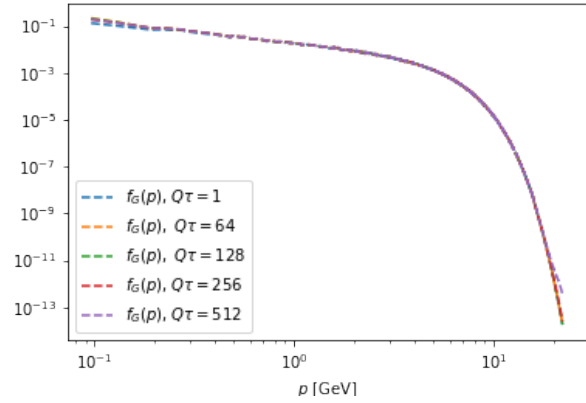


Figure 5.17: Energy density contribution for Gaussian initial conditions simulated on a 512^2 lattice with $L = 12.9$ fm/c. The right figure shows the system using the parameters obtained for distribution function of the single-color-sheet approximation for the Glasma at $\tau = 0.1$ fm/c. Similarly the parameters for $N_\eta = 30$ were used for the right figure.

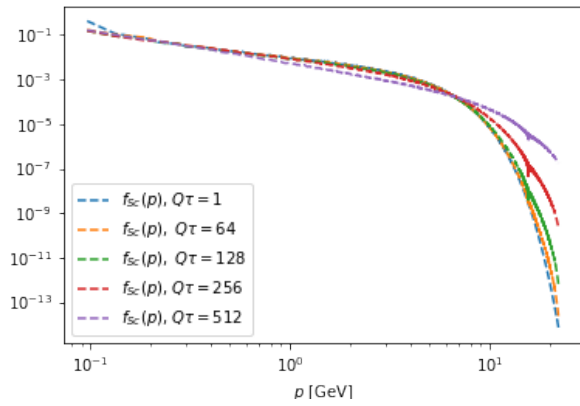
times when simulating gauge systems described by Gaussian initial conditions. This is further detailed in Figures 5.19c and 5.19d where we show that the characteristic scalar particle number decreases in a short initial phase while gluon particle numbers increase. After this phase we observe almost constant characteristic particle numbers. The hard momentum scales stay almost constant during the whole simulation period as depicted in Figures 5.19a and 5.19b. Hence, the comparison between Glasma and Gaussian initial conditions gives a consistent picture with regards to the relation between the introduced scales and the energy density.



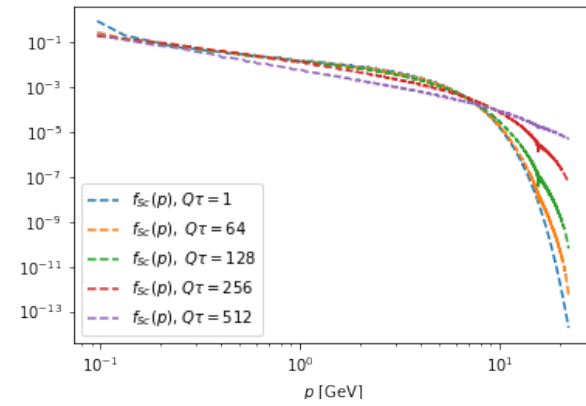
(a) $N_\eta = 1$, gluon distribution



(b) $N_\eta = 30$, gluon distribution



(c) $N_\eta = 1$, scalar distribution



(d) $N_\eta = 30$, scalar distribution

Figure 5.18: Single-particle distribution function of gluons and scalars for Gaussian initial conditions simulated on a 512^2 lattice with $L = 12.9$ fm/c. The figures in the top row show the system using the parameters obtained for distribution function from the single-color-sheet approximation for the Glasma at $\tau = 0.1$ fm/c. Similarly, the parameters for $N_\eta = 30$ were used for the bottom figures.

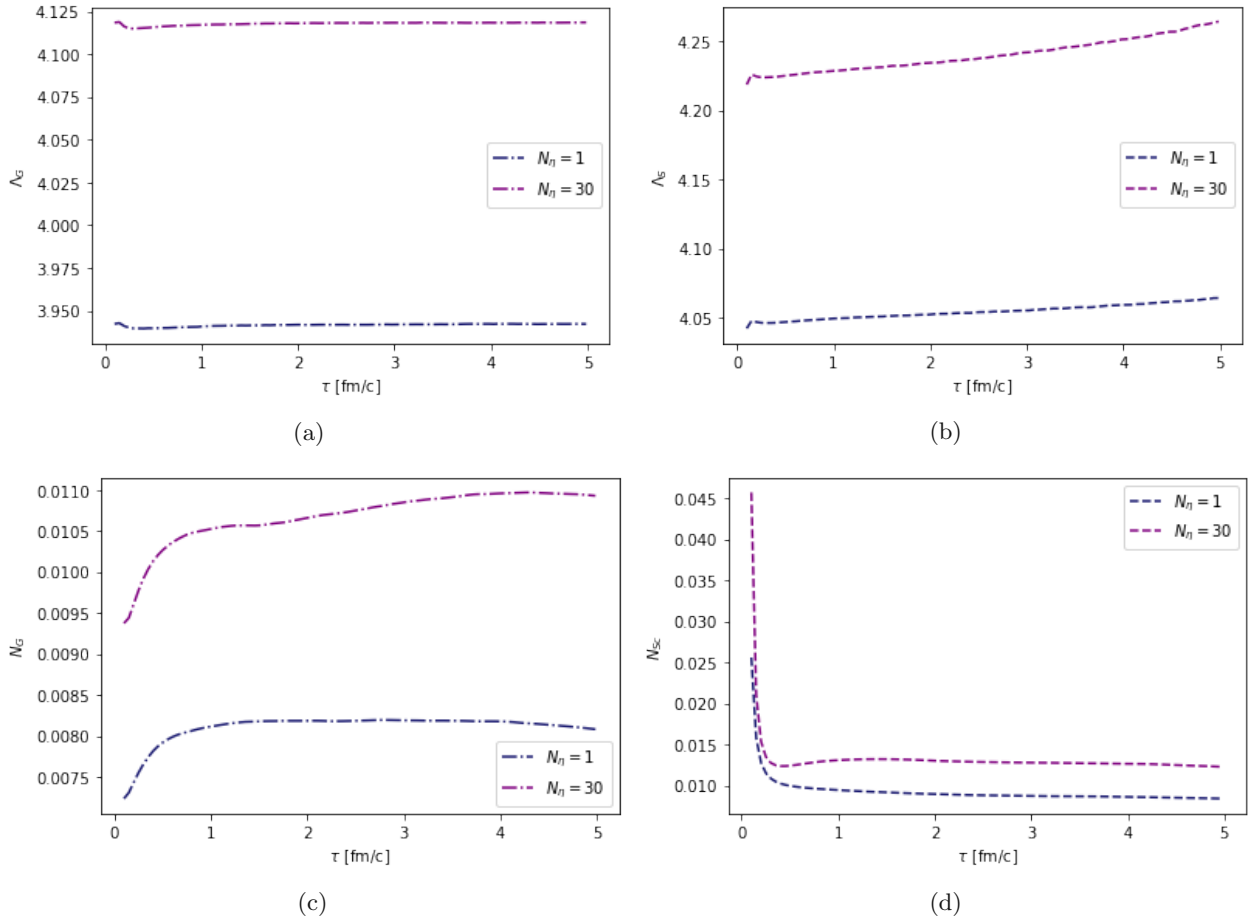


Figure 5.19: Hard momentum scales (top) and characteristic occupancy (bottom) for gluons (left) and scalars (right) for Gaussian initial conditions simulated on a 512^2 lattice with $L = 12.9$ fm/c. The figures show systems using the parameters obtained for distribution function using the single-color-sheet approximation and $N_\eta = 30$ for the Glasma at $\tau = 0.1$ fm/c.

Chapter 6

Conclusion

In this chapter we want to summarize the observations discussed in Chapter 4 and Chapter 5. We give an interpretation for the presented results and discuss the most important similarities and differences between Gaussian and Glasma initial conditions. Finally, we critically review our obtained results and approaches taken.

In this work we compared the dynamical behavior of Glasma initial conditions described by the MV-model [29, 28, 8] and the Gaussian initial conditions [35, 33] extended to large times scales. In particular, we conducted classical-statistical simulations of 2+1 dimensional gauge systems which are described by the single-color sheet approximation and the generalized MV-model [42] using $N_\eta = 30$ color-sheets. For the comparison with the Gaussian initial conditions we approximated the obtained distribution function for the Glasma at $\tau = 0.1$ fm/c and initialized the fields according to their mode-vector expansion [32].

In Chapter 4 we focused on the early stages of the simulation for $\tau < 1$ fm/c. We found that after short transient times the energy density of Glasma initial conditions shows a $1/\tau$ -behavior which is imposed by the longitudinal expansion of the system. Consistently with this observation the Gaussian initial conditions show the same qualitative behavior but without any initial transient phase. The difference in the behavior of the energy density at the early stage after the initialization can be explained with the structural difference of the initial conditions, as there are no transverse chromo-electric fields at initialization time for the Glasma.

Another commonality of the two types of initial conditions is that after a short phase after the initialization, both systems appear to settle in a state with the same degree of (an-)isotropy in the sense that the relative longitudinal and transverse pressure components are given by $p_L/\varepsilon = 0$ and $p_T/\varepsilon = 0.5$. Again, the difference between both with respect to the isotropy was observed right after the initialization where the Glasma undergoes a phase of isotropization whereas the Gaussian initial condition undergoes a phase of an-isotropization. This difference can be explained with the structural differences of both types of initial conditions.

Furthermore, we found that the values for the total energy density at the initialization phase of the Gaussian initial conditions at $\tau = 0.1$ fm/c differs from the value we calculated for the Glasma at the same time. This observation is surprising since at this observation time both systems are described by nearly the same distribution function. This represents evidence that for the Glasma the higher-order contributions of n -point correlation functions are of crucial importance because the Gaussian initial condition only initialize the fields according to the 2-point correlation and therefore might yield a smaller energy density. Other possible sources of this discrepancy are the approach to only approximate the gluon distribution while using the same distribution for scalars and that we conduct a Gauss restoration step after the initialization. Both of these sources can lead to further deviation of the distribution functions and therefore also of the energy densities of the systems. However, the effect of these deviations is not expected to justify the magnitude of the difference in the energy densities.

In Chapter 5 we discussed the dynamical behavior of the two types of initial conditions for a larger time scale. We observe for Glasma initial conditions that the longitudinal chromo-electric field dominates the other field contributions for $\tau > 1$ fm/c. These dynamics impose an anisotropization phase after the initial isotropization of the system. In Sections 5.2 and 5.3 we argued that this change in behavior results from the dynamical behavior of the scalar sector for the Glasma initial condition. The Glasma was observed to reach a state of linear scalar particle production after $\tau = 1$ fm/c which leads to a deviation of the total energy density from the $1/\tau$ -decrease. We further observed that the scalar distribution function grows over the whole momentum spectrum while the gluon distribution only shows dynamics for small momenta. This observation underpins the argument that the scalar sector is responsible for the dynamical behavior of the energy density. In Section 5.4 we argued that the dynamical behavior is independent of the lattice spacing and it is therefore ensured that the observations are not artifacts resulting from the discretization.

Interestingly, despite the similarity of the distribution functions for both types of initial conditions we could not observe the effects described above for the Gaussian initial conditions. The energy density evolves according to $1/\tau$ also at late times. Also the distribution functions evolve differently from the Glasma. We observed that the gluon distribution function is static while the scalar distribution grows slowly at high momenta at late times. This comparison is especially remarkable when taking into account that for Minkowski space-time it has been shown that the occupation numbers approach a universal self-similar attractor after some transient evolution [31, 33]. Evidently this is not the case for the expanding case. This is surprising since one might expect that at late times, at which the longitudinal expansion slows down, we will reach a state where we find similar features for the expanding plasma. This raises the expectation that for both types of initial conditions we would find similar dynamical behaviors at late times since they have the same distribution function at $\tau = 0.1$ fm/c. The discrepancy of the qualitative behavior substantiates the argument that the connected n -point correlation functions might have a large effect large effect for Glasma simulations.

We want to point out that throughout our analysis of the dynamical behavior for the distribution function we have used a definition using mode-vectors which assumes a vanishing effective mass. However, it is known that the effective gluon and scalar masses are created during the evolution which renders this definition as not ideal. We have shown that also other definitions of the distribution function lead to similar conclusions and can explain the dynamical behavior that we observed for the different components of the energy density.

We briefly summarize the commonalities between the dynamical behavior of Gaussian and Glasma initial conditions. We that both initial conditions yield a $1/\tau$ -behavior after $\tau = 0.1$ fm/c and also show the same isotropization level at this stage until $\tau \approx 1$ fm/c. Furthermore we observe that gluon distributions show no dynamical evolution for both systems and also find that the characteristic momenta are constant at late times. These commonalities further further substantiate the argument that the scalar sector is responsible for the differences in the dynamical behaviors described above.

Further future work might include an analysis of the dependence of the features for both types of initial conditions with respect to the initial time which determines the rate of expansion. Also a more accurate approximation of the Glasma distribution function as well as an assessment of the importance of higher-order n -point correlation functions pose interesting questions to better understand the dynamics of the observed systems. Another possibility to assess the underlying microscopic excitations and their differences among the initial conditions is provided by the analysis of spectral functions [52, 53, 54, 30].

Finally, our results suggest that the Glasma does not approach a clear quasi-particle picture, which would be the case if it showed the same qualitative behavior as for Gaussian initial conditions. For the theoretical description of heavy-ion collisions this implies that one needs to be very cautious when trying to describe the transition from the Glasma phase to a kinetic theory. In contrast, in

recent studies, a matching via the components of the energy-stress tensor was used instead to model the transition [10, 55, 21, 56, 57]. There are also many effects that we did not take into account, like plasma instabilities [58, 51, 59, 4, 60], which should be important to obtain a theoretically consistent dynamical picture of the initial states in heavy-ion collisions.

Appendices

A Properties of $SU(N_c)$ and $\mathfrak{su}(N_c)$

In this section we discuss the most important properties and aspects of Lie groups and their correspondence to Lie algebras. For this purpose we will restrict the discussion to matrix Lie groups which play a central role in quantum field theory.

Lie groups and Lie algebras

A Lie group is a finite-dimensional smooth manifold which forms a group with smooth group operations. For non-Abelian groups these operations are most often referred to as multiplication and inverse map. Very prominent examples for such groups are given by the matrix groups $SU(2)$ and $SU(3)$ which are discussed later in this chapter. The closed sub-group theorem [61] states that every closed sub-group of the general linear group $GL(n; \mathbb{C})$ forms a Lie group. Hence, it shows that the examples mentioned before represent proper Lie groups. Every matrix Lie group defines a Lie algebra which is a vectorspace over some field (in our case the real numbers \mathbb{R}) with an additional bilinear operation $[\cdot, \cdot]$, called the Lie bracket. This operation satisfies

$$[x, [y, z]] + [y, [z, x]] = -[z, [x, y]], \quad (\text{Bianchi identity}) \quad (\text{A.1})$$

$$[x, y] = -[y, x], \quad (\text{anti-commutativity}) \quad (\text{A.2})$$

for all $x, y, z \in \mathfrak{g}$.

The Lie algebra corresponding to a matrix Lie group G is given by

$$\mathfrak{g} = \{X \in M(n; \mathbb{C}) : \forall t \in \mathbb{R} e^{tX} \in G\}, \quad (\text{A.3})$$

where the Lie bracket is defined as the commutator.

Representations of Lie groups and Lie algebras

Lie groups in particle physics are used to describe certain symmetries of physical systems. This picture is very clear when discussing matrix Lie groups. However, in order to classify the action of a Lie group G on a more abstract level it is useful to define representations which are given by the homomorphism

$$\Pi : G \rightarrow GL(V), \quad (\text{A.4})$$

where V is some n -dimensional vectorspace. $GL(V)$ denotes the group of all invertable linear transformation on V . Since all matrix Lie groups are already subsets of $GL(n; \mathbb{C})$ and \mathbb{C}^n is isomorphic to V , we follow that the identity map is a trivial representation, often referred to as the defining representation. In this work we do not distinguish or analyze further group representations.

We also introduce the concept of Lie algebra representations. A representation of a Lie algebra \mathfrak{g} is given by a Lie algebra homomorphism

$$\pi : \mathfrak{g} \rightarrow \mathfrak{gl}(V) \quad (\text{A.5})$$

where $\mathfrak{gl}(V)$ is the Lie algebra defined by the linear space of all endomorphisms on the vector space V with the Lie bracket

$$[\rho, \sigma] = \rho \circ \sigma - \sigma \circ \rho \quad (\text{A.6})$$

for all $\rho, \sigma \in \mathfrak{gl}(V)$. For a given representation Π of a Lie group G we can find a representation π defined by

$$\Pi(X) = e^{\pi(X)}, \quad X \in G \quad (\text{A.7})$$

of the corresponding Lie algebra \mathfrak{g} . In particular, we are interested in two representation of Lie algebras, the fundamental representation which is given by the identity map and the adjoint representation

$$\text{ad} : \mathfrak{g} \rightarrow \mathfrak{gl}(\mathfrak{g}), X \mapsto \text{ad}(X) = [X, \cdot]_{\mathfrak{g}}. \quad (\text{A.8})$$

Note that by referring to Lie algebra elements “given in a certain representation” we mean the image of the element under the representation map.

$SU(N_c)$ and $\mathfrak{su}(N_c)$

We now want to introduce the most important properties of the special unitary groups $SU(N_c)$ as a matrix Lie group and its connection to the Lie algebra $\mathfrak{su}(N_c)$. Abstractly this structure forms a $N_c^2 - 1$ dimensional real manifold which forms a topological group. In particle physics a more concrete point of view is taken by using specific representations. The special unitary group in the defining representation can be identified by the group of $N_c \times N_c$ matrices M with

$$\det(M) = 1, \quad M^{-1} = M^\dagger. \quad (\text{A.9})$$

The corresponding Lie algebra $\mathfrak{su}(N_c)$ can be identified with the traceless Hermitian matrices. Furthermore, we can find traceless Hermitian matrices t^a , $a = 1, \dots, N_c^2 - 1$ which generate $SU(N_c)$ and form a basis of $\mathfrak{su}(N_c)$. In the fundamental representation of $\mathfrak{su}(N_c)$ the connection between those structures are given by

$$[t^a, t^b] = if^{abc}t^c, \quad \text{tr}(t^a t^b) = \frac{1}{2}\delta^{ab}, \quad (\text{A.10})$$

where the coefficients f^{abc} can be interpreted as a tensor of type $(3, 0)$. They are known as the totally anti-symmetric structure constants. Those coefficients characterize the Lie algebra uniquely by defining the Lie bracket. We give the generators for the number of colors $N_c = 2, 3$ below.

We can write an algebra elements A, B in terms of generators t^a in the following way

$$A = A^a t^a, \quad B = B^a t^a \quad (\text{A.11})$$

where the some over the color index a is implied. It can be shown that “representing” the Lie algebra elements in this way amounts to the adjoint representation of $\mathfrak{su}(N_c)$. The generators t^a in the adjoint representation can be given in terms of the structure constants

$$(t^a)_{jk} = -if^{ajk}. \quad (\text{A.12})$$

We further can rewrite the trace of the product of two algebra elements using (A.10) and obtain

$$\text{tr}[AB] = \text{tr} \left[\sum_{a=1}^{N_c^2-1} A^a t^a \sum_{b=1}^{N_c^2-1} B^b t^b \right] = \sum_{a=1}^{N_c^2-1} \sum_{b=1}^{N_c^2-1} A^a B^b \text{tr} [t^a t^b] \quad (\text{A.13})$$

$$= \sum_{a=1}^{N_c^2-1} \sum_{b=1}^{N_c^2-1} \frac{1}{2} A^a B^b \delta^{ab} = \frac{1}{2} \sum_{a=1}^{N_c^2-1} A^a B^a = \frac{1}{2} A^a B^a \quad (\text{A.14})$$

In SU(2) the generators are defined in terms of the Pauli matrices

$$\sigma_1 = \begin{pmatrix} 0 & 1 \\ 1 & 0 \end{pmatrix}, \quad \sigma_2 = \begin{pmatrix} 0 & -i \\ i & 0 \end{pmatrix}, \quad \sigma_3 = \begin{pmatrix} 1 & 0 \\ 0 & -1 \end{pmatrix}, \quad (\text{A.15})$$

and are given by $t_k = \frac{1}{2}\sigma_k$. Similarly, for SU(3) the Gellman matrices are used

$$\begin{aligned} \lambda_1 &= \begin{pmatrix} 0 & 1 & 0 \\ 1 & 0 & 0 \\ 0 & 0 & 0 \end{pmatrix}, & \lambda_2 &= \begin{pmatrix} 0 & -i & 0 \\ i & 0 & 0 \\ 0 & 0 & 0 \end{pmatrix}, & \lambda_3 &= \begin{pmatrix} 1 & 0 & 0 \\ 0 & -1 & 0 \\ 0 & 0 & 0 \end{pmatrix}, & \lambda_4 &= \begin{pmatrix} 0 & 0 & 1 \\ 0 & 0 & 0 \\ 1 & 0 & 0 \end{pmatrix}, \\ \lambda_5 &= \begin{pmatrix} 0 & 0 & -i \\ 0 & 0 & 0 \\ i & 0 & 0 \end{pmatrix}, & \lambda_6 &= \begin{pmatrix} 0 & 0 & 0 \\ 0 & 0 & 1 \\ 0 & 1 & 0 \end{pmatrix}, & \lambda_7 &= \begin{pmatrix} 0 & 0 & 0 \\ 0 & 0 & -i \\ 0 & i & 0 \end{pmatrix}, & \lambda_8 &= \frac{1}{\sqrt{3}} \begin{pmatrix} 1 & 0 & 0 \\ 0 & 1 & 0 \\ 0 & 0 & -2 \end{pmatrix}, \end{aligned} \quad (\text{A.16})$$

to define the generators $t_k = \frac{1}{2}\lambda_k$.

B Algorithm for SU(2) theories

In equation (3.1.39) we stated an implicit definition for the transverse link fields. We restate this equation in a more general way for given matrices A, B of the group $SU(N_c)$ which reads

$$\left[(A + B) (\mathbb{1} + U)^\dagger \right]_{ah} = 0. \quad (\text{B.1})$$

In this section we discuss algorithms to find $U \in SU(N_c)$. The subscript “ ah ” in above equation denotes that the anti-hermitian and traceless part of the given matrix. The anti-hermitian and traceless part of a group element M is given by

$$[M]_{ah} = \frac{1}{2i} (M - M^\dagger) - \frac{1}{N_c} \text{tr} \left(\frac{1}{2i} (M - M^\dagger) \right) \mathbb{1}. \quad (\text{B.2})$$

In this work we focus on the case $N_c = 2$. The main difficulty is to find a solution U which is element of the group $SU(2)$. For $N_c > 2$ this equation can only be solved numerically [8].

Algorithm for SU(2)

Assuming $N_c = 2$ we can find a solution for (B.1) explicitly. We start by the more general problem of finding a matrix $U \in SU(2)$ such that

$$\left[(A + B) (\mathbb{1} + U)^\dagger \right] - \left[(A + B) (\mathbb{1} + U)^\dagger \right]^\dagger = 0, \quad (\text{B.3})$$

hence the matrix $(A + B) (\mathbb{1} + U)^\dagger$ has a vanishing anti-hermitian part which is therefore trivially also traceless. Rewriting (B.3) yields

$$\mathbb{1} - (A + B) (A^\dagger + B^\dagger)^{-1} = (A + B) U^\dagger (A^\dagger + B^\dagger) - U. \quad (\text{B.4})$$

Note that in general it holds that

$$(X^\dagger)^{-1} = (X^{-1})^\dagger \quad (\text{B.5})$$

for any non-singular matrix X . Above equation is therefore solved by

$$U = (A + B) (A^\dagger + B^\dagger)^{-1}. \quad (\text{B.6})$$

It remains to show that U is unitary and has satisfies $\det(U) = 1$. Again, using (B.5) and fundamental properties of the determinant we follow

$$\det(U) = \det \left((A + B) (A^\dagger + B^\dagger)^{-1} \right) \quad (\text{B.7})$$

$$= \det(A + B) \det \left((A^\dagger + B^\dagger)^{-1} \right) \quad (\text{B.8})$$

$$= \det(A + B) \det \left((A + B)^{-1} \right) = 1. \quad (\text{B.9})$$

Next, we check if U is a unitary matrix and therefore satisfies

$$UU^\dagger = (A + B) (A^\dagger + B^\dagger)^{-1} (A + B)^{-1} (A + B)^\dagger = \mathbb{1}. \quad (\text{B.10})$$

Using the properties of $SU(2)$ matrices it can be shown that above property is equivalent to

$$B^\dagger A + A^\dagger B = BA^\dagger + AB^\dagger, \quad (\text{B.11})$$

which can be checked explicitly. Hence, we have proven that U is a group element and therefore we have found an explicit expression solving (B.1) for $N_c = 2$.

C Conversion to lattice units

In this section we discuss how to convert dimensional quantities to lattice units such that their relative magnitude remains unchanged. We do this in order to avoid the need of a dimension analysis for the algorithms used during the simulation process. Furthermore, this allows us to overcome certain numerical issues such as rounding error or loss of significance which result from the finite machine accuracy.

Throughout this work we derived all physical quantities in natural units by setting

$$\hbar = 1, \quad c = 1, \quad (\text{C.1})$$

and express all dimensional quantities in units of

$$\begin{aligned} 1 \text{ GeV} &= 10^9 \text{ eV} = 1.602 \times 10^{-10} \text{ J}, \\ 1 \text{ fm} &= 10^{-15} \text{ m}. \end{aligned} \quad (\text{C.2})$$

Using the values for the speed of light and Planck's constant

$$\begin{aligned} \hbar &= 1.0546 \times 10^{-34} \text{ Js}, \\ c &= 299792458 \frac{\text{m}}{\text{s}} \end{aligned} \quad (\text{C.3})$$

we obtain

$$\hbar c = 0.197326 \text{ GeV fm}, \quad (\text{C.4})$$

which is a practical relation for expressing all dimensional quantities in terms of GeV.

We introduce lattice units by defining a scaling constant Q_{latt} with $[Q_{latt}] = \text{GeV}$. We rescale all dimensional quantities such as lattice spacing a , screening mass m or the UV-regulator Λ_{UV} with powers of Q_{latt} such that the resulting quantity is dimensionless. For this conversion assume some quantity X with physical dimensions $[X] = \text{GeV}^a \text{ fm}^b$. We first express X in terms of GeV, which yields

$$X \text{ GeV}^a \text{ fm}^b = (0.197326)^{-b} X \text{ GeV}^{a-b}. \quad (\text{C.5})$$

We now obtain X in lattice units X_{latt} by rescaling with Q_{latt}^{a-b} and obtain

$$X_{latt} = \frac{(0.197326)^{-b} X \text{ GeV}^{a-b}}{Q_{latt}^{a-b} \text{ GeV}^{a-b}} = \left(\frac{Q_{latt}}{0.197326} \right)^b \frac{X}{Q_{latt}^a} \quad (\text{C.6})$$

with $[X_{latt}] = 1$. Note that for all quantities and observables which are calculated during the simulation the reverse conversion has to be applied in order to obtain their magnitudes in physical dimensions.

Bibliography

- [1] Istvan Montvay and Gernot Münster. *Quantum Fields on a Lattice*. Cambridge University Press, Mar. 1997. ISBN: 978-0-521-59917-7.
- [2] Jan Smit. *Introduction to Quantum Fields on a Lattice*. Cambridge University Press, Sept. 2002. ISBN: 978-0-521-89051-9.
- [3] Charles Gale, Sangyong Jeon, and Björn Schenke. “Hydrodynamic Modeling of Heavy-Ion Collisions”. In: *Int. J. Mod. Phys. A* 28 (2013), p. 1340011. DOI: 10.1142/S0217751X13400113.
- [4] Paul Romatschke and Ulrike Romatschke. *Relativistic Fluid Dynamics In and Out of Equilibrium*. Cambridge Monographs on Mathematical Physics. Cambridge University Press, May 2019. ISBN: 978-1-108-48368-1 978-1-108-75002-8. DOI: 10.1017/9781108651998.
- [5] Björn Schenke, Sangyong Jeon, and Charles Gale. “(3+1)D Hydrodynamic Simulation of Relativistic Heavy-Ion Collisions”. In: *Phys. Rev. C* 82 (2010), p. 014903. DOI: 10.1103/PhysRevC.82.014903.
- [6] T. Lappi and L. McLerran. “Some Features of the Glasma”. In: *Nucl. Phys. A* 772 (2006), pp. 200–212. DOI: 10.1016/j.nuclphysa.2006.04.001.
- [7] T. Lappi. “The Glasma Initial State at the LHC”. In: *J. Phys. G* 35 (2008). Ed. by Jan-e Alam et al., p. 104052. DOI: 10.1088/0954-3899/35/10/104052.
- [8] David Müller. “Simulations of the Glasma in 3+1D”. PhD thesis. Vienna, Tech. U., 2019.
- [9] Peter Brockway Arnold, Guy D. Moore, and Laurence G. Yaffe. “Effective Kinetic Theory for High Temperature Gauge Theories”. In: *JHEP* 01 (2003), p. 030. DOI: 10.1088/1126-6708/2003/01/030.
- [10] Aleksi Kurkela et al. “Matching the Nonequilibrium Initial Stage of Heavy Ion Collisions to Hydrodynamics with QCD Kinetic Theory”. In: *Phys. Rev. Lett.* 122.12 (2019), p. 122302. DOI: 10.1103/PhysRevLett.122.122302.
- [11] Aleksi Kurkela and Yan Zhu. “Isotropization and Hydrodynamization in Weakly Coupled Heavy-Ion Collisions”. In: *Phys. Rev. Lett.* 115.18 (2015), p. 182301. DOI: 10.1103/PhysRevLett.115.182301.
- [12] Edmond Iancu and Raju Venugopalan. “The Color Glass Condensate and High-Energy Scattering in QCD”. In: *Quark-Gluon Plasma 4*. Ed. by Rudolph C. Hwa and Xin-Nian Wang. Mar. 2003, pp. 249–3363. DOI: 10.1142/9789812795533_0005.
- [13] Francois Gelis et al. “The Color Glass Condensate”. In: *Ann. Rev. Nucl. Part. Sci.* 60 (2010), pp. 463–489. DOI: 10.1146/annurev.nucl.010909.083629.
- [14] F. Gelis. “Color Glass Condensate and Glasma”. In: *Int. J. Mod. Phys. A* 28 (2013), p. 1330001. DOI: 10.1142/S0217751X13300019.
- [15] Charles Gale et al. “Multi-Messenger Heavy-Ion Physics”. In: (June 2021).
- [16] Adam Bzdak et al. “Initial-State Geometry and the Role of Hydrodynamics in Proton-Proton, Proton-Nucleus, and Deuteron-Nucleus Collisions”. In: *Physical Review C* 87.6 (June 2013), p. 064906. DOI: 10.1103/PhysRevC.87.064906.

- [17] Scott McDonald, Sangyong Jeon, and Charles Gale. “IP-Glasma Phenomenology Beyond 2D”. In: *Nucl. Phys. A* 982 (2019). Ed. by Federico Antinori et al., pp. 239–242. DOI: 10.1016/j.nuclphysa.2018.08.014.
- [18] Scott McDonald, Sangyong Jeon, and Charles Gale. “Exploring Longitudinal Observables with 3+1D IP-Glasma”. In: *Nucl. Phys. A* 1005 (2021). Ed. by Feng Liu et al., p. 121771. DOI: 10.1016/j.nuclphysa.2020.121771.
- [19] Björn Schenke, Chun Shen, and Prithwish Tribedy. “Features of the IP-Glasma”. In: *Nucl. Phys. A* 982 (2019). Ed. by Federico Antinori et al., pp. 435–438. DOI: 10.1016/j.nuclphysa.2018.08.015.
- [20] Björn Schenke, Prithwish Tribedy, and Raju Venugopalan. “Event-by-Event Gluon Multiplicity, Energy Density, and Eccentricities in Ultrarelativistic Heavy-Ion Collisions”. In: *Phys. Rev. C* 86 (2012), p. 034908. DOI: 10.1103/PhysRevC.86.034908.
- [21] Aleksi Kurkela et al. “Effective Kinetic Description of Event-by-Event Pre-Equilibrium Dynamics in High-Energy Heavy-Ion Collisions”. In: *Phys. Rev. C* 99.3 (2019), p. 034910. DOI: 10.1103/PhysRevC.99.034910.
- [22] Andreas Ipp and David I. Müller. “Progress on 3+1D Glasma Simulations”. In: *Eur. Phys. J. A* 56.9 (2020), p. 243. DOI: 10.1140/epja/s10050-020-00241-6.
- [23] Andreas Ipp and David Müller. “Rapidity Profiles from 3+1D Glasma Simulations with Finite Longitudinal Thickness”. In: *PoS EPS-HEP2017* (2017). Ed. by Paolo Checchia et al., p. 176. DOI: 10.22323/1.314.0176.
- [24] Andreas Ipp and David Müller. “Broken Boost Invariance in the Glasma via Finite Nuclei Thickness”. In: *Phys. Lett. B* 771 (2017), pp. 74–79. DOI: 10.1016/j.physletb.2017.05.032.
- [25] Daniil Gelfand, Andreas Ipp, and David Müller. “Simulating Collisions of Thick Nuclei in the Color Glass Condensate Framework”. In: *Phys. Rev. D* 94.1 (2016), p. 014020. DOI: 10.1103/PhysRevD.94.014020.
- [26] T. Lappi. “Rapidity Distribution of Gluons in the Classical Field Model for Heavy Ion Collisions”. In: *Phys. Rev. C* 70 (2004), p. 054905. DOI: 10.1103/PhysRevC.70.054905.
- [27] Björn Schenke and Sören Schlichting. “3D Glasma Initial State for Relativistic Heavy Ion Collisions”. In: *Phys. Rev. C* 94.4 (2016), p. 044907. DOI: 10.1103/PhysRevC.94.044907.
- [28] Larry D. McLerran and Raju Venugopalan. “Gluon Distribution Functions for Very Large Nuclei at Small Transverse Momentum”. In: *Phys. Rev. D* 49 (1994), pp. 3352–3355. DOI: 10.1103/PhysRevD.49.3352.
- [29] Larry D. McLerran and Raju Venugopalan. “Computing Quark and Gluon Distribution Functions for Very Large Nuclei”. In: *Phys. Rev. D* 49 (1994), pp. 2233–2241. DOI: 10.1103/PhysRevD.49.2233.
- [30] K. Boguslavski et al. “Broad Excitations in a 2+1D Overoccupied Gluon Plasma”. In: *JHEP* 05 (2021), p. 225. DOI: 10.1007/JHEP05(2021)225.
- [31] K. Boguslavski et al. “Highly Occupied Gauge Theories in 2+1 Dimensions: A Self-Similar Attractor”. In: *Phys. Rev. D* 100.9 (2019), p. 094022. DOI: 10.1103/PhysRevD.100.094022.
- [32] Jürgen Berges et al. “Universal Attractor in a Highly Occupied Non-Abelian Plasma”. In: *Phys. Rev. D* 89.11 (2014), p. 114007. DOI: 10.1103/PhysRevD.89.114007.
- [33] Kirill Boguslavski. “Universality Classes Far from Equilibrium: From Heavy-Ion Collisions to Superfluid Bose Systems”. PhD thesis. Jan. 2016.

- [34] Sören Schlichting. “Non-Equilibrium Dynamics and Thermalization of Weakly Coupled Non-Abelian Plasmas”. PhD thesis. U. Heidelberg (main), Aug. 2013. DOI: 10.11588/heidok.00015314.
- [35] Jürgen Berges. “Introduction to Nonequilibrium Quantum Field Theory”. In: *AIP Conference Proceedings*. Vol. 739. Rio de Janeiro (Brazil): AIP, 2004, pp. 3–62. DOI: 10.1063/1.1843591.
- [36] Christof Gattringer and Christian B. Lang. *Quantum Chromodynamics on the Lattice: An Introductory Presentation*. Lecture Notes in Physics. Berlin Heidelberg: Springer-Verlag, 2010. ISBN: 978-3-642-01849-7. DOI: 10.1007/978-3-642-01850-3.
- [37] E. Follana et al. “Highly Improved Staggered Quarks on the Lattice, with Applications to Charm Physics”. In: *Phys. Rev. D* 75 (2007), p. 054502. DOI: 10.1103/PhysRevD.75.054502.
- [38] Kenneth G. Wilson. “Confinement of Quarks”. In: *Phys. Rev. D* 10 (1974). Ed. by J. C. Taylor, pp. 2445–2459. DOI: 10.1103/PhysRevD.10.2445.
- [39] Kevin Dusling, Francois Gelis, and Raju Venugopalan. “The Initial Spectrum of Fluctuations in the Little Bang”. In: *Nucl. Phys. A* 872 (2011), pp. 161–195. DOI: 10.1016/j.nuclphysa.2011.09.012.
- [40] A. Makhlin. “The Wedge Form of Relativistic Dynamics. 2. The Gluons”. In: (Aug. 1996).
- [41] T. Lappi. “Production of Gluons in the Classical Field Model for Heavy Ion Collisions”. In: *Phys. Rev. C* 67 (2003), p. 054903. DOI: 10.1103/PhysRevC.67.054903.
- [42] Jamal Jalilian-Marian et al. “The Intrinsic Glue Distribution at Very Small x ”. In: *Phys. Rev. D* 55 (1997), pp. 5414–5428. DOI: 10.1103/PhysRevD.55.5414.
- [43] T. Lappi. “Energy Density of the Glasma”. In: *Phys. Lett. B* 643 (2006), pp. 11–16. DOI: 10.1016/j.physletb.2006.10.017.
- [44] Owe Philipsen, Björn Wagenbach, and Savvas Zafeiropoulos. “From the Colour Glass Condensate to Filamentation: Systematics of Classical Yang–Mills Theory”. In: *Eur. Phys. J. C* 79.4 (2019), p. 286. DOI: 10.1140/epjc/s10052-019-6790-8.
- [45] Alex Krasnitz and Raju Venugopalan. “Nonperturbative Computation of Gluon Minijet Production in Nuclear Collisions at Very High-Energies”. In: *Nucl. Phys. B* 557 (1999), p. 237. DOI: 10.1016/S0550-3213(99)00366-1.
- [46] C. T. H. Davies et al. “Fourier Acceleration in Lattice Gauge Theories. 1. Landau Gauge Fixing”. In: *Phys. Rev. D* 37 (1988), p. 1581. DOI: 10.1103/PhysRevD.37.1581.
- [47] Guy D. Moore. “Motion of Chern-Simons Number at High Temperatures under a Chemical Potential”. In: *Nucl. Phys. B* 480 (1996), pp. 657–688. DOI: 10.1016/S0550-3213(96)00445-2.
- [48] Kenji Fukushima. “Initial Fields and Instability in the Classical Model of the Heavy-Ion Collision”. In: *Phys. Rev. C* 76 (2007), p. 021902. DOI: 10.1103/PhysRevC.76.021902.
- [49] Hirotugu Fujii, Kenji Fukushima, and Yoshimasa Hidaka. “Initial Energy Density and Gluon Distribution from the Glasma in Heavy-Ion Collisions”. In: *Phys. Rev. C* 79 (2009), p. 024909. DOI: 10.1103/PhysRevC.79.024909.
- [50] T. Lappi. “Wilson Line Correlator in the MV Model: Relating the Glasma to Deep Inelastic Scattering”. In: *Eur. Phys. J. C* 55 (2008), pp. 285–292. DOI: 10.1140/epjc/s10052-008-0588-4.
- [51] Kenji Fukushima and Francois Gelis. “The Evolving Glasma”. In: *Nucl. Phys. A* 874 (2012), pp. 108–129. DOI: 10.1016/j.nuclphysa.2011.11.003.
- [52] Kirill Boguslavski et al. “Spectral Function of Fermions in a Highly Occupied Non-Abelian Plasma”. In: (June 2021).

-
- [53] K. Boguslavski et al. “Spectral Function for Overoccupied Gluodynamics from Real-Time Lattice Simulations”. In: *Phys. Rev. D* 98.1 (2018), p. 014006. DOI: 10.1103/PhysRevD.98.014006.
- [54] J. P. Blaizot, T. Lappi, and Y. Mehtar-Tani. “On the Gluon Spectrum in the Glasma”. In: *Nucl. Phys. A* 846 (2010), pp. 63–82. DOI: 10.1016/j.nuclphysa.2010.06.009.
- [55] Naoto Tanji and Raju Venugopalan. “Effective Kinetic Description of the Expanding Overoccupied Glasma”. In: *Phys. Rev. D* 95.9 (2017), p. 094009. DOI: 10.1103/PhysRevD.95.094009.
- [56] Aleksi Kurkela et al. “Initial Conditions for Heavy Ion Collisions with QCD Kinetic Theory”. In: *PoS High-pT2017* (2019), p. 001. DOI: 10.22323/1.320.0001.
- [57] Aleksi Kurkela et al. “Initial Conditions for Hydrodynamics from Kinetic Theory Equilibration”. In: *Nucl. Phys. A* 967 (2017). Ed. by Ulrich Heinz, Olga Evdokimov, and Peter Jacobs, pp. 289–292. DOI: 10.1016/j.nuclphysa.2017.04.009.
- [58] Jürgen Berges and Sören Schlichting. “The Nonlinear Glasma”. In: *Phys. Rev. D* 87.1 (2013), p. 014026. DOI: 10.1103/PhysRevD.87.014026.
- [59] Aleksi Kurkela and Guy D. Moore. “Bjorken Flow, Plasma Instabilities, and Thermalization”. In: *JHEP* 11 (2011), p. 120. DOI: 10.1007/JHEP11(2011)120.
- [60] Raju Venugopalan. “From Glasma to Quark Gluon Plasma in Heavy Ion Collisions”. In: *J. Phys. G* 35 (2008). Ed. by Jan-e Alam et al., p. 104003. DOI: 10.1088/0954-3899/35/10/104003.
- [61] Brian Hall. *Lie Groups, Lie Algebras, and Representations: An Elementary Introduction*. Springer, May 2015. ISBN: 978-3-319-13467-3.